



2017

DECONVOLVING THE STEPS TO CONTROL MORPHOLOGY, COMPOSITION, AND STRUCTURE, IN THE SYNTHESIS OF HIGH- ASPECT-RATIO METAL OXIDE NANOMATERIALS

Lei Yu

University of Kentucky, lei.yu@uky.edu

Author ORCID Identifier:

 <https://orcid.org/0000-0002-3975-8930>

Digital Object Identifier: <https://doi.org/10.13023/ETD.2017.306>

[Right click to open a feedback form in a new tab to let us know how this document benefits you.](#)

Recommended Citation

Yu, Lei, "DECONVOLVING THE STEPS TO CONTROL MORPHOLOGY, COMPOSITION, AND STRUCTURE, IN THE SYNTHESIS OF HIGH-ASPECT-RATIO METAL OXIDE NANOMATERIALS" (2017). *Theses and Dissertations--Chemistry*. 82.

https://uknowledge.uky.edu/chemistry_etds/82

This Doctoral Dissertation is brought to you for free and open access by the Chemistry at UKnowledge. It has been accepted for inclusion in Theses and Dissertations--Chemistry by an authorized administrator of UKnowledge. For more information, please contact UKnowledge@lsv.uky.edu.

STUDENT AGREEMENT:

I represent that my thesis or dissertation and abstract are my original work. Proper attribution has been given to all outside sources. I understand that I am solely responsible for obtaining any needed copyright permissions. I have obtained needed written permission statement(s) from the owner(s) of each third-party copyrighted matter to be included in my work, allowing electronic distribution (if such use is not permitted by the fair use doctrine) which will be submitted to UKnowledge as Additional File.

I hereby grant to The University of Kentucky and its agents the irrevocable, non-exclusive, and royalty-free license to archive and make accessible my work in whole or in part in all forms of media, now or hereafter known. I agree that the document mentioned above may be made available immediately for worldwide access unless an embargo applies.

I retain all other ownership rights to the copyright of my work. I also retain the right to use in future works (such as articles or books) all or part of my work. I understand that I am free to register the copyright to my work.

REVIEW, APPROVAL AND ACCEPTANCE

The document mentioned above has been reviewed and accepted by the student's advisor, on behalf of the advisory committee, and by the Director of Graduate Studies (DGS), on behalf of the program; we verify that this is the final, approved version of the student's thesis including all changes required by the advisory committee. The undersigned agree to abide by the statements above.

Lei Yu, Student

Dr. Beth S. Guiton, Major Professor

Dr. Mark A. Lovell, Director of Graduate Studies

DECONVOLVING THE STEPS TO CONTROL MORPHOLOGY, COMPOSITION,
AND STRUCTURE, IN THE SYNTHESIS OF HIGH-ASPECT-RATIO METAL
OXIDE NANOMATERIALS

Dissertation

A dissertation submitted in partial fulfillment of the
requirements for the degree of Doctor of Philosophy in the
College of Arts and Sciences
at the University of Kentucky

By
Lei Yu
Lexington, Kentucky

Director: Dr. Beth S. Guiton, Associate Professor of Chemistry
Lexington, Kentucky 2017

Copyright © Lei Yu 2017

ABSTRACT OF DISSERTATION

DECONVOLVING THE STEPS TO CONTROL MORPHOLOGY, COMPOSITION, AND STRUCTURE, IN THE SYNTHESIS OF HIGH-ASPECT-RATIO METAL OXIDE NANOMATERIALS

Metal oxides are of interest not only because of their huge abundance but also for their many applications such as for electrocatalysts, gas sensors, diodes, solar cells and lithium ion batteries (LIBs). Nano-sized metal oxides are especially desirable since they have larger surface-to-volume ratios advantageous for catalytic properties, and can display size and shape confinement properties such as magnetism. Thus, it is very important to explore the synthetic methods for these materials. It is essential, therefore, to understand the reaction mechanisms to create these materials, both on the nanoscale, and in real-time, to have design control of materials with desired morphologies and functions.

This dissertation covers both the design of new syntheses for nanomaterials, as well as real-time methods to understand their synthetic reaction mechanisms. It will focus on two parts: first, the synthesis of 1-dimension (1-D) featured nanomaterials, including manganese-containing spinel nanowires, and tin dioxide and zinc oxide-based negative nanowire arrays; and second, a mechanistic study of the synthetic reactions of nanomaterials using *in situ* transmission electron microscopy (TEM). The work presented here demonstrates unique synthetic routes to single crystalline “positive” and “negative” metal oxide nanowires, and introduces a new mechanism for the formation of single-crystalline hollow nanorods.

KEYWORDS: metal oxides, nanowires, *in situ*, TEM

Student's signature: Lei Yu

Date: July 18, 2017

DECONVOLVING THE STEPS TO CONTROL MORPHOLOGY, COMPOSITION,
AND STRUCTURE, IN THE SYNTHESIS OF HIGH-ASPECT-RATIO METAL
OXIDE NANOMATERIALS

By
Lei Yu

Dr. Beth S. Guiton
Director of Dissertation

Dr. Mark A. Lovell
Director of Graduate Studies

July 18, 2017

ACKNOWLEDGMENTS

Dr. Beth Guiton has not only been an extraordinary advisor and mentor; she has been a friend and guide during my Ph.D. research. I thank her for letting me join the group and introducing me to electron microscopy, a completely new and exciting world to me. She granted me the freedom to approach the topics that interest me, encouraged me to try my own ideas, and gave me the opportunity to work in Oak Ridge National Laboratory for the last year to meet with top scientists and use the most advanced microscopes. Moreover, I want to thank her for sharing her love and passion for life and science, and how to find a balance between work and family. All of those experiences are constructive and beneficial to my career and life thereafter.

I also want to express my gratitude to my dissertation committee: Dr. John Selegue, Dr. Doo Young Kim, Dr. Dibakar Bhattacharyya for taking time from their busy schedule to attend committee meetings, giving me advice and keeping me on track to obtain my Ph.D.

I could not have come this far without the help of people I met at both UK and ORNL. I appreciate the timely response and assistance from department staff. I thank Dr. Jason Backus for his training and years of help on XRD, and Dr. Dali Qian and Dr. Nicolas Briot from the Electron Microscopy Center for their keen assistance on using SEM, TEM and FIB. I also want to express great gratitude to Dr. David Cullen, Dr. Juan-Carlos Idrobo, and Dr. Andrew Lupini from ORNL, for not only training and helping me on the electron microscopes, but also their precious words of advice on my career path. And special thanks to Dr. Karren More for being as my mentor at ORNL.

I am so grateful to have such awesome lab mates and friends, who are ready to help and support each other. In particular, I want to thank Bethany Hudak for training me on the microscopes I have been using both at UK and ORNL, and her company especially after I moved to Oak Ridge. I will miss those days we hung out together. Xiaojia Ren, thank you for all the girls' talks and the good care you've taken of me when I felt lost and uncertain. You made me feel like I was at home with family while so far away from my hometown. I cannot wait to see the birth of your baby girl, and I know you'll make a great mom! I also want to thank Xiahan Sang and Wei Guo at Oak Ridge, not only for sharing their thoughts on research and careers with me, but also for treating me like their family.

Finally, I want to thank my parents back in China. Mum, thank you for sculpting me into a happy and optimistic person, and my chill Dad, for teaching me to be a hard worker and thinker. I could never finish my Ph.D. without your love and support. I feel proud to be the first Ph.D. in our family, and even more proud to be your daughter. Love you.

TABLE OF CONTENTS

ACKNOWLEDGMENTS	iii
LIST OF FIGURES	vi
CHAPTER 1 Introduction.....	1
1.1 Motivation.....	1
1.2 1-D nano structure synthetic approaches	3
1.2.1 Introduction.....	3
1.2.2 Hydrothermal syntheses.....	4
1.2.3 Metal-catalyzed syntheses	7
1.2.4 Solid to solid transformations	10
1.3 <i>In situ</i> transmission electron microscopy.....	13
1.3.1 Introduction.....	14
1.3.2 Studies on 1-D nanostructure synthesis using <i>in situ</i> TEM.....	15
CHAPTER 2 Experimental methods	18
2.1 Sample preparation	18
2.1.1 Hydrothermal syntheses of metal oxide nanowires	18
2.1.2 Pulsed laser deposition for thin film growth.....	19
2.2 Characterization	19
2.2.1 Powder X-ray diffraction	19
2.2.2 Scanning electron microscopy	19
2.2.3 X-ray photoelectron spectroscopy	20
2.2.4 Linear sweep voltammetry.....	21
2.3 Transmission electron microscopy	23
2.3.1 Principles of transmission electron microscopy	23
2.3.2 Scanning transmission electron microscopy.....	25
2.3.3 Energy dispersive X-ray spectroscopy.....	27
2.3.4 Electron energy loss spectroscopy	29
2.3.5 <i>In situ</i> heating within TEM.....	31
CHAPTER 3 Manganese-containing nanowires with the spinel crystal structure	33
3.1 Introduction.....	33
3.2 Methods.....	37
3.3 CuMn ₂ O ₄ , MgMn ₂ O ₄ and Mg ₂ MnO ₄ nanowires	38
3.4 <i>In situ</i> TEM study of the reaction mechanism for spinel nanowires	46
3.5 Catalytic properties towards oxygen evolution reactions	47
3.6 Conclusion	51
CHAPTER 4 Solid-liquid-vapor synthesis of negative metal oxide nanowire arrays.....	52
4.1 Introduction.....	52
4.2 Methods.....	56
4.3 Temperature and time effect on SLV etching for SnO ₂ thin films	57
4.4 Effect of catalyst particle size and crystal orientation on SLV etching for ZnO.....	60
4.5 SLV etching on silicon substrate	64
4.6 Conclusion	67

CHAPTER 5 Understanding hollow metal oxide nanomaterial formation with <i>in situ</i>	
TEM	68
5.1 Introduction.....	68
5.2 Syntheses of β -FeOOH nanorods and nanowires	71
5.3 Formation of hollow iron oxide nanorod in <i>in situ</i> TEM.....	71
5.4 Conclusion	83
REFERENCES	85
VITA.....	105

LIST OF FIGURES

Figure 1.1 SEM images of MnO ₂ NWs fabricated through hydrothermal method.	7
Figure 1.2 Cartoon showing VLS growth mechanism.....	8
Figure 1.3 SEM images of ZnO NWs growth on (a) Si substrate and (b) sapphire substrate	9
Figure 1.4 Cartoon showing (a) SLV dissolution of a single NW and (b) SLV formation of negative NWs.	10
Figure 1.5 Cartoon showing three types of solid-to-solid transformation of NWs	11
Figure 1.6 Schematic graph showing an experimental setup for solid nanobattery cell in TEM	16
Figure 2.1 Schematic picture of hydrothermal reactor.	18
Figure 2.2 Diagram illustrating the interactions of the incident electron-beam with the sample in the SEM	20
Figure 2.3 Linear sweep voltammetry set-up	22
Figure 2.4 Cartoon depicting the interactions of incident electrons with the specimen in a TEM	25
Figure 2.5 Schematic diagram depicting HAADF, ADF and BF detectors in the STEM	27
Figure 2.6 Schematic figure showing the emission of characteristic X-rays as a result of interactions of the incident electron-beam and atom	28
Figure 2.7 EELS spectrum of a 20 nm thin titanium carbide specimen	30
Figure 2.8 Details of Protochips Aduro E-chip.	31
Figure 3.1 Structure of cubic spinel AB ₂ O ₄	35
Figure 3.2 Structural characterization of MnO ₂ to CuMn ₂ O ₄ conversion.	39
Figure 3.3 Crystallinity and compositional analysis of a CuMn ₂ O ₄ NW	40
Figure 3.4 (a) Calculated XRD patterns of CuMn ₂ O ₄ with varied inversion degree, (b) Comparison of experimental data to calculated one	41
Figure 3.5 Structural characterization of Mg-containing NW syntheses.....	42
Figure 3.6 Crystallinity and compositional analysis of a Mg ₂ MnO ₄ NW	44
Figure 3.7 EDS spectra and TEM images (inset) from NP impurities present in the ternary oxides synthesized from γ -MnOOH starting material.....	44
Figure 3.8 Structural characterization and compositional analysis CuMn ₂ O ₄ synthesized from γ -MnOOH starting material.	45
Figure 3.9 Frames from an <i>in situ</i> TEM heating video from a γ -MnOOH NW in contact with Mg(OH) ₂ crystal	46
Figure 3.10 EDS spectra taken from the MnOOH NW before and after <i>in situ</i> TEM heating.....	47
Figure 3.11 XPS spectra for CuMn ₂ O ₄ , MgMn ₂ O ₄ and Mg ₂ MnO.	48
Figure 3.12 Linear sweep voltammetry curves of CuMn ₂ O ₄ , Mg ₂ MnO ₄ , and MgMn ₂ O ₄	49
Figure 4.1 Cartoon depicting (a) VLS growth of NWs, (b) SLV dissolution of NWs, and (c) SLV creation of negative NWs.....	53
Figure 4.2 Characterization of SnO ₂ on Al ₂ O ₃ thin film	57
Figure 4.3 SEM images of the SLV process.....	58

Figure 4.4 Cross-section SEM image and EDS spectrum of SnO ₂ thin film etched with 8 nm thickness of Au	59
Figure 4.6 SEM images of (1000) ZnO substrate deposited with 50 nm gold NPs. (a) Before and (b) after etching	61
Figure 4.7 SEM images of gold NP etched ZnO substrates with different orientations upon annealing at 1000°C for 30 min	62
Figure 4.7 SEM images of gold NP etched (0001) ZnO substrates in high vacuum	63
Figure 4.8 SEM images of gold NP etched Si substrate	64
Figure 5.1 Structural characterization for β -FeOOH NRs	71
Figure 5.2 Structural characterization of hollow α -Fe ₂ O ₃ NRs	72
Figure 5.3 Thermal gravimetric analysis of β -FeOOH NRs	73
Figure 5.4 <i>In situ</i> XRD of β -FeOOH NRs in low vacuum	74
Figure 5.5 TEM images of an FeOOH NR as it is heated <i>in situ</i>	75
Figure 5.6 TEM images and corresponding selected area diffraction patterns of a NR during <i>in situ</i> heating	76
Figure 5.7 Iron edge of the electron energy loss spectrum of a NR.	77
Figure 5.8 Oxygen edge of the electron energy loss spectrum of a NR	78
Figure 5.9. Graphical representations of crystal structures of β -FeOOH, β -Fe ₂ O ₃ , γ -Fe ₂ O ₃ /Fe ₃ O ₄ , FeO, α -Fe ₂ O ₃	80
Figure 5.10 Cartoon showing the structure decomposition of a NR for density calculations	81
Figure 5.11 TEM images of an FeOOH NW before (a) and after (b) heating in TEM	82
Figure 5.12 Surface confined Ostwald ripening	83

Chapter 1 Introduction

1.1 Motivation

Metal oxides are of interest for their applications as electrocatalysts¹, gas sensors², diodes³, solar cells⁴ and LIBs⁵. Nano-sized metal oxides are desirable since they have large surface-to-volume ratios advantageous for catalytic properties, and can display size- and shape-dependent properties such as magnetism. Researchers have been investigating the synthesis of metal oxides with different nanostructured morphologies, such as nanoparticles (NPs), nanowires (NWs), nanotubes (NTs) and core-shell structures, for use as functional materials. Among those various morphologies, 1-D nanostructures such as NWs and NTs are especially interesting due to their structural one-dimensionality, leading to a wide range of potential nanoscale device applications.⁶

Fabrication routes of 1-D nanostructures can be generally categorized into two types: top-down and bottom-up. Top-down synthetic routes are standard techniques for semiconductor manufacturing, and are subtractive approaches in which smaller features are created from a larger piece of material.⁷⁻⁹ The mask and the technologies used for etching (e.g. electron-beam or ion-beam induced etching) have, however, largely limited the spatial resolution of the nanoscale features. The bottom-up method, which builds up from atoms or small molecules and generally includes growth from vapor phase and solution phase, owns atomic precision in comparison.⁷

In a typical vapor phase synthesis, the vapor produced at a high temperature is transported onto a substrate in a lower temperature region, where the material condenses and grows into NWs. More often, a liquid droplet phase catalyzes the growth of the nanostructures and this is referred to as the vapor-liquid-solid (VLS) process. Syntheses

based on this mechanism have been widely used for a large number of oxide NWs, including ZnO¹⁰, SnO₂¹¹, Ga₂O₃¹², and TiO₂.¹³

The growth of NWs can also be carried out in solution such as under hydrothermal conditions, which can be utilized to produce NWs in large scale with relatively low cost. This method has been used successfully for the synthesis of NWs of ZnO¹⁴, MnO₂¹⁵ and Fe₂O₃¹⁶ among other methods.

One intriguing method for the synthesis of materials whose crystal structures are not naturally inclined to form one-dimensional morphologies is by utilizing a solid-to-solid phase transformation from existing precursor NWs. In this approach a naturally one-dimensional material is grown in NW form, and then converted in a second, often topotactic, step, to the desired structure and composition, while maintaining the original NW morphology. For example, the decomposition of metal hydroxide NWs might lead to metal oxide NWs for combinations like MnOOH/Mn₂O₃,¹⁷ FeOOH/ Fe₂O₃¹⁸ etc.

To refine the synthesis of 1-D metal oxide nanostructures, a wide variety of characterization techniques have been employed to determine structure, morphology, and composition. X-ray diffraction (XRD) and neutron diffraction spectroscopy are commonly used to determine the crystal and/or magnetic structures of solid-state materials.¹⁹⁻²² X-ray photoelectron spectroscopy (XPS) has been very powerful in identifying the elemental species and determining their oxidation states, of particular importance for transition metal oxides, which often display multiple oxidation states.

To further examine the structure and properties of nanomaterial samples, direct nano/atomic scale analyses are needed. Electron microscopies provide very powerful tools for microanalysis when combined with appropriate detectors, not only allowing

direct imaging of a sample down to the atomic scale, but also helping to identify impurities, dislocations, and grain boundaries. Transmission electron microscopy (TEM), in particular, provides atomic-resolution imaging, along with Z-contrast imaging, selected area electron diffraction (SAED), electron dispersive X-ray spectroscopy (EDS) and electron energy loss spectroscopy (EELS), which enables a full range of characterization approaches for nanomaterials.

In the past, information on the structure and properties of materials was typically acquired from *ex situ* characterization techniques, both to design the nanomaterials and to understand their formation mechanisms. Nanoscale reaction mechanisms were commonly explored by time-dependent studies complemented with TEM characterization.^{4,23–25} However, information obtainable from *ex situ* experiments is limited and these “time-dependent” characterizations are very limited, and leads to the necessity of deducing mechanistic steps from “before” and “after” data points. To this end, *in situ* experiments especially *in situ* TEM-based experiments have been exploited and found to be more reliable to study the reaction mechanisms for certain nanostructures.

Temperature control has been a main feature for modern *in situ* TEM technology. *In situ* TEM heating can be used to study the material behavior up to about 1200 °C, within which reactions of nanomaterials can be observed in real time, along with both qualitative and quantitative analyses.

1.2 1-D nano structure synthetic approaches

1.2.1 Introduction

As mentioned above, 1-D nanostructures may be fabricated either via bottom-up or by top-down methods. From the perspective of a chemist, bottom-up methods are highly

desirable since they enable interactions between the smallest building blocks of matter to dictate the eventual structure and function of the nanomaterial. The purpose of this chapter is to describe the advantages and disadvantages of the approaches used for my dissertation work.

1.2.2 Hydrothermal syntheses

Hydrothermal synthesis refers to reactions in aqueous solutions at high temperature and pressure. As far back as the eighteenth century, geologists and mineralogists have known that numerous minerals were formed under such conditions in nature. Gradually, hydrothermal methods were introduced into the laboratory, to synthesize mineral crystals. The French scientist, De Sénarmont, was instrumental in the foundation of this field; he utilized sealed glass ampoules to contain the reactants and placed the ampoules in autoclaves (welded gun barrels) to avoid explosion. He successfully synthesized large numbers of oxides, carbonates, fluorides, sulfates and sulfides. In recent years this approach has been widely used by chemists and engineers to grow nanosized single crystals.^{15,26–29}

It is known that the properties of solvents under hydrothermal conditions are very different from those in standard conditions. In the hydrothermal condition, the lowered dielectric constant of water provides an environment for the electrolyte to form ion pairs or complexes, and precedes the formation of a nucleus for crystal growth. The decreased viscosity allows for improved mobility to maintain a supply of raw material for crystallization, and an increased ionic product indicates an increase in the concentration of dissociated water species, necessary for reaction.³⁰

In a typical hydrothermal synthesis, tiny crystalline nuclei form in the supersaturated medium, followed by crystal growth; large particles then grow at expense of smaller ones through an Ostwald ripening process. The formation and aspect ratios of 1-D nanostructures can be affected by factors such as the pH of solution,^{31–33} reactant concentrations,^{27,33–35} reaction temperature^{33,36,37} and growth time^{36,38} during a hydrothermal synthesis. Some crystal structures tend to exhibit anisotropic growth, for example, hexagonal crystal structures such as ZnO,³⁹ Ln(OH)₃,⁴⁰ and LnPO₄ (Ln = La-> Dy)²⁸. For materials with isotropic structures, however, growing anisotropic structures under the same conditions is a challenge. In this case the use of a template, or stabilizing/capping reagents such as polymers⁴¹, surfactants,²⁶ or strong chelating ligands,⁴² are used to break the isotropy through the interaction of the capping molecule on selective facets of the NP nuclei.^{42–44}

There are several proposed mechanisms for the 1D nanostructure growth within the confinement of capping reagents, which control kinetically the growth rate of the different faces of particles by interacting with those faces through adsorption and desorption. In the case of 1-D structure, the lateral faces are passivated with respect to the axial growth plane, resulting in slower growth rate of the passivated planes.^{42,45–47} Similarly, Joo et al.⁴⁸ were able to manipulate the aspect ratio of ZnO NWs pronouncedly, but instead of using capping reagents, through a face-selective crystal growth inhibition mechanism in an alkaline environment, by adding charged non-zinc complex ions. Since ZnO is charged negatively on the (0002) top surface and positively on the (1010) sidewalls respectively, the added charged metal complexes are selectively

electrostatically attracted to either the top face or the side wall, and hinder the growth of that face.

The hydrothermal reactor includes an autoclave usually made of steel, with or without an inner reaction vessel which lines the interior wall of the autoclave, or acts as a separate “floating insert”. The materials of the hydrothermal reactor are chosen depending on their compatibility with the reaction system in question. For example, borosilicate and quartz glasses are stable towards neutral and acidic solutions, usable up to 300-500 °C, and in both cases transparent, allowing the experiment to be observed directly. In contrast with quartz glass, Teflon handles better with corrosives such as alkaline media and hydrofluoric acid, and can be used below 300 °C and 250 bars with autoclaves; such a combination is commercially available and most commonly chosen.

Hydrothermal syntheses have many advantages over ceramic synthetic methods. Firstly, they are readily able to be scaled-up and cost effective. Secondly, hydrothermal syntheses allow for good control over size and morphology due to the uniformity of nucleation. They also have regulated growth rate, and low agglomeration of the precipitated crystals from solution.⁴⁹ Figure 1.1 shows the SEM image of MnO₂ NWs exhibiting homogeneous morphology, synthesized in our lab using a hydrothermal method.

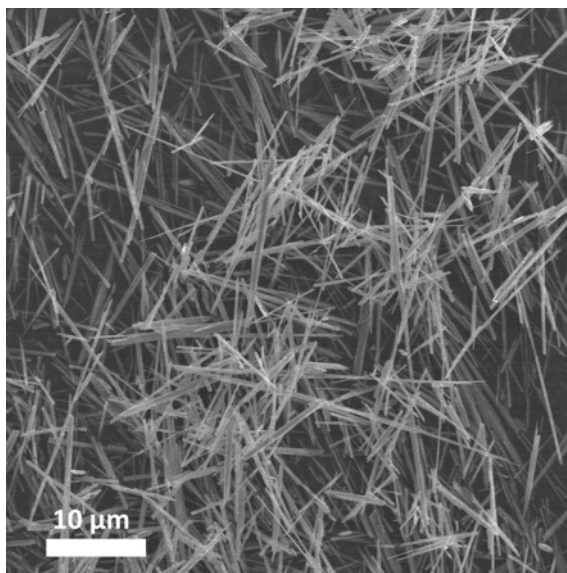


Figure 1.1 SEM images of MnO₂ NWs fabricated through hydrothermal method.

More exotic versions of the hydrothermal syntheses have also been explored, in order to increase the reaction kinetics and/or push the phase space of accessible new materials. Phuruangrat et al.⁵⁰ synthesized hexagonal WO₃ NWs for the first time using a microwave-assisted hydrothermal method producing materials that prove to be excellent catalysts for the hydrogen evolution reaction. Yeo et al.⁵¹ utilized laser-induced hydrothermal growth to grow localized ZnO and TiO₂ NW arrays on temperature sensitive substrate. The biggest drawback of hydrothermal approaches remains the fairly low maximum pressure, which is restrained by the relatively low reaction temperature limit decided by the reactor materials.

1.2.3 Metal-catalyzed syntheses

Another bottom-up approach to 1-D nanostructures is metal-catalyzed synthesis, and it is most frequently employed through the vapor-liquid-solid (VLS) synthesis mechanism, first proposed by Wagner⁵² in 1964. The general mechanism is shown in the

schematic Fig. 1.2. Metal catalysts (typically Au NPs) absorb the vapor precursor and form a liquid alloy. On supersaturation, the crystalline whiskers precipitate and grow from the liquid as solid single-crystalline NWs. The mechanism was further studied by Wu et al.⁵³ and found to have three well-defined stages: metal alloying, crystal nucleation, and axial growth. This VLS synthesis has been applied tens of thousands of times and represents a ubiquitous method of NW synthesis, covering single elements, tetrelides, pnictides, and chalcogenides, including Si,^{54,55} Ge,⁵⁶ TiC,⁵⁷ GaN,⁵⁸ and ZnO⁵⁹ etc.

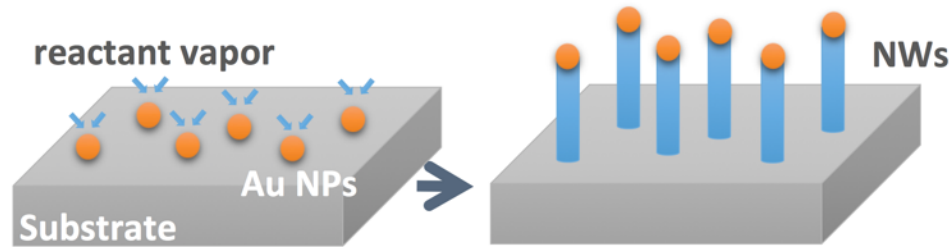


Figure 1.2 Cartoon showing VLS growth mechanism

The VLS mechanism conveys enormous control over the NW growth process with respect to most other methods. For instance, the diameter and length of the NW can be dictated by the size of the catalyst particle, and the growth time respectively.⁵² Also, vertical growth of NWs is attainable if a careful choice of substrate is made, to ensure a homoepitaxial relationship, or a heteroepitaxial junction with only a small lattice mismatch between the NW and the substrate. For example, vertical arrays of Si NWs can be grown from single crystalline Si substrates,⁶¹ and ZnO will grow vertically aligned on the a-plane of a sapphire substrate⁶². Figure 1.3 shows the irregular and vertical growth of ZnO NWs grown on Si and sapphire substrates respectively. Interestingly, the types of metal catalysts might also affect the growth direction of the NWs. Kuykendall et al.⁶³ found that GaN NWs grew in the direction of a-axis or the m-axis from an a-Al₂O₃

substrate using Ni or Au as the catalyst respectively. The major drawback of the VLS growth approach is the presence of unintended contamination within the NWs by the catalyst.^{64,65}

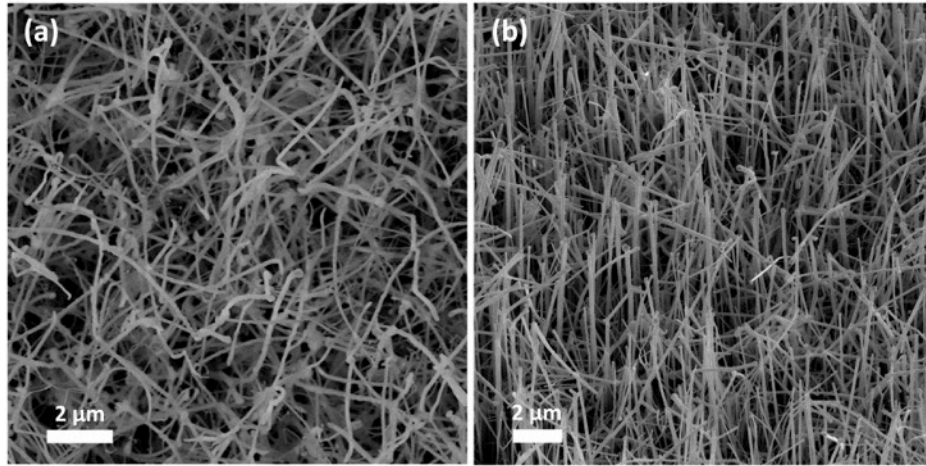


Figure 1.3 SEM images of ZnO NWs growth on (a) Si substrate and (b) sapphire substrate

The reverse of VLS growth, is a material etching method dubbed the solid-liquid-vapor (SLV) process, which our group is developing to grow nanosized holes (“negative NWs”) within a single-crystalline matrix. In a SLV dissolution process, diffusion from the solid into the metal suppresses the liquidus of the resulting solid solution, inducing the particle to melt. Continued diffusion into the now alloyed droplet continues, until supersaturation occurs and the reactant vapor leaves the particle at the liquid–vapor interface. If the driving forces, such as low pressure and/or a reactive chemical atmosphere, are maintained, the metal droplet can be induced to etch the crystal. Schematics of this process are shown in Fig. 1.4a for the SLV dissolution of an entire NW and in Fig. 1.4b for the SLV creation of NNW arrays.⁶⁶ More about SLV process will be discussed in Chapter 4.

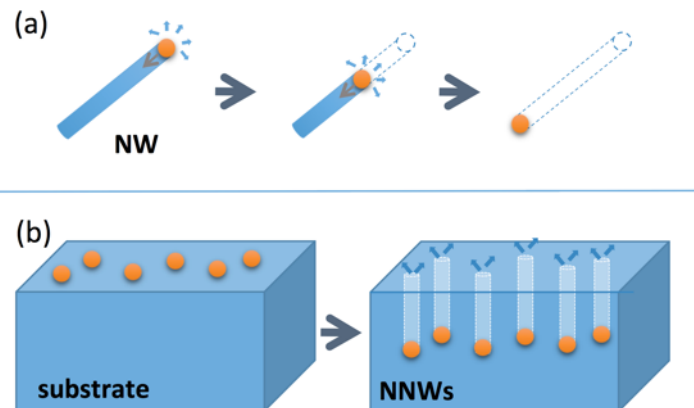
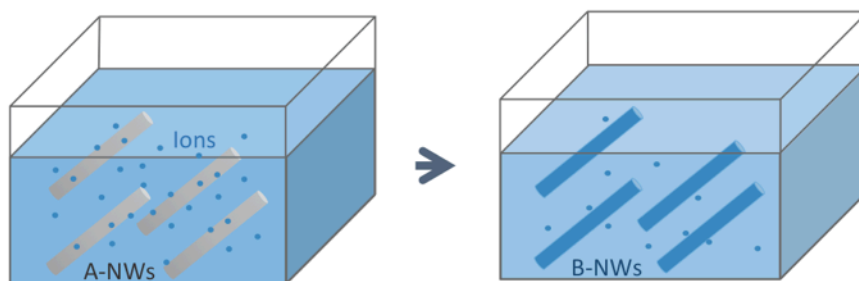


Figure 1.4 Cartoon showing (a) SLV dissolution of a single NW and (b) SLV formation of negative NWs.

1.2.4 Solid to solid transformations

For some materials, it is difficult to synthesize them into a NW morphology directly. In this case, materials for whom synthesis as a 1D nanostructure is facile can be used as chemical templates, to generate new 1D materials through a secondary reaction in which the original 1-D morphology is preserved. The second morphology-preserving step can be achieved through solution-phase, vapor-phase, or solid-state reaction, as shown in Fig. 1.5, utilizing nanocrystals as starting materials eliminates some of the disadvantages of traditional solid-state reactions using larger-sized powders, such as the necessity for diffusion over long distances, and large strain nucleation barriers.⁶⁷

(a) ion exchange reaction



(b) vapor phase diffusion



(c) solid state transformation

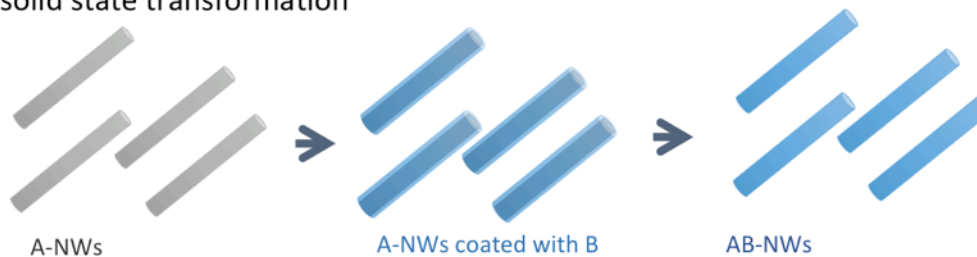


Figure 1.5 Cartoon showing three types of solid-to-solid transformation of NWs: (a) ion exchange reaction, (b) vapor-phase diffusion and (c) solid-state transformation

Phase transitions in solution phase can either be accomplished through anion or cation exchange, in which ion exchange happens when precursor NWs are mixed with other anion or cation sources in solution to get new phases, with the NW morphology maintained. Recently, Zhang et al.⁶⁸ synthesized CsPbCl_3 , CsPbI_3 , and CsPbX_3 alloy NWs through the fast anion exchange reaction of CsPbBr_3 NWs and other halide precursors. Similarly, Xia^{69–71} and co-workers have shown control over the synthesis of metal chalcogenide NWs utilizing cation exchange reactions. In these experiments, as-

obtained trigonal-Se (t-Se) NWs were reacted in solution with Ag^+ cations, resulting in Ag_2Se NWs. Interestingly, the crystal structure of the resulting Ag_2Se NWs depends on the size of the t-Se NWs, with tetragonal and orthorhombic Ag_2Se NWs obtained when the diameter of t-Se NWs is smaller or bigger than 40 nm respectively. Further, they transformed the Ag_2Se NWs to CdSe NWs via a second cation exchange process. Moreover, tubular CdSe can be obtained if the Se NWs are initially just partially converted, by controlling the extent of transformation. The topotactic relationship (involving displacement and exchange of atoms within crystal lattice) between the parent solid and the resulting species is the key to the single-crystal to single-crystal transformation in solution phase.

The solid-to-solid transformation in the vapor-phase is also being widely used. Yang⁷² and co-workers used this method to synthesize MgB_2 NWs by reacting B NWs with Mg vapor. Various transition metal phosphides, such as FeP, CoP, Cu_3P , $\text{Fe}_x\text{Co}_{1-x}\text{P}$,⁷³⁻⁷⁷ can also be synthesized in this way, for which the hydrothermally obtained transition metal hydroxide or oxide NWs undergo a low-temperature phosphidation reaction with a phosphorus-containing vapor source. Oxidization of a precursor NW also falls into this category, and is among the simplest class of solid-solid transformations since it involves the simple reaction of a NW with oxygen in the air. For example, Kolmakov et al.⁷⁸ figured out a topotactic transformation from Sn NWs to SnO_2 NWs, going through a lower temperature oxidation to form a SnO shell used to retain the NW morphology, followed by a fast, higher temperature, oxidation to form SnO_2 NWs. Li et al.⁷⁹ synthesized core-shell Bi- Bi_2O_3 NWs by oxidizing Bi NW arrays under slow heating, and single crystal Bi_2O_3 nanotubes were obtained when this was followed by a quick

heating process. Shan et al.⁸⁰ synthesized porous ZnO NWs and ZnCdO NWs by oxidizing ZnSe and ZnCdSe NWs respectively. In these cases the nanopores in the NWs are believed to result from rapid oxidation occurring at defects and boundaries, breaking the continuous NW into small particles.

Finally, solid-state transformations of NWs are another very important route for NW synthesis, in which material exchange with an external precursor may or may not occur. For the former scenario, the synthesis of metal silicide NWs is a good example. Numerous species of metal silicide NWs are synthesized through the reaction of Si NWs with sputter-coated metal layers, such as NiSi, NiSi₂, CoSi, Mn₄Si₇ and Mg₂Si etc.^{81–85} Similarly, some ternary spinel NWs such as ZnAl₂O₄⁸⁶ and LiMn₂O₄⁸⁷ are synthesized through reaction of metal oxide NW with another metal/oxide coating. Lithium, due to its small size and good diffusivity, has also been used to react with other NW species to form ternary NWs through a bias-induced lithiation process, such as Li₂V₂O₅,⁸⁸ LiV₃O₈,⁸⁹ Li_xSi,⁹⁰ Li_xSn,⁹¹ and Li_xGe⁹². Transformation of In₂Se₃ NWs to CuInSe₂ NWs by reaction of precursor NWs with contacted copper on two ends⁶⁷ or coated copper⁹³ were reported by Cui's group, in which the transformation temperature largely dictates the crystal orientation of the long axis for In₂Se₃ NWs. Examples of solid-state phase transformation of NWs without external reactant include the dehydration and decomposition of parent precursor NWs, such as the formation of NiO NWs resulting from the heat treatment of Ni(OH)₂,⁹⁴ as well as pure-phase structural transformations, such as that displayed by the cubic to orthorhombic phase transformation of FeSi₂ NWs,⁹⁵ and the κ- to α-phase transformation of In₂Se₃.⁸⁵

1.3 *In situ* transmission electron microscopy

1.3.1 Introduction

Electron microscopy uses a beam of accelerated electrons as illumination sources to create images of materials, and enables the resolution of structures on the micro-/nano-scale, unattainable by conventional light microscopy. The first electron microscope was invented in the 1930s; in less than 100 years it has become ubiquitous in the characterization of materials, evolving into an incredibly powerful tool with magnifications range of $\times 50$ to $\times 10,000,000$, and has been responsible for pushing the limits of material science.

In addition to the capability of atomic-resolution imaging, various attached analytical techniques enable the TEM to characterize crystallographic phases and orientation (by using electron diffraction), generate elemental maps (by using EDS and EELS), and images with elemental contrast (Z-contrast imaging) precisely in nano-scaled localized regions.

Traditionally, characterization methods have been used to study materials in a static state, before or after a reaction. To study the dynamics of a reaction mechanism, however, *in situ* methods are essential to acquire the missing information during the evolution of materials, such as the presence of metastable intermediate phases. *In situ* TEM enables us to monitor reactions in real-time and at atomic-resolution. High-resolution TEM imaging in combination with other techniques such as EDS, EELS, and SAED taken during the reaction, can further provide us with local information at the reacting interfaces.⁹⁶ Reactions in the TEM can be stimulated in several ways: radiating the sample with electrons or light,⁹⁷⁻⁹⁹ varying the temperature using an *in situ* heating holder,^{100,101} putting the sample in a solution or gaseous environment using special

sample holders or modified vacuum systems,^{102–105} performing local electrochemical reactions,^{106,107} or by applying mechanical testing.^{108–111}

TEM characterization forms the backbone of much of the work reported in this thesis, to both characterize materials, and study the phase transformations of 1D nanomaterials. The following sections in this chapter will discuss breakthroughs in 1D nanostructure synthesis using *in situ* TEM. The operation of the TEM will be discussed in chapter 2.

1.3.2 Studies on 1-D nanostructure synthesis using *in situ* TEM

As mentioned above, ternary and quaternary NWs can be synthesized by reacting a simpler and readily available binary NW with compounds containing the additional desired elements. Recently, *in situ* TEM has been widely used to study this type of reaction. Schoen et al. used *in situ* heating within the TEM to induce the reaction of In_2Se_3 NWs with Cu, and observed the formation of single-crystalline CuInSe_2 NWs.¹¹² In this experiment, real-time observation of the reaction revealed that the transition temperature strongly influences the crystal orientation of the NW. Wu and co-workers synthesized and studied the growth behaviors of series of heterostructure NWs, including CoSi_2 ,¹¹³ NiSi ,⁸¹ and MnSi ,¹¹⁴ in Si NWs, and ZnO in Al_2O_3 NWs,¹¹⁵ based on a similar design by annealing the starting NW with another material either in point or line contact in TEM.

In situ heating within TEM was also been employed to study the growth mechanism of NWs. Persson et al.¹¹⁶ investigated GaAs NW growth via *in situ* TEM, in which the NW was discovered to grow via a vapor-solid-solid (VSS) solid-phase diffusion mechanism, through the diffusion of elements from the solid metal alloy seed, in contrast to the more widely studied VLS mechanism for semiconductor NW growth.¹¹⁷ In this

case, the solid seed particle was found to be an alloy of only Au and Ga during growth, without the presence of As. This is in direct contrast to the case of In_2Se_3 , the growth of which was also studied using *in situ* heating in the TEM, revealing a VLS growth mechanism via a liquid Au-In-Se alloy droplet. More recently, Boston et al.¹¹⁸ performed a microcrucible synthesis for quaternary metal oxide Y_2BaCuO_5 NWs within the TEM. The presence of a catalytic barium carbonate NP and a porous matrix containing copper and yttrium oxide in this case enabled migration of the NP, leading to the growth of NWs out from the surface.

In addition to NW growth, NW etching/dissolution/sublimation has also been studied using *in situ* TEM. In our own group, Hudak et al.¹¹⁹ studied the evaporation of SnO_2 NWs via the SLV mechanism (see section 1.2.3 above), catalyzed by a gold nanodroplet. Later, Hsin et al.¹²⁰ studied the sublimation of In_2Se_3 within an $\text{In}_2\text{Se}_3/\text{In}_2\text{O}_3$ core/shell NW, revealing two mechanisms at the exposed In_2Se_3 surface: mass desorption and stepwise migration.

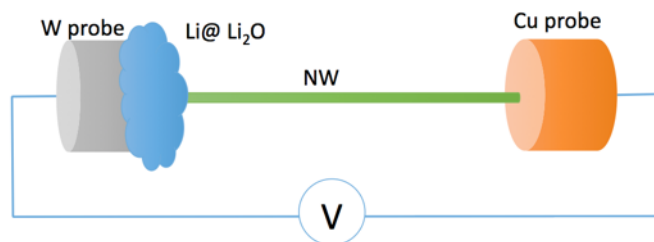


Figure 1.6 Schematic graph showing an experimental setup for solid nanobattery cell in TEM

Finally, the electrochemical behavior of NWs as battery electrodes, such as for lithium and sodium ion batteries (LIB and SIB) can also be studied using *in situ* TEM techniques. Figure 1.6 shows a typical experimental setup for a solid nanobattery cell, in which a NW is mounted to a copper probe and used as a working electrode, while a piece

of Li metal is mounted on a tungsten probe as a counter electrode, with a native Li_2O layer performing as a solid-state electrolyte. Using a similar setup, Liu et al.⁹² studied the electrochemical lithiation/delithiation behavior of a Ge NW, and observed directly the formation and progression of nanopores in this material for the first time, as well as the reversible expansion and contraction of the NW, providing insight into the mechanism of microstructure evolution for Ge electrodes. More recently, researchers have studied extensively the lithiation/delithiation behaviors of other 1D nanostructures, such as amorphous silicon coated carbon nanofibers,¹²¹ Si NPs attached to carbon nanofibers,¹²² Si NWs,¹²³ ZnO NWs,¹²⁴ NaV_3O_8 ,¹²⁵ and $\alpha\text{-V}_2\text{O}_5$.⁸⁸ Additionally, Lu et al.¹²⁶ has recently studied the sodiation behavior of Ge NWs via *in situ* TEM, for which sodium metal was used instead of lithium.

Chapter 2 Experimental methods

2.1 Sample preparation

2.1.1 Hydrothermal syntheses of metal oxide nanowires

Hydrothermal methods are used to prepare the precursor NWs for further spinel NW synthesis, and iron oxy-hydroxide NWs for *in situ* TEM experiments. The reactor consists of two parts: the stainless steel autoclave vessel and the Teflon liner, as shown in Fig. 2.1. In a typical synthesis, a well-mixed solution of reactants is transferred into the Teflon-lined stainless steel autoclave, assembled and sealed, and maintained at the reaction temperature for a certain amount of time. After the system is cooled down, the product is collected and washed several times with distilled water, and dried at 60 °C overnight.



Figure 2.1 Schematic picture of hydrothermal reactor showing (A) showing components of hydrothermal reactor, stainless steel autoclave vessel and Teflon liner, and (B) the assembled hydrothermal reactor.

2.1.2 Pulsed laser deposition for thin film growth

Pulsed laser deposition (PLD) is a physical vapor deposition technique to grow high-quality films, which utilizes a high energy focused pulsed laser beam to strike and remove materials from the surface of a target in an ultra high vacuum. The vaporized material is then deposited on a substrate, which is placed facing the target. A KrF excimer laser ($\lambda = 248 \text{ nm}$) with a fluence of 1.6 J/cm^2 was used in this study to grow SnO_2 thin films for SLV etching.

2.2 Characterization

2.2.1 Powder X-ray diffraction

Powder X-ray diffraction (XRD) was used to identify the crystal phases of our powder samples. XRD detects constructive interference of incident X-rays scattered from atomic planes in crystals, producing peaks under the condition that the diffracted rays satisfy Bragg's law ($n\lambda = 2d \sin \theta$). XRD not only provides information about the unit cell dimensions, but can also reveal the phase-purity of samples by uncovering impurity peaks. XRD patterns were collected on a Bruker-AXS D8 Discover diffractometer. Powdered materials were scanned with $\text{CuK}\alpha$ radiation (1.5418 \AA) from 10° - 70° (2θ). The XRD patterns were compared with standards from the database, e.g. international center for diffraction data (ICDD), and/or indexed using simulations calculated patterns (CrystalMaker software suite).

2.2.2 Scanning electron microscopy

Scanning electron microscopy (SEM) produces images using a focused electron-beam, which is scanned across the sample in a raster pattern. When the incident electrons

interact with the atoms of the specimen, energy may be lost through several processes, This energy may be converted via conversion to elastic electrons (backscattered electrons), inelastic electrons (secondary and Auger electrons), cathodoluminescence photons, and/or X-rays, as shown in Fig. 2.2, all of which convey information about the surface and the properties of the material.

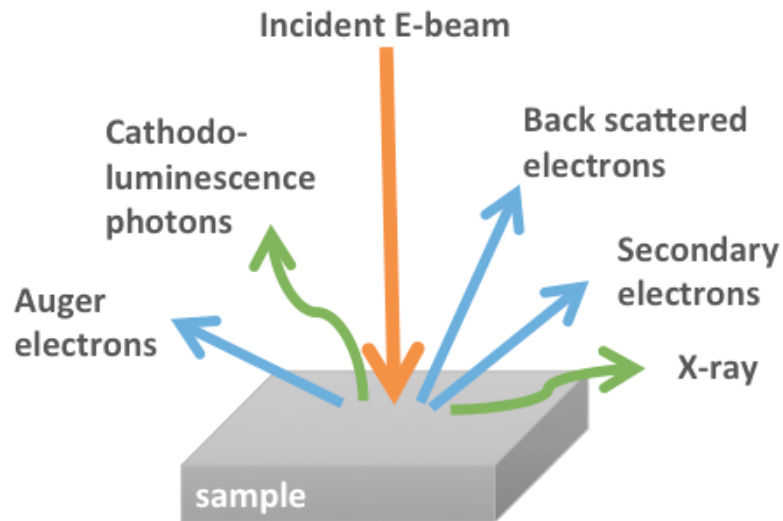


Figure 2.2 Diagram illustrating the interactions of the incident electron-beam with the sample in the SEM

The two most common imaging modes in SEM are secondary electron (SE) imaging and backscattered electron (BSE) imaging, providing mainly topological information about the surface of the sample and its mass (atomic number) information at the nanoscale, respectively. The SEM images in this dissertation were taken on Hitachi S4300SE using SE imaging mode at a voltage between 15 kV and 20 kV.

2.2.3 X-ray photoelectron spectroscopy

X-ray photoelectron spectroscopy (XPS) is a surface analysis technique used to measure the elemental composition (except H and He), the chemical state, and the electronic state, of elements from the surface of solid materials.¹²⁷ When the sample surface is irradiated with incident X-rays, the energy is transferred to a core-level electron. When sufficient energy is incident, the electron will be ejected away from the nuclear attraction force with a kinetic energy characteristic of the incoming photon, and the particular element. The energy and intensity of emitted photoelectrons are then collected and analyzed. Characteristic bonding energy can be calculated by subtracting the measured kinetic energy from the energy of the incident X-rays.

In this dissertation, XPS was performed for the as-synthesized manganese-containing spinel NWs to identify the oxidation states for the cation species. X-rays generated by a Mg K- α source (1253.6 eV, PHI 04-548 Dual Anode X-ray source), an 11 inch diameter hemispherical electron energy analyser with multichannel detector, with pass energies of 23.5 eV and 0.025 eV step sizes (PHI 5600) and a Thermo Scientific Model K-Alpha XPS instrument, with a monochromated, microfocusing Al K α X-ray source (1486.6 eV) were used. The base pressure in the analysis chamber is typically 2×10^{-9} mbar or lower. Survey spectra (0-1350 eV) were acquired with a pass energy of 200 eV and the high-resolution spectra were collected with a pass energy of 50 eV. Peak fitting was performed using mixed Gaussian/Lorentzian peak shapes and a Shirley/Smart type background.

2.2.4 Linear sweep voltammetry

Linear sweep voltammetry (LSV) is used to test our products' ability to catalyze the oxygen evolution reaction (OER) in alkali solution. We used a three-electrode system, which comprises a counter electrode (CE), a working electrode (WE) and a reference

electrode (RE), as shown in Fig. 2.3. The three electrodes were immersed in alkali solution, with potential catalyst material for testing cast on the tip of the working electrode. A cycling potential was applied to the working electrode versus the reference electrode. During the potential cycling, the current between the working electrode and the counter electrode was measured.

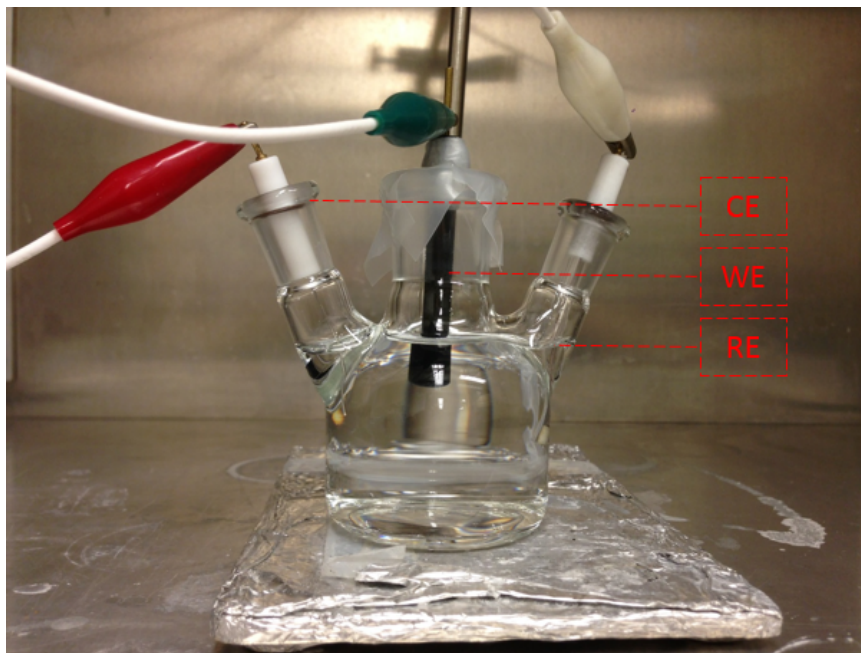
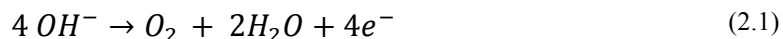


Figure 2.3 Linear sweep voltammetry set-up comprising counter electrode (CE), working electrode (WE) and reference electrode (RE).

Linear sweep voltammetry (LSV) curves were obtained with a scan rate of 10 mV/s in the potential range of 0-1V vs. Ag/AgCl. We used a Pt wire as the counter electrode, silver/silver chloride (Ag/AgCl) as the reference electrode, and a 0.1 M KOH solution was used as the electrolyte. For the working electrode, the mixture of catalysts and carbon black were deposited onto a glassy carbon (GC) current collector (diameter = 4mm). 3 mg of catalyst mixed with 7 mg of carbon black were dispersed in 1 mL of acetone by sonicating for 30 minutes. Carbon black was added to increase the

conductivity. 6 μL of the as-prepared catalyst solution was dropped on the GC. After drying, 3 μL of 2.5 wt % nafion was then applied to the catalyst. The current density (A/cm^2) was obtained by normalizing the measured current by the geometric area of the electrodes. A difference in surface roughness of each electrode was not corrected for. Finally, the LSV curves of the spinel NWs for the oxygen evolution reaction were corrected for iR effect. The electrical resistance (R) of the NW electrode was determined by electrochemical impedance spectroscopy at the DC potential of 1.0 V vs. Ag/AgCl. LSVs were plotted as a function of potential versus hydrogen electrode (RHE).

The performance of the catalyst towards the oxygen evolution reaction (equation 2.1) was evaluated by two factors, the onset potential and the current density, which can be determined from the CV curves.



A large increase in current occurs at the onset potential due to electrons produced by the OER.

2.3 Transmission electron microscopy

2.3.1 Principles of transmission electron microscopy

In a TEM, a high-energy electron-beam is produced and emitted from a gun through thermionic or field electron emission into vacuum. The as-produced electron-beam is then manipulated and directed by a magnetic field, analogous to a lens in optical microscopy, passing through and interacting with a thin sample specimen. The transmitted electrons are then focused to produce high-resolution images. High-resolution is possible due to the short wavelength of electrons accelerated through the high voltages used, based on the relationship between resolution and wavelength as shown in equation

2.2, where δ is the smallest distance that can be resolved, λ is the wavelength of radiation, μ is the refraction index of the viewing medium, and β is the semi-angle of collection of the magnifying lens. To simplify the expression, the $\mu \sin \beta$ term may be approximated to unity.

$$\delta = \frac{0.61 \lambda}{\mu \sin \beta} \quad (2.2)$$

The electron wavelength may be estimated using De Broglie's equation (equation 2.3), where the energy of the electron, E , is measured in electron volts (eV), and its wavelength, λ , is in nanometers (nm).

$$\lambda = \frac{1.22}{\sqrt{E}} \quad (2.3)$$

Combining equations 2.2 and 2.3 above thus produces the following expression for resolution:

$$\delta = \frac{0.74}{\sqrt{E}} \quad (2.4)$$

The maximum possible resolution for a 200 keV electron-beam would therefore be ~ 0.0016 nm. Lens imperfections limit the resolution, however, such that the wavelength-limited limit of resolution can never be obtained. To this end one of two approaches are typically employed: (1) increasing the accelerating voltage, or (2) employing spherical (C_s) and/or chromatic (C_c) aberration correctors. In recent years the development of aberration-correction techniques has been transformative to field of microscopy thanks to the ultra-high resolutions obtainable.

The most common operation mode in TEM is bright-field imaging. In this mode, the electron-beam passes through the condenser lens system, and is scattered by the specimen. The transmitted electrons pass through the apertures and are focused in the back focal

plane, producing a magnified projection of the specimen onto the viewing fluorescent screen with intermediate lens and projector lens or can be also recorded digitally by a CCD camera. At low resolution, the contrast in bright-field mode comes from the variation in thickness and density in the sample. Thicker, denser or heavier atom areas block more electrons and thus appear dark in the image, while on the contrary, regions in which are thinner, or have lower density and/or lighter atoms (including the vacuum) would appear bright.

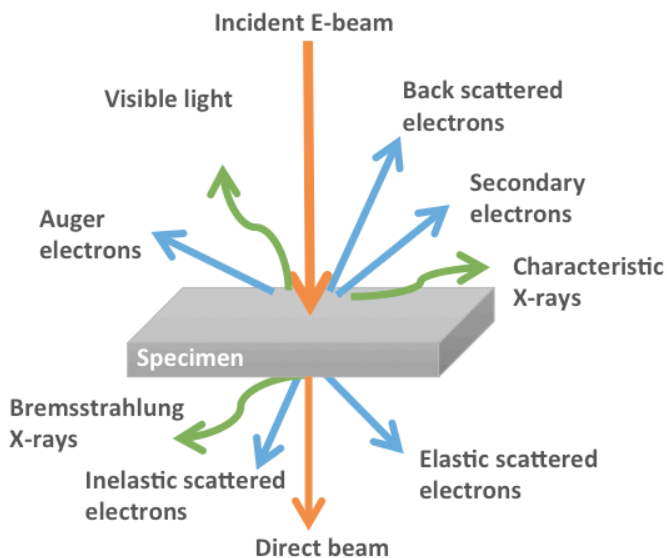


Figure 2.4 Cartoon depicting the interactions of incident electrons with the specimen in a TEM

2.3.2 Scanning transmission electron microscopy

In addition to the directly transmitted beam, there are many secondary signals, as shown in Fig 2.4, produced when the incident electron-beam interacts with atoms in specimen, due to the ionizing nature of electrons.¹²⁸ Many of these secondary signals, such as characteristic X-rays and inelastically scattered electrons, are used in analytical electron microscopy (EDS and EELS respectively), providing us chemical information

and other details about the specimen. To achieve a localized signal, a very small beam or probe may be produced by the TEM, usually less than 5 nm, in which case the scanning mode of TEM (or STEM) is obtained. By combining the STEM with high-angle detector, high-resolution imaging with atomic number contrast is possible, in which, the electrons are scattered with low angle by light elements while heavier atoms scatter electrons to a high angle. This mode is the subject of the next section. Scanning transmission electron microscopy

Very similar to SEM, in STEM mode, the electron-beam (or probe) is convergent to sub-nanometer size and scanned over a selected region of the specimen in a raster fashion. Unlike in TEM mode, where the straight-through electrons are used to generate images, in STEM mode, scattered electrons are instead collected to create images, with annular detectors being used simultaneously as shown in the Fig. 2.5. While collecting high resolution images in STEM mode, spectroscopic signals such as characteristic X-rays and low-angle scattered electrons can be collected at the same time, which enables complimentary atomic resolution EDS and EELS mapping respectively.¹²⁹

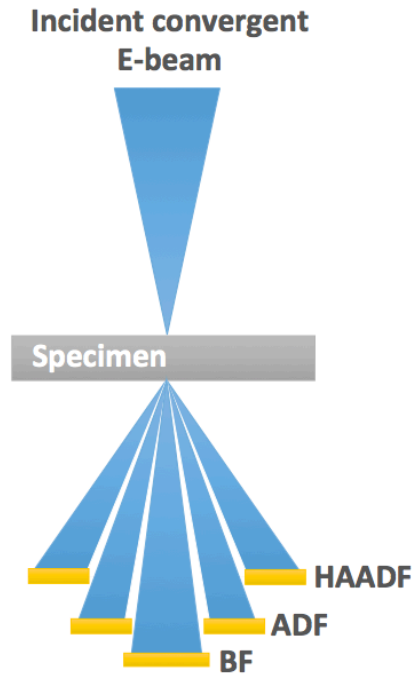


Figure 2.5 Schematic diagram depicting HAADF, ADF and BF detectors in the STEM

Images collected at high angle (usually >50 mrad) with respect to the original beam propagation by a high-angle annular dark field detector (HAADF) are called HAADF images, and also sometimes referred to as Z-contrast images. Electrons at high angle are mainly incoherently scattered (also called Rutherford scattering), and the intensity of the image strongly depends on the atomic number (Z^2), and is least affected by inelastically or Bragg scattering at lower angle relating to sample thickness.^{128,130} For HAADF, or Z-contrast, imaging, atoms with higher atomic number scatter more strongly, producing a bright signal, and lighter atoms or areas without material appear dark.

2.3.3 Energy dispersive X-ray spectroscopy

Energy dispersive X-ray spectroscopy (EDS) is very useful in localized elemental analysis. When the electron-beam interacts with atoms in the specimen, the electron in

the inner shell may be knocked out forming an electron hole, and the hole would be filled rapidly by electrons of high energy from an outer shell. The energy difference between the two energy levels can be released in the form of an X-ray (Fig. 2.6) The emitted X-rays are then collected by EDS detectors, generating a spectrum with counts of X-rays as a function of X-ray energy. Each elemental atom has its unique set of X-rays due to its distinctive atomic structure. Thus, such characteristic X-rays spectra can be used to identify the elemental species in the sample.

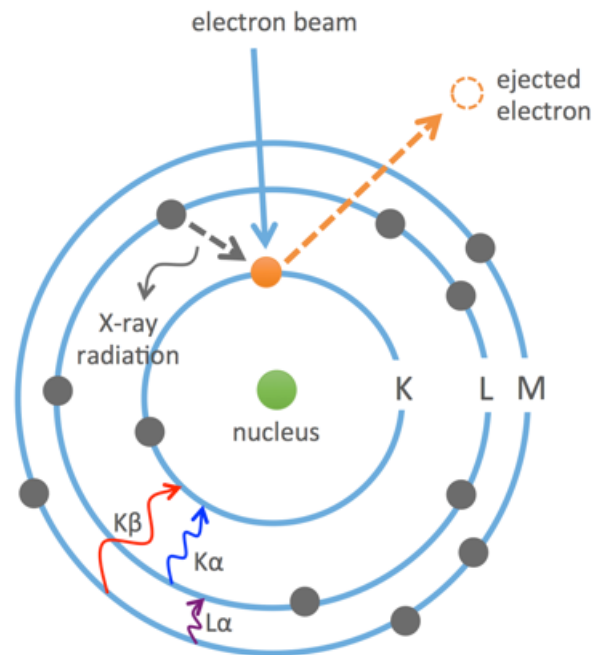


Figure 2.6 Schematic figure showing the emission of characteristic X-rays as a result of interactions of the incident electron-beam and atom

Both qualitative and quantitative analysis can be performed using EDS, though there are some detection limits. For example, only elements above lithium in the periodic table can in principle be detected by EDS, and EDS has fairly low energy resolutions (>100

eV). Some of these challenges may be addressed with a complementary technique EELS, which will be discussed in the following section.

2.3.4 Electron energy loss spectroscopy

When the electron-beam interacts with the atoms of the specimen, inelastic scattering can occur, resulting in energy loss of the incident electrons. Measurement of these energy losses form the signal for EELS, which therefore provides information about the local physical and chemical environment of specimen. In a typical EEL spectrum (Fig. 2.7), the peak at zero energy is known as the zero-loss peak (ZLP), and represents the electrons transmitted elastically, without any measurable energy loss. Low-energy losses (less than 50 eV) are primarily due to excitations of valence shell electrons, which are usually interpreted in terms of band structure, band gap, surface plasma etc.^{131, 132} Energy losses greater than 50 eV are from inelastic scattering with inner-shell electrons, showing as “ionization edges” (due to their cliff-shape) in the spectrum, and are known as core-loss peaks. The edges are formed when inner electrons are excited to a state above the Fermi level upon absorbing enough energy from the incident beam, and the energy lost by the incident beam is recorded in the spectrum. Since the ionization energies of elements are characteristic of the core energy levels, those core-loss peaks can be used to identify elemental species without the detection limits for light elements in EDS.

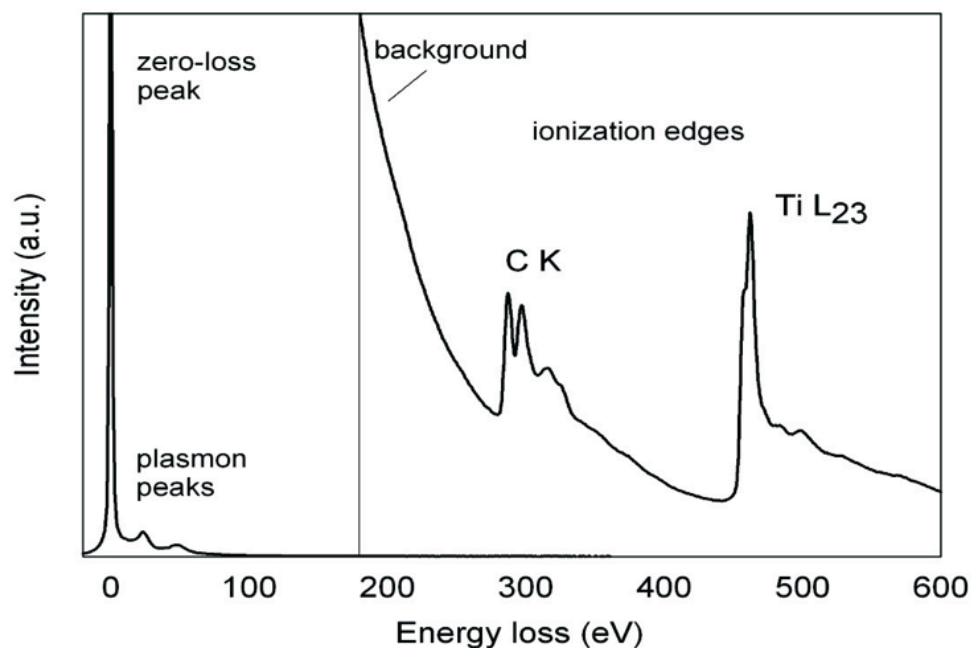


Figure 2.7 EELS spectrum of a 20 nm thin titanium carbide specimen¹³² (Figure adapted from Ref. 132)

In combination with high-resolution STEM imaging, an EEL spectrum may be acquired for each pixel for an image, gathering a data cube known as a spectrum image, allowing energy losses to be mapped as a function of spatial variants x and y . A recent advance in EELS includes the introduction of a monochromated electron source, commonly improving the energy resolution to less than 0.1 eV, opening up the potential for detailed studies on electronic structure and bonding effects through near edge fine structure of the ionization edges, and accurate band gap and dielectric function measurements from the low-loss region.^{132,133}

In this dissertation, applications of EELS are introduced in chapter 5 to identify the oxidation state changes of iron cations during phase transformation, which unravel the phase transition from γ -Fe₂O₃ to the isostructural polymorph Fe₃O₄.

2.3.5 *In situ* heating within TEM

In situ heating in the TEM has been widely used to study the crystal growths or segregations,^{134–136,118,137,138} phase transformations,^{139–141} lithiation behaviors for battery materials,^{88,92,121–123,125,126,142–144} melting or evaporation behaviors of nanocrystals,^{119,145,146} and other phenomena. Current state-of-the-art TEM heating holders are based on microelectromechanical systems (MEMS) chip technology. These chips consist of a Si-based substrate, overlaid by a thin film featured with electron transparent windows for heating and TEM analysis. Ultra fast temperature changes (up to 1200 °C) with high stability can be applied via dielectric resistive heating through electrodes connected to the thin film.¹⁴⁷

For our *in situ* heating experiments, we use a commercially available Protochip Aduro holder and thermal E-chips, which enable us to make ultra-fast temperature changes (1×10^6 °C/s) within the temperature range from room temperature to 1200 °C with high stability, shown in Fig. 2.8 (Protochip, Inc).

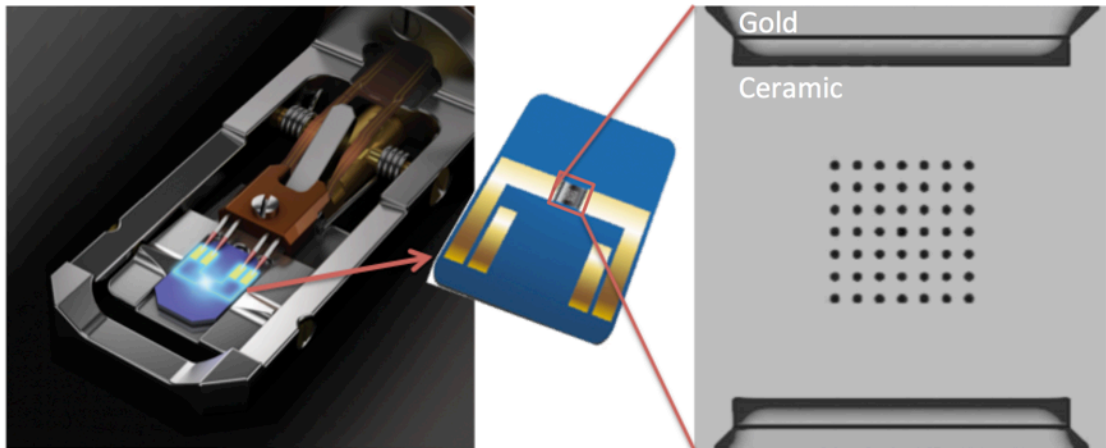


Figure 2.8 Details of Protochips Aduro E-chip.

E-chips are constructed with a ceramic window to perform as heating membrane, with 7 μ m holes spaced 7 μ m apart to allow electron-beam transmission. E-chips may be overlaid with SiN film, holey carbon film or no film; for the work discussed in this thesis a holey carbon overlay was used throughout. The holey carbon layer is 20 nm thick with 2 μ m holes spaced 2 μ m apart. Gold electrodes attached to the ceramic apply resistive heating to the sample.

All samples for *in situ* heating were suspended in solvent, and then drop-casted onto Protochips E-chips. The E-chips are then dried in an oven at 60 °C for 15 min. The E-chips are loaded in a Protochips Aduro heating holder, and used to perform *in situ* TEM heating experiments.

All samples for *in situ* heating were suspended in solvent, and drop-cast onto the Protochips E-chip. The E-chip is then dried in an oven at 60 °C for 15 min, loaded into a Protochips Aduro heating holder, and used to perform *in situ* TEM heating experiments.

Chapter 3 Manganese-containing nanowires with the spinel crystal structure

Parts of this chapter are taken from “Simple Synthetic Route to Manganese-Containing NWs with the Spinel Crystal Structure”, *Journal of Solid State Chemistry*, 2016, 8, 23-29.²²

3.1 Introduction

Manganese-containing spinels have interested researchers for decades, both for the versatility of the spinel-type crystal structure having many interstices, and for the multiple oxidation states of manganese and different properties of the resulting spinels. Spinel such as Fe_3O_4 ,^{148,149} Mn_3O_4 ,^{150,151} and LiMn_2O_4 ,^{152,153} for example, are known to perform well as electrodes for lithium ion batteries; of particular interest are the tests performed by Thackeray et al.¹⁵⁴ and Feltz et al.¹⁵⁵ who tested the lithiation kinetics for manganese-containing spinels MMn_2O_4 (M = Mn, Mg, Li), and found the reducibility of the manganese cations was a crucial factor for lithiation. Besides their use as battery electrodes, manganese-based spinels are also good catalysts for oxidation and reduction reactions:¹⁵⁶ CdMn_2O_4 can be used as an electrode material for NO gas sensors;¹⁵⁷ NiMn_2O_4 ,¹⁵⁸ mesoporous MnCo_2O_4 ,¹⁵⁹ and high surface area CuMn_2O_4 ¹⁶⁰ have been shown to catalyze CO oxidation at ambient temperatures, exhibiting robust stabilities. Cu-Mn spinel oxides are also highly active for production of H_2 from methanol.¹⁶¹ In addition, manganese spinels are reactive towards electro-organic redox catalysis with comparative stability.¹⁶²

Since Tarascon et al. found that nanoscale transition-metal oxides were able to enhance lithium reactivity,¹⁴⁸ which is fundamental for lithium ion battery performance,

researchers have studied several promising nanoscale metal oxides, particularly nanoscale manganese-containing spinels. Based on this research, these nanoscale spinels have better performance than bulk materials for lithium ion batteries.^{163, 164} Additionally, nano-sized manganese spinels are also more desirable for catalytic processes taking place at active surfaces, since they have larger surface-to-volume ratios than dense spinels. Though some reports exist on the synthesis of manganese-containing spinels with NP^{165, 166-168} and nanorod (NR)¹⁶⁹ morphology, a NW morphology is still quite challenging to synthesize and only a limited number of reports regarding the manganese-containing spinel NW synthesis exist. For example, Hosono et al.¹⁷⁰ and Lee et al.⁸⁷ reported the synthesis of single crystalline LiMn_2O_4 NWs by hydrothermal and solid-state methods respectively; Song et al. synthesized manganese-gallium oxide NWs with a minor MnGa_2O_4 spinel phase;¹⁷¹ and Chen et al. obtained MnCr_2O_4 NWs by heating stainless steel foil;¹⁷² and Na et al. synthesized Mn_2SnO_4 NWs using a chemical vapor deposition method.¹⁷³ To date, however, no reports exist for the synthesis of single-crystalline NWs of Mg_2MnO_4 or CuMn_2O_4 .

Cubic Mg_2MnO_4 forms the inverse spinel structure, with half of the Mg^{2+} ions in the tetrahedral A-sites, and the octahedral B-sites occupied equally by Mg^{2+} and Mn^{4+} to maximize the crystal field stabilization energy of the Mn^{4+} cations, as shown in Fig. 3.1. Both Mg^{2+} and Mn^{4+} are critical in determining the functionality of this compound. Izawa et al. found Mg_2MnO_4 showed good lithium isotope selectivity in the ion exchange process in which Li^+ ions replace Mg^{2+} in the Mg_2MnO_4 .¹⁷⁴ Mg_2MnO_4 is also a good electrocatalyst for the oxygen evolution reaction, due to its high ion mobility enhanced by the tetravalent manganese ions within the spinel structure.^{175,176}

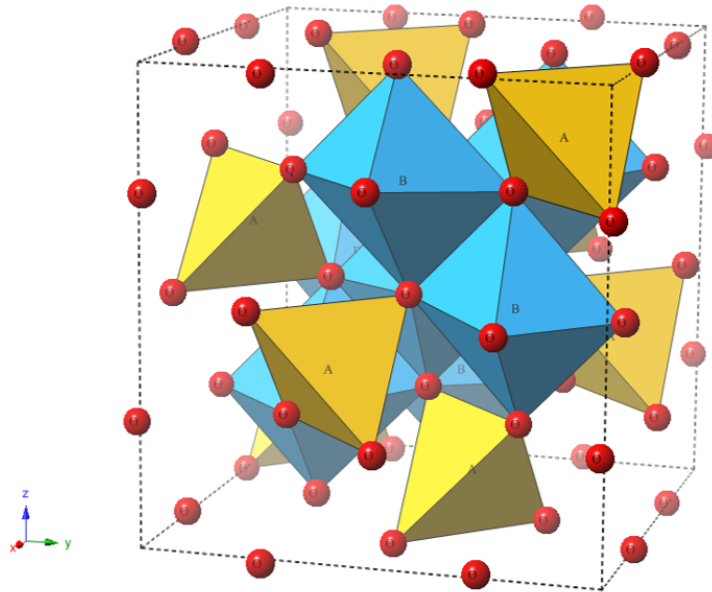


Figure 3.1 Structure of cubic spinel AB_2O_4

$CuMn_2O_4$ is known to exist in both a cubic^{177,178} and a tetragonal¹⁷⁹ phase, with differing structurally-dependent properties. Waskowska et al.¹⁸⁰ synthesized 0.8 inverted cubic $CuMn_2O_4$ which has Cu^+ and Mn^{2+} on the A-sites and Cu^{2+} , Mn^{3+} and Mn^{4+} taking B-sites. This coexistence of Mn^{3+} and Mn^{4+} cations on the octahedral sites is believed to be the driving force for its high electrical conductivity. Despite the presence of two Jahn-Teller (J-T) active ions, the proportion of Cu and Mn cations with the J-T active Cu^{2+} and Mn^{3+} oxidation states is smaller than the critical amount required to cause an overall J-T distortion,¹⁸⁰ and the structure therefore forms a cubic phase. The structure of tetragonal $CuMn_2O_4$, however, is more complicated than that of the cubic phase. Shoemaker et al.¹⁸¹ refined the tetragonal $CuMn_2O_4$ structure with c/a ratio of 1.03399 and a 0.27 inversion degree. In this tetragonal spinel, Cu^+ , Cu^{2+} , Mn^{2+} , Mn^{3+} ions all take tetrahedral sites, with octahedral sites occupied by Cu^{2+} , Cu^{3+} , Mn^{3+} , Mn^{4+} . In its bulk form, $CuMn_2O_4$ is

known to catalyze the oxidation of CO to CO₂ at room temperature,^{160,182,183} and the reduction of NO_x.¹⁸⁴

With the many useful applications of Mg₂MnO₄ and CuMn₂O₄ as enumerated above, it would be highly desirable to have a reliable, inexpensive, and scalable route for the production of single-crystalline NWs of these materials. 1-D nanomaterials have the advantage of possessing high aspect ratios and high surface areas, which are particularly crucial for catalyst applications, and may be fabricated into 2-D membranes for easier manipulation in industrial applications.^{185–188} In addition, since catalysts have preferred faces for catalytic activity,^{184,189} single-crystalline materials – especially those with specific crystalline facets – are needed. Given these reasons, and the fact that syntheses of ternary oxides in NW form can be notoriously tricky, we were intrigued by the report by Lee et al.⁸⁷ of LiMn₂O₄ NW synthesis, using a binary manganese oxide or oxyhydroxide NW precursor to essentially “lock-in” the NW morphology, and a simple solid-state reaction to convert the material to the desired ternary oxide spinel phase; this is a remarkable result given the very different crystal structures of the starting NWs (which are rutile-type) and the product (which are spinel-type).

In this project, we expand on the approach of Lee et al.,⁸⁷ to introduce a new route to synthesize other single-crystalline manganese-containing spinel NWs by the solid-state reaction of binary manganese-containing NW precursors with metal hydroxides. Our study is the first report of the synthesis of Mg₂MnO₄ or CuMn₂O₄ in single-crystalline NW or NR morphology. Powder X-ray diffraction (XRD), scanning electron microscopy (SEM), transmission electron microscopy (TEM), X-ray photoelectron spectroscopy (XPS) and linear sweep voltammetry (LSV) have been used to characterize phase purity,

crystal structure, morphology, oxidation states of elements, and electrochemical catalytic performance with regards to the oxygen evolution reaction (OER).

3.2 Methods

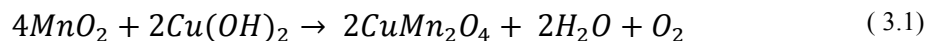
MnO₂ and γ -MnOOH NWs are grown *via* hydrothermal reaction as described in the literature.^{190, 191} For precursor MnO₂ NWs, 1.37 g MnSO₄·H₂O and 0.086 g NaClO₃ were dissolved in 36 mL distilled water and stirred for 15 minutes. The mixed solution was transferred to a 45 mL Teflon-lined stainless steel autoclave, assembled and sealed, and maintained at 160 °C for 18 h. After the system was allowed to cool to room temperature, the product was collected and washed with distilled water several times, then dried at 60 °C overnight. In a typical procedure for γ -MnOOH NWs, 0.63 g KMnO₄ and 0.45 g CTAB were dissolved in 36 mL distilled water and stirred for 20 minutes. The mixed solution was transferred to a 45 mL Teflon-lined stainless steel autoclave, sealed, and maintained at 180 °C for 12 h. The system was again allowed to cool to room temperature, the product collected and washed with distilled water several times, and then dried at 60 °C overnight.

To make CuMn₂O₄ NWs, a mixture of Mn-containing precursor NWs and well-ground Cu(OH)₂ with molar ratio 2:1 was dispersed with methanol in a crucible and stirred for 20 min to make an even mixture. This was dried on a hot plate to produce a pellet, which was annealed at 900 °C for 1-3 h in air. A similar procedure was applied to make MgMn₂O₄ and Mg₂MnO₄ NWs, using the correct molar ratio of Mn-containing precursor NWs and well-ground Mg(OH)₂. Samples were quenched in liquid nitrogen to reduce the formation of secondary impurity phases during cooling. Optimization of the experimental parameters (leading to the choice of the above conditions) revealed that

calcining the copper-containing mixture below 850 °C results in a mixture of CuO, Mn₂O₃ and CuMn₂O₄, and that calcining the magnesium-containing mixture below 850 °C results in MgO, Mn₂O₃, and Mg₂MnO₄. In both cases, using calcination temperatures higher than 950 °C yielded large CuMn₂O₄ and Mg₂MnO₄ whiskers. Molar ratios of starting materials different from those listed yielded the same products but with additional impurity phases, implying that the chosen compositions (CuMn₂O₄, MgMn₂O₄, and Mg₂MnO₄) are the most stable under our reaction conditions.

3.3 CuMn₂O₄, MgMn₂O₄ and Mg₂MnO₄ nanowires

The solid-state reaction of MnO₂ NWs with the rutile-type pyrolusite structure with polycrystalline Cu(OH)₂ was performed, to obtain NWs of CuMn₂O₄ with the spinel-type crystal structure. Shown in Fig. 3.2 are SEM images and indexed XRD patterns from both the MnO₂ NW starting material, and the resulting CuMn₂O₄ NWs. Remarkably, though the reaction of rutile-type NWs to form spinel NWs represents a massive structural change, the anisotropic morphology of the starting material is retained during the transformation to the resulting a wire- or rod-shaped crystals, though admittedly with some degradation of wire quality. Fully-indexed XRD patterns show that a conversion from MnO₂ to CuMn₂O₄ was achieved, with both phase-pure reactant and product, proceeding via the following proposed solid-state reaction:



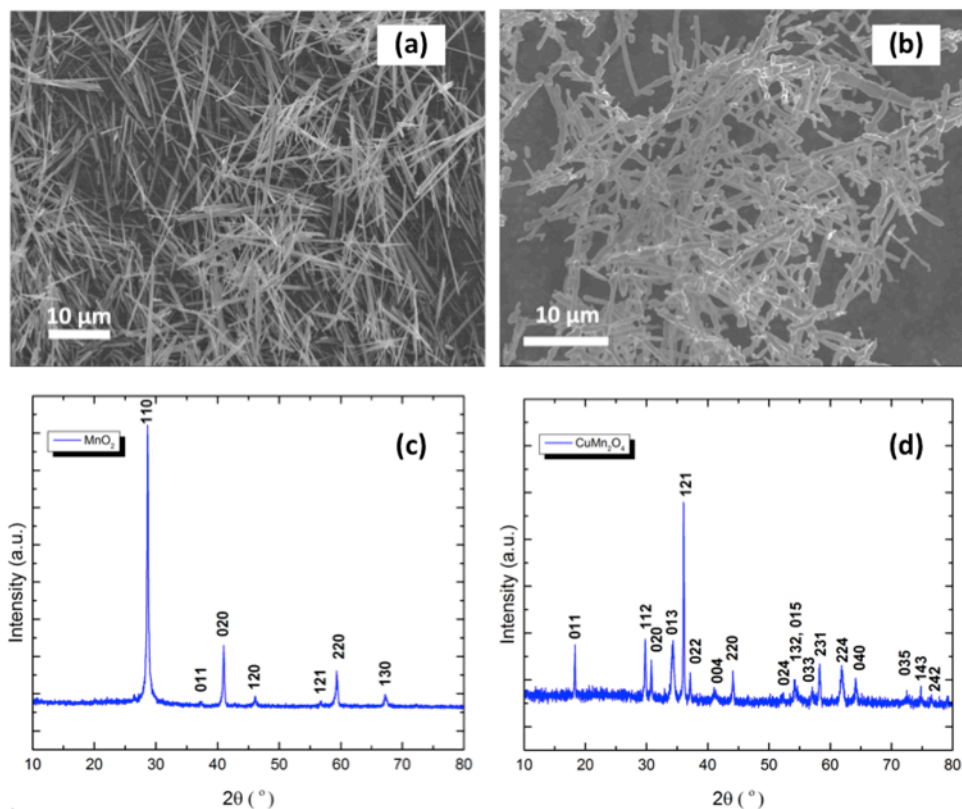


Figure 3.2 Structural characterization of MnO_2 to CuMn_2O_4 conversion. SEM images of (a) MnO_2 and (b) CuMn_2O_4 NWs; and powder XRD patterns of (c) MnO_2 NWs, indexed to the pyrolusite phase (pdf card # 01-071-0071), and (d) CuMn_2O_4 NWs, indexed to CuMn_2O_4 spinel (using the tetragonal space group $I41/amd$, with $a = 5.798 \text{ \AA}$, and $c = 8.791 \text{ \AA}$).

Further characterization of the crystallinity and composition of the CuMn_2O_4 NWs was performed using the TEM to collect higher resolution images, which are shown in Fig. 3.3, with accompanying fast Fourier transform (FFT) and EDS analysis. Inspection of the images and indexing of the FFT confirms the expected spinel structure, and that the wires are single-crystalline; indeed, in every case for which a wire was sufficiently thin to enable high-resolution imaging, the wire was a single crystal. Exact values for the relative concentration of Cu and Mn were challenging to obtain using EDS, since the wires are somewhat too large for a Cliff-Lorimer correction, yet possibly too small for

the standard “ZAF” correction. With this caveat in mind, ZAF-corrected estimates of the Cu and Mn concentrations for the wire shown in Fig. 3.3 are consistent with a 1:2 ratio of Cu:Mn.

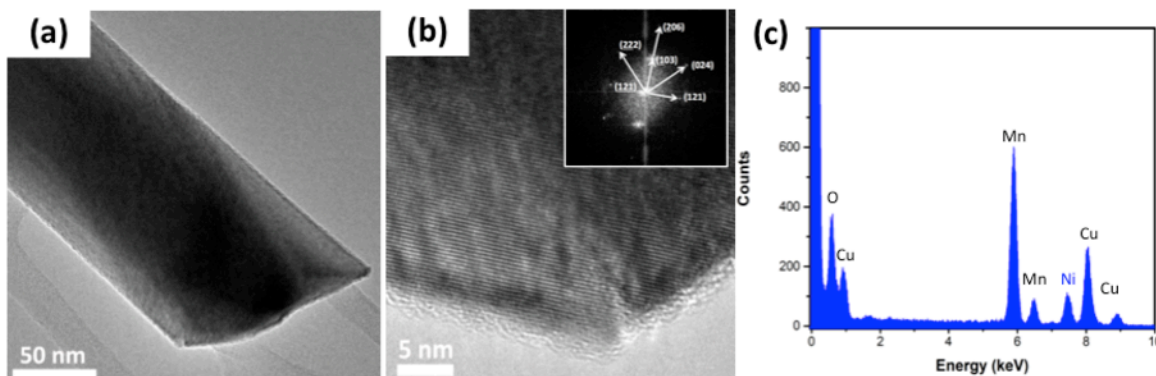


Figure 3.3 Crystallinity and compositional analysis of a CuMn_2O_4 NW (synthesized from MnO_2 precursor). (a) TEM image demonstrating NW facets. (b) High-resolution TEM image with FFT inset, demonstrating single-crystallinity. (c) EDS spectrum showing the presence of Cu, Mn, and O within the wire. Ni peak due to the TEM grid marked in blue.

Our crystal structure model for CuMn_2O_4 was built using CrystalMaker software. By analysis of the calculated spectra, we found that certain relative peak intensities change with degree of inversion (defined by the occupancy of the spinel crystal A- and B-sites), though the peak positions remain the same. These results are shown in Fig. 3.4. The intensities of the (011) and (022) reflections increase, while those of (112) and (020) decrease with an increasing degree of inversion. Though not conclusive, since peak intensities would also depend on crystalline anisotropy resulting from the one-dimensional rod morphology, this allows us to estimate an inversion degree of about 0.9 for our CuMn_2O_4 NR samples where the intensity of (011) lies between that of (112) and (020), while (020) and (022) have about the same intensity, which is consistent with the same four sharp peaks of our experimental XRD pattern. The breadth of the (013) peak makes intensity comparison of this reflection difficult to include in the comparison.

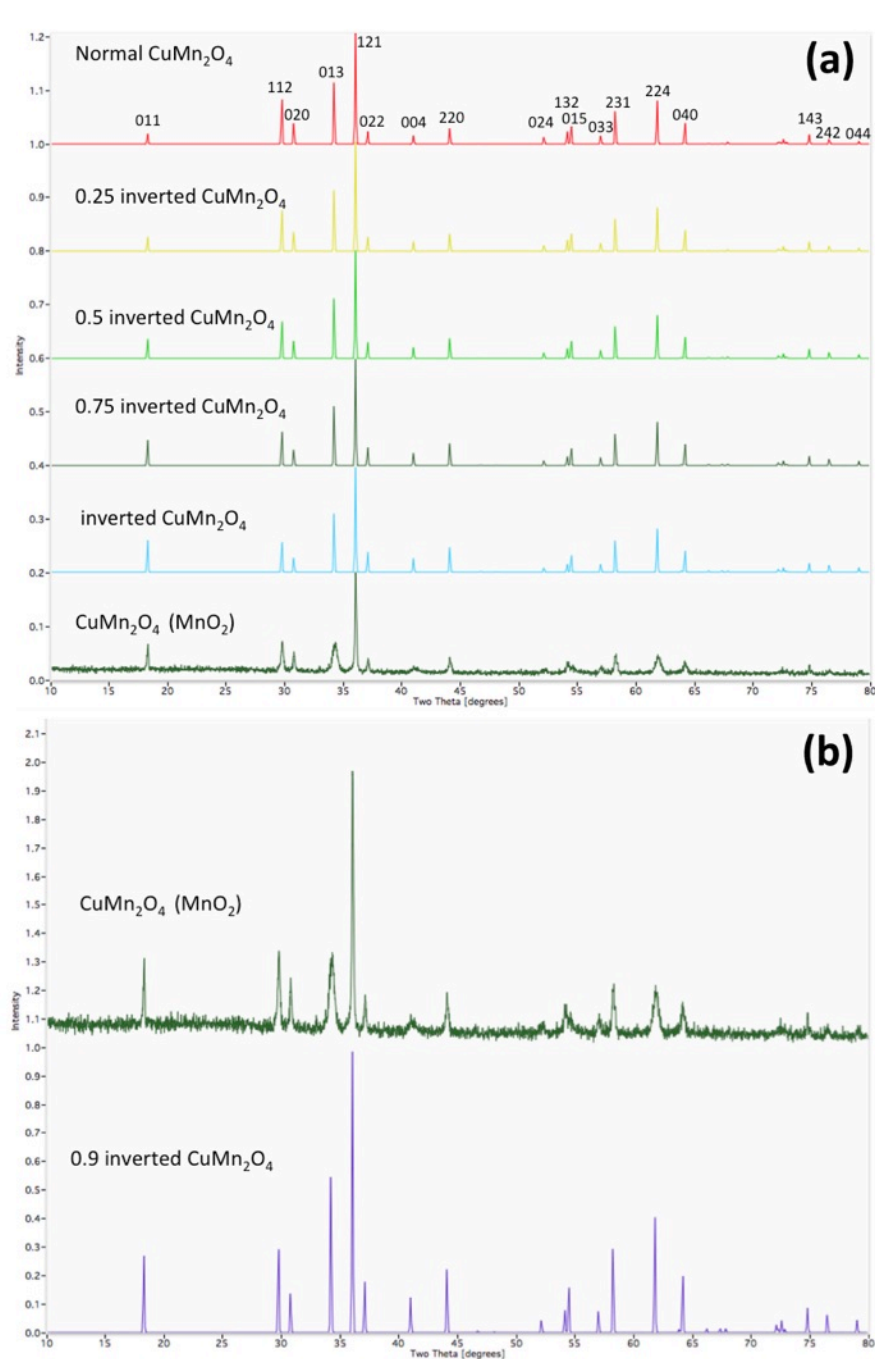


Figure 3.4 (a) Calculated XRD patterns of CuMn_2O_4 with varied inversion degree, compared with our experimental data for the product synthesized from MnO_2 . The intensity of the (011) and (022) reflections increase, while that of (112) and (020) decrease with increasing degree of conversion. (b) Comparison of experimental data to calculated reveals an estimated inversion degree of 0.9, by comparison of the (011), (112), (020), and (022) peaks. The breadth of the (013) peak makes intensity comparison of this reflection difficult to include in the comparison.

Figure 3.5 shows XRD patterns and SEM images of MgMn_2O_4 and Mg_2MnO_4 NWs using an analogous synthetic approach, for which the following solid-state reactions were expected:

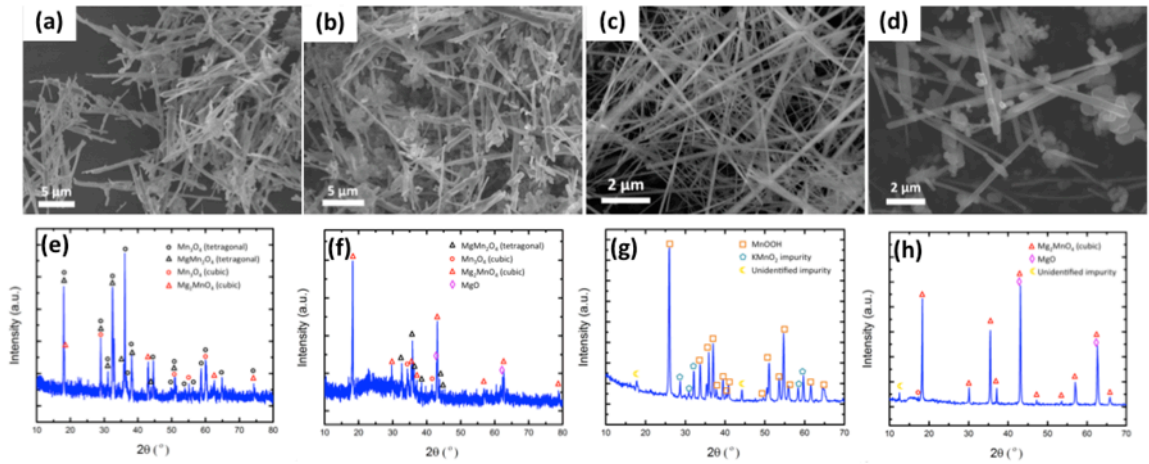
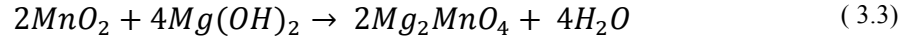
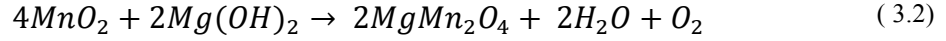
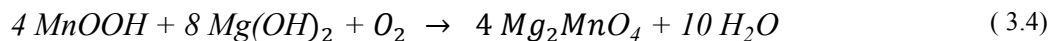


Figure 3.5 Structural characterization of Mg-containing NW syntheses. SEM images of (a) tetragonal spinel NWs with nominal composition MgMn_2O_4 (synthesized from MnO_2 precursor NWs); (b) cubic spinel NWs with nominal composition Mg_2MnO_4 (synthesized from MnO_2 precursor NWs); (c) γ - MnOOH NWs; and (d) cubic spinel Mg_2MnO_4 NWs (synthesized from γ - MnOOH precursor NWs). (e) to (h) Powder XRD patterns from (a) to (d) respectively.

For these reactions, however, XRD reveals that the products are not phase pure, and in each case comprise a dominant phase of the expected structure, with secondary spinel and binary oxide phases. One explanation for this is that the MgMn_2O_4 - Mg_2MnO_4 system forms a limited solid solution, phase separating into cubic spinel on the Mg-rich end, and tetragonal spinel on the Mn-rich end, with mass-conservation achieved by the formation of small amounts of MgO and Mn_3O_4 respectively.

To attempt to access a phase-pure region, we further tried an experiment, using γ -MnOOH NWs as an alternate precursor to replace MnO₂, which for the composition Mg₂MnO₄ produced improved results. SEM images and XRD patterns from both the γ -MnOOH and resulting Mg₂MnO₄ NWs are shown in Fig. 3.5. In this case, though SEM images suggest that our MnOOH starting material is a single material, XRD analysis reveals that it is a mixture of MnOOH and KMnO₂ structure types, and a small (unidentified) impurity phase. (It should be noted that both our SEM and XRD results for γ -MnOOH NWs appear indistinguishable from those of γ -MnOOH NWs used in the published report¹⁹⁰ on which we based our synthesis.) Despite the mixture of structures in the starting material, both types of wires apparently react to form Mg₂MnO₄ NWs in the solid-state reaction step, as indicated by the XRD from this product, for which all but one peak (at 12.5°) can be assigned to cubic Mg₂MnO₄. For the γ -MnOOH starting material, we propose the following solid-state reaction (3.4), and we speculate that the KMnO₂ wires must react similarly, though additionally producing a gas-phase or amorphous potassium-containing side product:



The high-resolution TEM image and FFT of a representative Mg₂MnO₄ NW in Fig. 3.6 shows that similar to the CuMn₂O₄, these wires are single-crystalline, and EDS analysis with a ZAF correction is again consistent with the expected ratio of Mg to Mn. TEM and EDS analysis were additionally performed on a secondary morphology present in our samples, with a small particle (as opposed to NW) morphology (Fig. 3.7). EDS reveals that this phase is very rich in Mg.

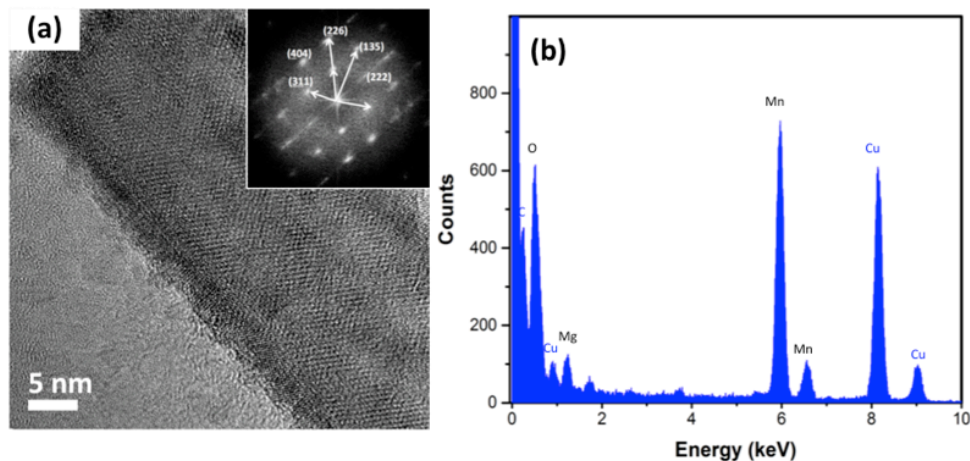


Figure 3.6 Crystallinity and compositional analysis of a Mg_2MnO_4 NW (synthesized from γ - MnOOH precursor). (a) High-resolution TEM image with FFT inset, demonstrating single-crystallinity. (b) EDS spectrum showing the presence of Mg, Mn, and O within the wire (quantitative analysis in supporting information). Cu peak due to the TEM grid marked in blue.

For completeness, we further performed the reaction of $\text{Cu}(\text{OH})_2$ with the γ - MnOOH NW precursor, with similar results in terms of phase-purity, crystallinity, and morphology. In this case, we speculate that the dominant solid-state reaction proceeds as equation 3.5.

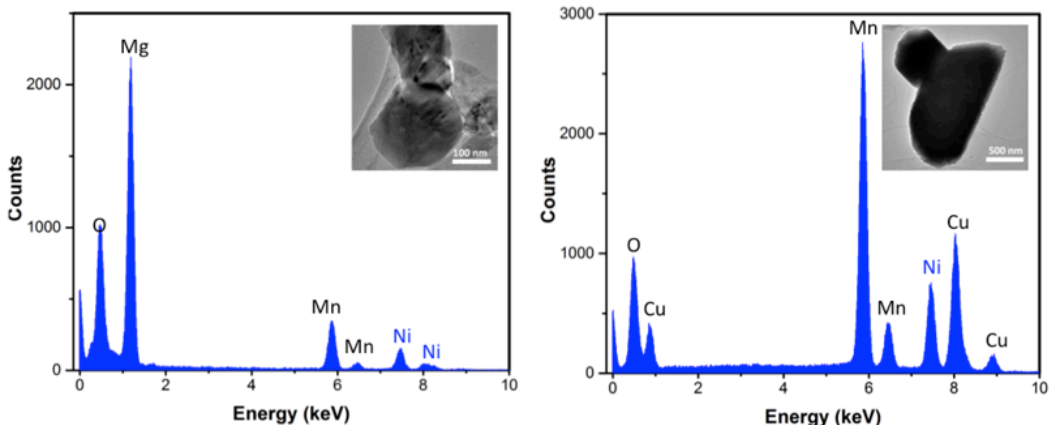
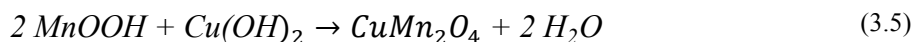


Figure 3.7 EDS spectra and TEM images (inset) from NP impurities present in the ternary oxides synthesized from γ - MnOOH starting material (a) Mg_2MnO_4 synthesis, and (b) CuMn_2O_4 synthesis. Ni peaks from the TEM grid are labeled in blue.

The XRD pattern from CuMn_2O_4 (Fig. 3.8) matches the calculated spectrum (using the tetragonal space group $I4_1/amd$, with $a = 5.798\text{\AA}$, and $c = 8.791\text{\AA}$), except for three minor CuO impurity peaks and one unidentified peak at 12.5° . Given the small powder samples available, and small crystallite size, a Rietveld refinement to further identify these peaks was not possible. CuMn_2O_4 NWs are confirmed to be single-crystalline using high-resolution TEM imaging (Fig. 3.8), and EDS is again consistent with the expected Cu:Mn ratio. The minor (non wire-like) particle phases have also been analyzed by TEM and EDS (Fig. 3.7), but in this case appear to have the same composition as the NW morphologies.

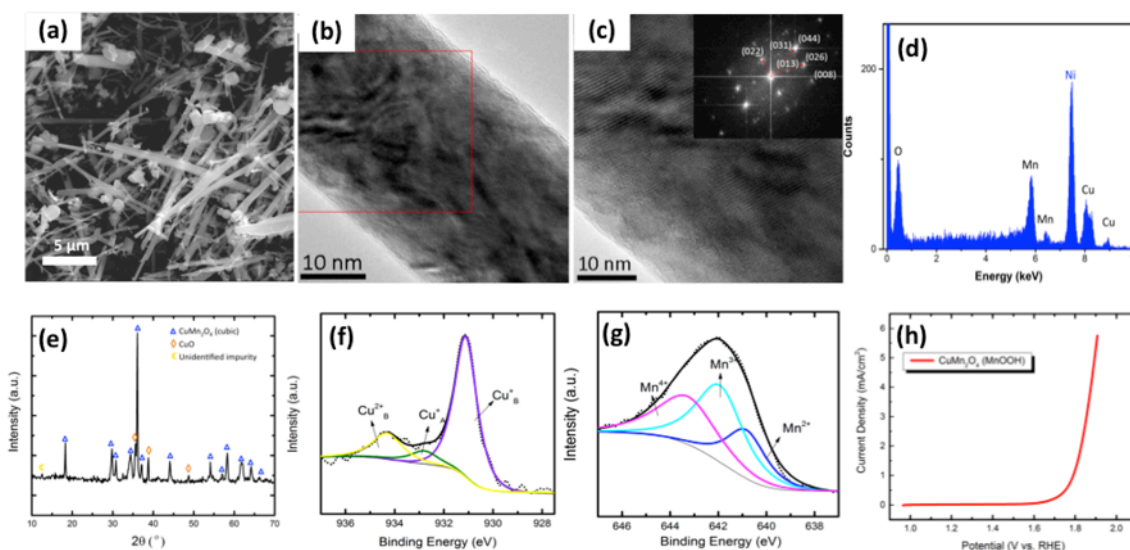


Figure 3.8 (a) SEM image; (b) TEM image; (c) high-resolution TEM image with FFT inset; (d) EDS spectrum; (e) XRD pattern; XPS spectra for the $2p_{3/2}$ region of (f) Cu cations, and (g) Mn cations; and electrocatalytic activity measurement, taken from CuMn_2O_4 synthesized from $\gamma\text{-MnOOH}$ starting material.

3.4 *In situ* TEM study of the reaction mechanism for spinel nanowires

In order to elucidate the structural changes occurring during the calcination process in order to form these spinel NWs, we ran *in situ* TEM heating experiments for the reaction. The diffusion process of metal sources into γ -MnOOH NWs was observed.

Figure 3.9 shows preliminary data taken using this approach, in which γ -MnOOH NWs and bulk $\text{Mg}(\text{OH})_2$ were deposited onto a commercial TEM heating substrate (Protochips Aduro heating E-chip), and the sample temperature was ramped from 300 °C to 870 °C *in situ* while imaging in the TEM. The figure shows frames from the resulting movie, in which the wire on the right of each frame is γ -MnOOH (diameter = 80 nm) and

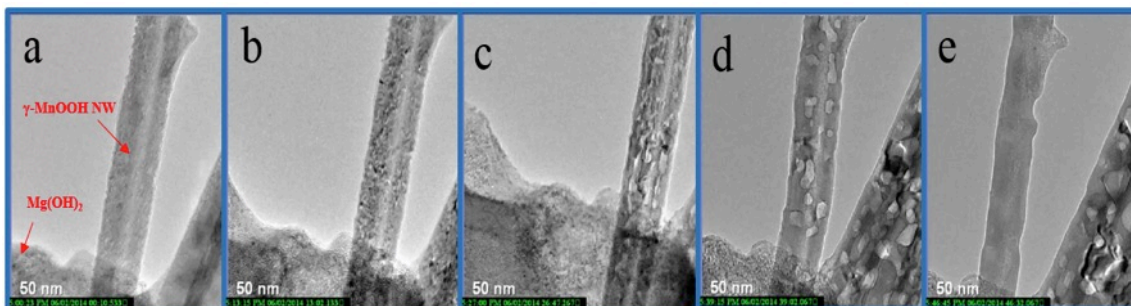


Figure 3.9 Frames from an *in situ* TEM heating video from a γ -MnOOH NW (right) in contact with $\text{Mg}(\text{OH})_2$ crystal (bottom), at (a) 0 min, (b) 13 min, (c) 26 min, (d) 39 min, (e) 46 min; T = 300 to 870 °C

the grain on the bottom left is $\text{Mg}(\text{OH})_2$, both of which were identified by energy dispersive X-ray spectroscopy (EDS). The results of this preliminary data are revealing: as magnesium atoms diffuse into the MnOOH NW, the wire undergoes a transformation from single-crystalline to polycrystalline, and back to single-crystalline *via* the ripening of smaller to larger grains within the polycrystal. From the EDS spectrum of the NW after heating, magnesium is seen to have diffused into the NW (Fig. 3.10).

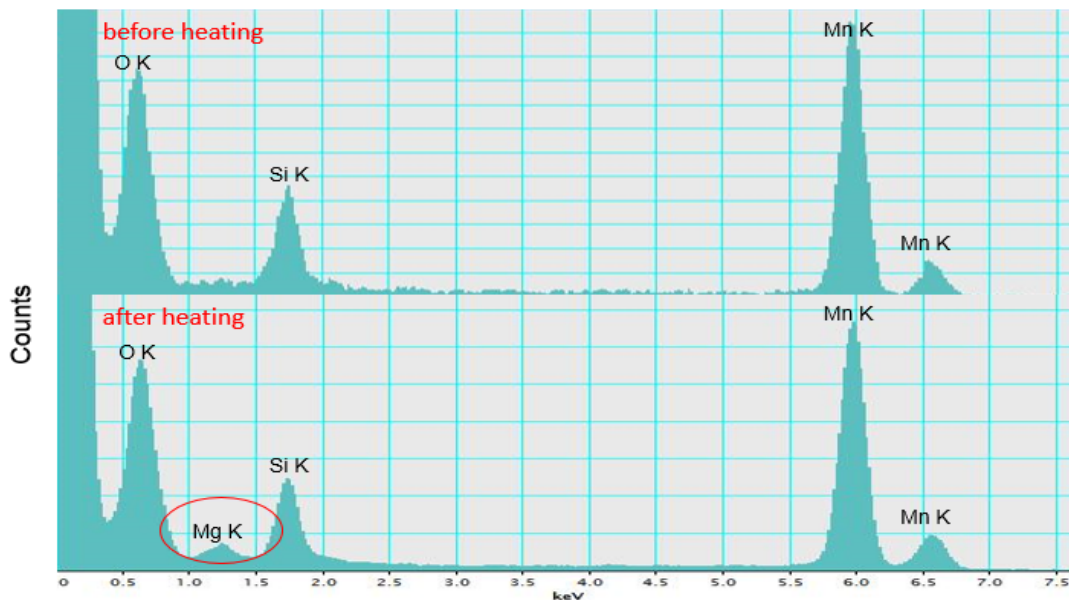


Figure 3.10 EDS spectra taken from the MnOOH NW before and after *in situ* TEM heating

3.5 Catalytic properties towards oxygen evolution reactions

One of the key factors determining the catalytic properties of these NWs is the oxidation states of the cations, which we determined for three samples, using XPS: CuMn_2O_4 using the MnO_2 starting material (as shown in Fig. 3.2 & Fig. 3.3), tetragonal MgMn_2O_4 using the MnO_2 starting material (as in Fig. 3.5), and cubic Mg_2MnO_4 using the γ -MnOOH starting material (as shown in Fig. 3.5 & Fig. 3.6). The binding energy of copper is related to its valence state and its coordination environment. The intense peak at 931.1 eV in the XPS spectra of Cu 2p_{3/2} (Fig. 3.11a) is assigned to Cu^+ on the spinel B site. According to previous XPS studies of CuMn_2O_4 ,^{192–194} the two broad peaks at 932.8 eV and 934.1 eV could be due to Cu^+ on the A site and Cu^{2+} on the B site. Shoemaker et al., however, assigned the peak at 934.75 eV to Cu^{3+} on the B site. From the XPS spectrum, it is evident that significantly more copper cations reside on B sites than A sites, which is consistent with the high inversion degree calculated from CrystalMaker.

Manganese is also known to show mixed oxidation states in manganese-containing spinels. In Fig. 3.11b, peaks at 640.5 eV, 642.1 eV and 644.4 eV can be assigned to Mn^{2+} , Mn^{3+} , and Mn^{4+} , respectively¹⁹⁵ The CuMn_2O_4 NWs are therefore seen to contain Mn^{2+} , Mn^{3+} and Mn^{4+} . In contrast, MgMn_2O_4 and Mg_2MnO_4 NWs contain only Mn^{3+} and Mn^{4+} , heavily dominated by Mn^{3+} in the MgMn_2O_4 sample, and by Mn^{4+} in the Mg_2MnO_4 sample.

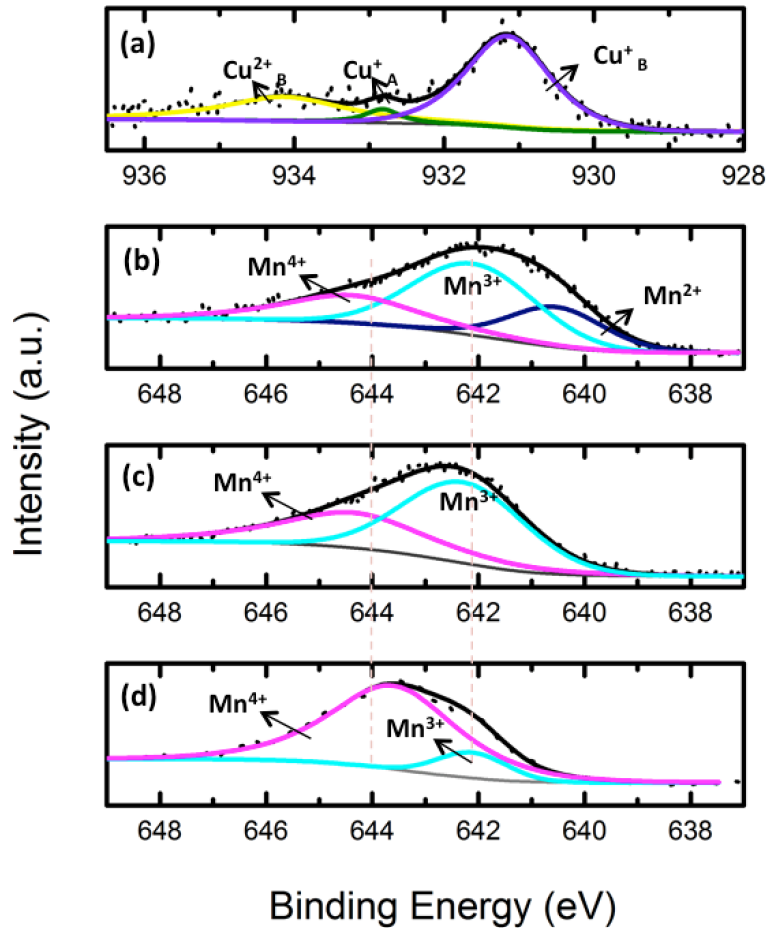


Figure 3.11 XPS spectra for the $2p_{3/2}$ region of (a) Cu cations in CuMn_2O_4 (from MnO_2); (b) Mn cations in CuMn_2O_4 (from MnO_2); (c) Mn cations in MgMn_2O_4 (from MnO_2); and (d) Mn cations in Mg_2MnO_4 (from $\gamma\text{-MnOOH}$).

The catalytic activity of these same three samples towards the oxygen evolution reaction (OER) in equation 3.6, was evaluated from linear sweep voltammetry curves comparing NW samples with pure carbon black (Fig. 3.12).

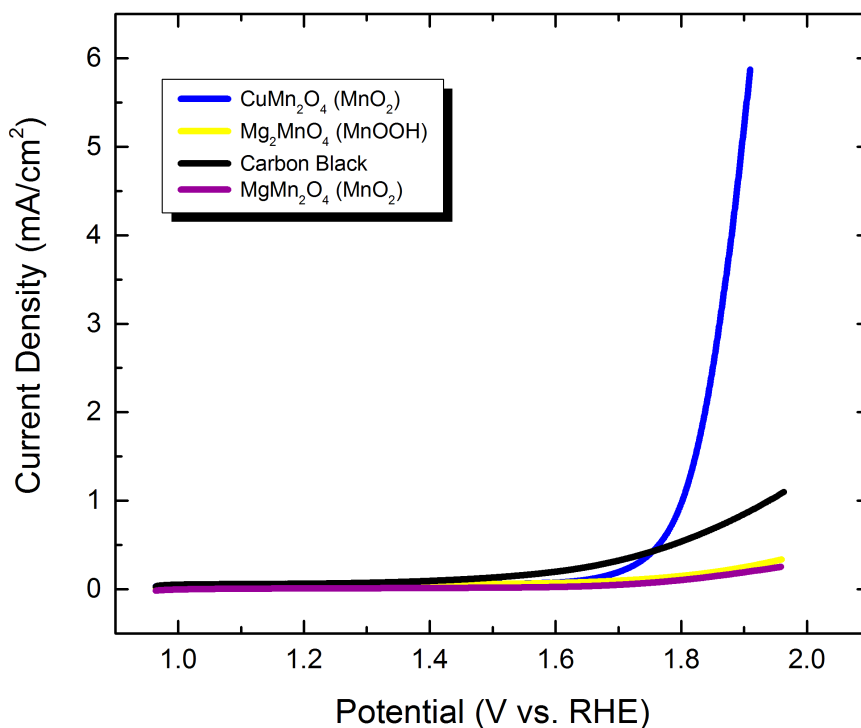
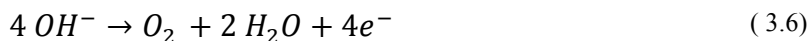


Figure 3.12 Linear sweep voltammetry curves of CuMn₂O₄, Mg₂MnO₄, and MgMn₂O₄, compared with carbon black (iR corrected)

Though all curves were collected with the same mass of sample loaded onto the GC (at 0.143 mg/cm²), the electrocatalytic activity of CuMn₂O₄ NWs toward the OERs was found to be superior to those of magnesium-containing spinels and pure carbon black, with around five times the current density determined at 2.0V.

The onset potential of CuMn_2O_4 was measured to be 1.6 V vs. RHE, which is comparable to the values reported for LaCo_3O_4 and $\text{La}_{0.8}\text{Sr}_{0.2}\text{MnO}_3$ perovskite oxides, and $\text{Co}_x\text{Mn}_{3-x}\text{O}_4$ spinel structures.^{196–198} The OER current of CuMn_2O_4 NWs is significantly larger than those of Mg-containing NWs and carbon black, although the surface roughness of Mg_2MnO_4 is expected to be much lower due to lower expected Brunauer-Emmett-Teller (BET) surface areas, suggesting that optimizing the surface area of the CuMn_2O_4 NW sample would lead to a highly catalytic sample. Despite of large differences in BET surface areas between two catalysts, calibration of the LSV data with respect to BET surface areas was not attempted, since it is difficult to estimate the area available for catalysis, and the surface area is in any case dominated by that of carbon black. We speculate that the multiple oxidation states of Cu and Mn induce the strong adsorption of OH^- reactants on catalyst surfaces, and also provide enough density of states to support fast electron transfer.

Oxidation state variance of the metals in Mg_2MnO_4 and CuMn_2O_4 are expected to affect the catalytic properties. Studies have shown that the key factor determining catalytic activity towards the OER for cubic Mg_2MnO_4 is the large amount of tetravalent manganese ions on the octahedral sites.¹⁷⁶ Interestingly, for tetragonal CuMn_2O_4 , however, the material is more catalytically-active but has fewer tetravalent manganese ions on the octahedral sites. Reported characterization of this material suggests that half of the tetravalent manganese ions reside on the octahedral sites, along with one third of the trivalent manganese ions and a small number of Cu^{2+} and Cu^{3+} cations.¹⁸¹ It is possible that having both multivalent copper as well as manganese in CuMn_2O_4 might provide a synergy which promotes catalytic activity.

3.6 Conclusion

We described a new route to make single crystalline Mg_2MnO_4 NWs and CuMn_2O_4 NWs by the simple solid-state reaction of MnO_2 and $\gamma\text{-MnOOH}$ NWs with metal hydroxide metal sources in such a way that the metal diffuses into the NW, undergoing a rutile to spinel crystal structure transformation, while preserving an anisotropic wire or rod-like morphology. Linear sweep voltammetric results revealed the electrocatalytic activity of Cu_2MnO_4 NWs for the oxygen evolution reaction in alkaline solution. We believe this synthetic route may be extended as a general way to synthesize many manganese-containing spinel NWs, as well as other ternary oxides.

Chapter 4 Solid-liquid-vapor synthesis of negative metal oxide nanowire arrays

Parts of this chapter are taken from “Solid-Liquid-Vapor Synthesis of Negative Metal Oxide NW Arrays”, *Chemistry of Materials*, 2016, 28(24), 8924-8929.⁶⁶

4.1 Introduction

Single-crystalline NW syntheses comprise a vast body of research, in no small part because such an approach can produce materials with well-defined, crystalline surfaces which are identical in structure and function from wire to wire.^{15,54,199,200} In large (bulk) quantities, the large surface-to-volume ratios of nanomaterials translates to very large, functional, surface areas. For anisotropic materials such as NWs, growing them in large arrays has created further interest, since in this architecture the surfaces presented may be aligned, and very closely spaced, making them attractive for incorporation into working devices.^{74,201–203} In the usual case an array of NWs is fabricated by growing from within a (usually amorphous) template (which is subsequently dissolved),^{204–207} or from a patterned array of metal catalyst particles.^{208,209} The resulting wires are therefore freestanding, with no precise relationship to, or interaction with, one another, though there are some reports of alignment achieved via lattice-matching with the underlying substrate.^{33,210–212}

An alternate approach to creating a similar array of surfaces is instead to embed an array of *negative* nanowires (NNWs), or pores, within a single-crystalline matrix. Several attempts have been made to create such materials with high aspect ratio pores, or NNWs, including dry etching methods, metal assisted chemical etching, and solid-liquid-vapor etching. Dry etching methods such as reactive ion etching are used widely, both industrially and for research.^{213–216} In this approach, ions are produced from a reactive

gas and accelerated with high energy, to collide and react (both physically and chemically) with a substrate. Though effective this leads to limited pore depths and correspondingly low aspect ratios, sidewall roughness induced by the ions, and can be expensive. In metal-assisted chemical etching, noble metals are used to induce local oxidation and reduction reactions under open circuit, in solution. This technique is mainly used for Si,^{217–222} and it remains a challenge to apply to other materials.^{223,224}

One particularly elegant approach is to utilize metal catalyst droplets *via* the SLV mechanism.^{225–231} This approach employs a variation on the reverse of a typical VLS NW growth mechanism, in which a metal catalyst droplet catalyzes the growth of a single-

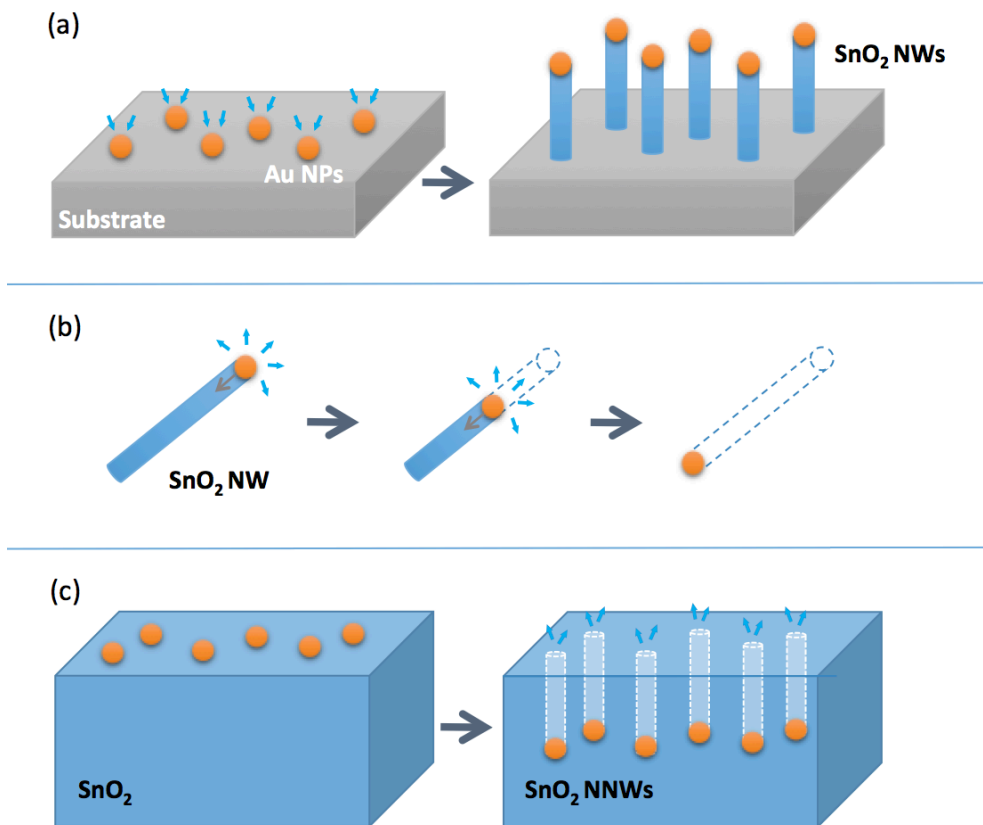


Figure 4.1 Cartoon depicting (a) VLS growth of SnO₂ NWs, (b) SLV dissolution of a single SnO₂ NW, and (c) SLV creation of negative SnO₂ NNWs

crystalline NW from vapor-phase reactants (Fig. 4.1a). In an SLV dissolution process, diffusion from the solid into the metal suppresses the liquidus of the resulting solid solution, inducing the particle to melt. Continued diffusion into the now alloyed droplet continues, until supersaturation occurs and the reactant vapor leaves the particle at the liquid-vapor interface. If the driving forces, such as low pressure and/or a reactive chemical atmosphere, for the process are maintained, the metal droplet can be induced to etch the crystal. Schematics of this process are shown in Fig. 4.1b for the SLV dissolution of an entire NW, and in Fig. 4.1c for the SLV creation of NNW arrays as discussed in this dissertation.

In addition to the typical advantages associated with VLS NW growth, such as control over size of the NNW (*via* controlling the size of the catalyst), control of the cross-sectional shape of the NNW (by minimizing the surface energies of the bounding facets), and great versatility in the choice of material, NNW arrays created using the SLV mechanism have several other key advantages. Like freestanding NWs, NNWs could be expected to grow along unique etch directions (so as to minimize the surface energy associated with the bounding facets) and can therefore be expected to have well-defined crystallographic relationships to one another, for example by aligning in parallel. Additionally, unlike an array of freestanding NWs (other than perhaps those grown epitaxially from a single-crystalline substrate), a NNW array will not comprise many free-standing objects, but will instead be contained within a single object, rendering it facile to move and manipulate. Further, because it is contained within a single crystal, it is possible to imagine that interaction between the NNWs might be manipulated by an external stimulus such as applied pressures and lattice strains.

Previous work to synthesize NNW arrays has focused on Group IV, III-V, and II-VI semiconductors, and mostly utilized reactive gaseous environments. Wagner first reported SLV etching of negative whiskers in 1968,²²⁵ etching holes into single-crystalline Si and Ge substrates with Au and Ni catalyst particles respectively, within a reactive gas environment. In this case reaction of Si or Ge with hydrogen chloride gas at the liquid-vapor interface was seen to drive the etching process. Over a decade after this first report, Givargizov et al. grew negative whiskers of ZnS via the SLV mechanism in hydrogen flow,²²⁶ and CdS,²²⁷ GaAs and GaP²²⁸ were found to etch in a similar way. Much more recently, InP NWs have been found to etch using Au catalyst particles in HCl flow,²²⁹ Ge NWs were created by etching in 2,3-butanedione,²³⁰ and Nikoobakht et al. found Au catalysts would etch across the (001) surface of InP, InAs, and GaP in water vapor.²³¹

Reactive gas atmospheres can present their own challenges, however, as these gases are often corrosive, or highly diffusive, and the diffusion of reactive gases and etchant ions into the substrate material may leave behind unwanted byproducts.^{232,233} Etching in vacuum (in a non-reactive atmosphere) is a way to overcome this problem. To date, the only report of SLV etching to produce NNW arrays performed in a vacuum environment was published by Kim and Stach,²³⁴ who etched GaN self-catalytically, with Ga droplets formed by the decomposition of the surface layer of the substrate, and the only known report of SLV etching by a *dissimilar* catalyst material in a similar environment, involves our own work in which an entire NW of SnO₂ was dissolved by the metal catalyst particle at its tip (see Fig. 4.1b), during *in situ* heating in the transmission electron microscope (TEM).²³⁵ On the basis of our work and the previous reports, we speculate that a similar

vacuum SLV etching approach could be applied to a wide range of crystalline substrates to produce NNW arrays; indeed, any catalyst-substrate material combination previously known to produce NWs *via* the VLS mechanism should be a viable candidate for SLV etching. Here we show controlled SLV etching in a chemical-free environment using a dissimilar catalyst for the first time, on two different oxides, SnO₂ and ZnO, and demonstrate control over the size, shape, and etch direction of NNW production. We additionally have performed SLV etching on Si substrates revealing an orientation relationship between the resulting etch-pits.

4.2 Methods

Epitaxial (111) SnO₂ thin-films of around 350 nm were grown on (0001) sapphire substrates via pulsed laser deposition (PLD),²³⁶ using a ceramic target, and a KrF excimer laser ($\lambda = 248$ nm) with a fluence of 1.6 J/cm². The films were deposited at 350°C in an oxygen atmosphere of 50 mTorr, with a laser repetition rate of 10 Hz. We used commercial sapphire (Al₂O₃) (0001) substrates bought from University Wafer.

To produce metal catalyst droplets, 4 nm (for Si) or 8 nm (for the oxides) of Au was deposited on each substrate using e-beam evaporation, and the composite was annealed at 500°C for 30 mins, to produce NPs. Alternately 50 nm gold colloid solution (BBI Solutions) was drop-cast onto the surface.

To perform etching, the NP/substrate composite was placed in a closed end tube furnace, connected to a turbo pump and heated under the conditions given in the text at a pressure of 10⁻⁵-10⁻⁶ Torr.

A dual beam focused ion beam (FIB) scanning electron microscope (SEM) was used to view the cross section of the substrates. For this, a FEI Helios Nanolab 660 system was

operated with immersion mode in either secondary electron (SE) or backscattered electron (BSE) mode. A gas injection system (GIS) was used to deposit carbon or platinum to protect the surface of the sample; a gallium liquid metal ion source (LMIS) was used for milling, and an Oxford EDX detector was used for elemental analysis. The area for imaging was first covered in carbon or platinum, and the ion beam was used to drill into the sample, exposing an inner cross-section of the sample for imaging.

4.3 Temperature and time effect on SLV etching for SnO₂ thin films

The crystallography controlling VLS NW growth should in large part be transferable to SLV NNW array synthesis. In order to investigate the extent to which the crystallographic arguments are similar, we attempted the SLV etching process on epitaxial thin-films of SnO₂. 350 nm-thick films of SnO₂ were grown using pulsed laser deposition (PLD), and showed phase-purity and good crystallinity, with a (111)

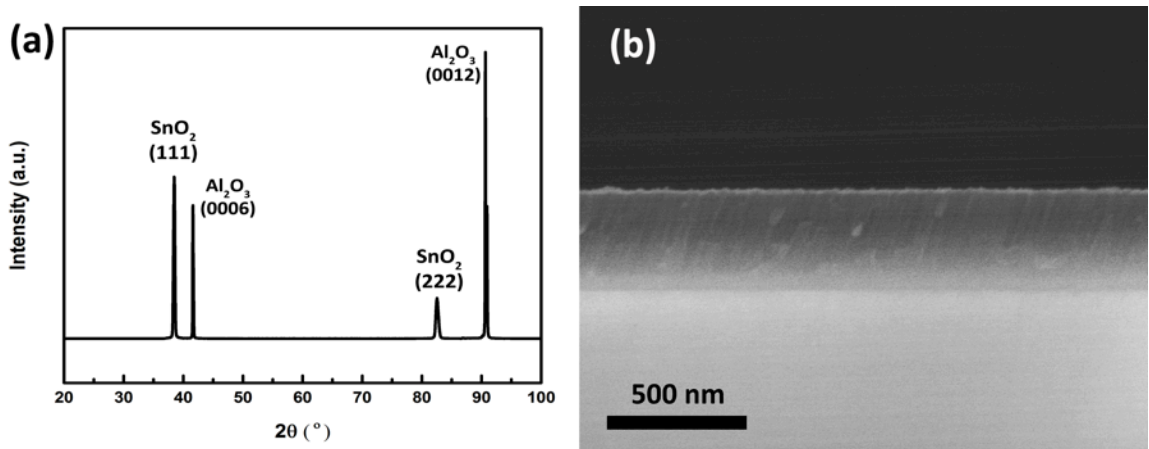


Figure 4.2 Characterization of SnO₂ on Al₂O₃ thin film. (a) XRD pattern, and (b) SEM image of the substrate cross-section.

orientation due to matching with the underlying (0001) sapphire substrate (Fig. 4.2). Au NPs were deposited on the SnO₂ surface using electron-beam evaporation of a thin gold

layer, and annealing. In these initial studies we first optimized the time and temperature dependence of SLV etching. In VLS NW growth, NW length is positively correlated with growth time, since the saturation of gold catalyst particle with reactants and subsequent nucleation of the NW occurs rapidly, after which the NW length increases at a roughly constant rate.^{237,238} Using parameters identified previously from SLV etching of an individual NW,²³⁵ we annealed the SnO₂ film at 900°C and low pressure for several different times, as shown in Fig 4.3. Before annealing the Au particles are easily

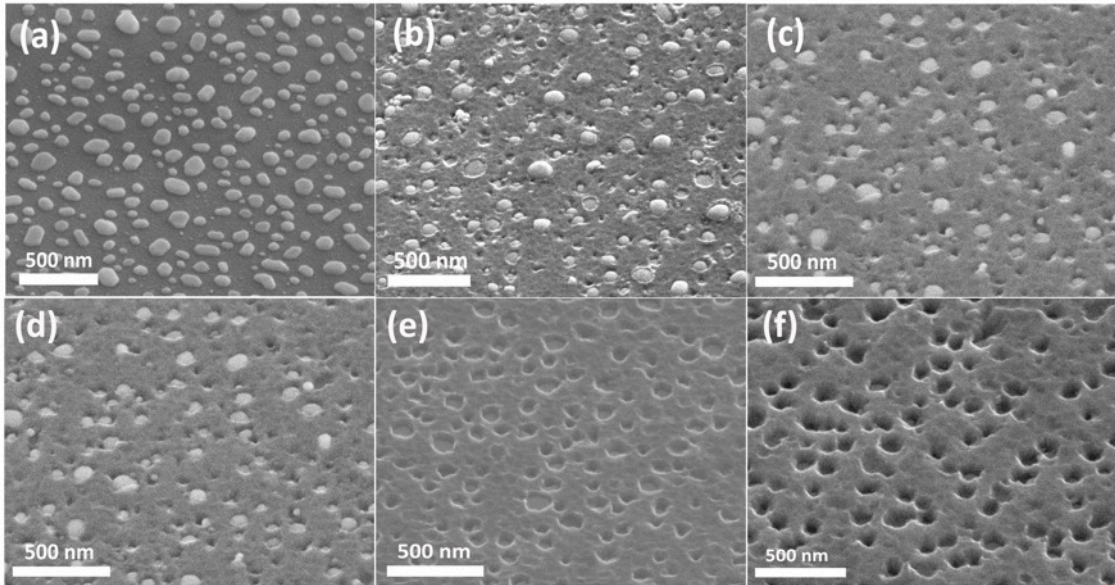


Figure 4.3 SEM images of the SLV process. (a-c) Gold NPs on SnO₂ epitaxial thin-film after annealing under high vacuum at 900°C for (a) 0 min; (b) 30 min; and (c) 60 min. (d-f); Gold NPs on a SnO₂ epitaxial thin-film after annealing under high vacuum for 60 min at (d) 900°C; (e) 925°C; and (f) 950° C

observed on the surface of the SnO₂ film, and all of them have initiated the etching process after an annealing period of 60 min, though the particles are still visible (Fig 4.3c). At the 30 min midpoint roughly half of the NPs appear to have initiated the etching process, suggesting that unlike the VLS growth process, saturation of the gold catalyst and “nucleation” of the NNW does not occur rapidly during SLV etching, most likely

because the reactant is now contained within a stable crystalline lattice, as opposed to the vapor phase as is the case for VLS.

Another key factor in determining etching depth is the annealing temperature. As shown in Fig. 4.3 (d-f), the length of the SnO₂ NNWs increases with elevated annealing temperature. When annealing the Au NP-decorated SnO₂ substrate for 1 h in vacuum, the depth of NNW was seen to increase on changing the temperature from 900°C to 950°C. Cross-sectional images of an SnO₂ substrate etched at 950 ° C for 60 min were collected using a dual-beam focused ion beam (FIB) instrument to mill a cross-section and image and show the residual gold catalyst at the base of the NNW (Fig. 4.4). The identity of the gold was confirmed using energy dispersive X-ray spectroscopy (EDS). Studies to measure the nucleation rate, and rate of NNW growth, as a function of Au NP size, temperature, time, and dispersion, are ongoing and expected to enable quantitative modeling of the SLV-etching kinetics.

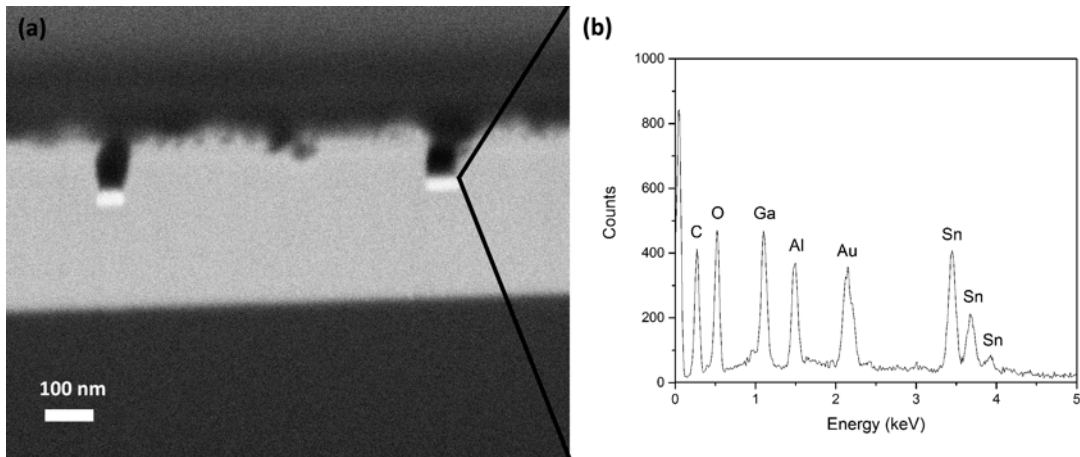


Figure 4.4 (a) Cross-section SEM image of SnO₂ thin film etched with 8 nm thickness of Au at 950 °C for 1 h and (b) EDS spectrum for the bright region at the bottom of the hole, showing the presence of gold.

4.4 Effect of catalyst particle size and crystal orientation on SLV etching for ZnO

One simple advantage of VLS NW growth is the ability to dictate NW diameter using the size of the metal catalyst particle. A similar dependence is observed in our experiments, as evidenced by comparison of Au NP size and dispersion before SLV etching, and NNW size and dispersion afterwards (**Figure 4.5**). An analysis of the images shown in **Figure 4.5**, in which 50 nm Au particles were deposited on the (0001) surface of a single-crystalline ZnO substrate, and annealed at 1000 °C for 60 min, shows approximately a one-to-one correlation of the number of NPs before etching to NNWs post-etching (3.52 NPs per square micron to 3.45 NNWs per square micron respectively), and an average NNW diameter of 78 ± 9.6 nm in comparison to 50 nm for the pre-etching NPs. Interestingly, though the dispersion of NNWs, is close to the initial NPs, the average NNW diameter is seen to be consistently larger than that of the initial NP, suggesting that once melted, the NP wets the surface to form a flattened droplet with wider diameter than the initial solid metal. In the limit of a spherical NP flattening to form a completely flat disc, we calculate that the height of such a disc (assuming constant volume) would be 14 nm. An interesting observation in support of the flat disc scenario is the presence of a flat disc-like piece of gold at the base of each NNW in the cross-section images shown in **Figure 4.4**. Though potentially complex, there is clearly a close dependence of NNW diameter on the initial Au droplet size, and it is the opposite to that seen for VLS growth of NWs, for which surface tension of the Au droplet leads to NW diameters smaller than the droplet diameters.

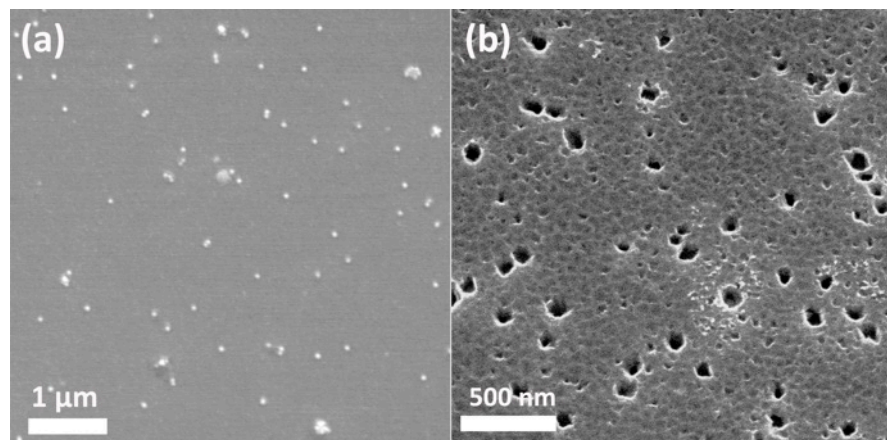


Figure 4.5 SEM images of (1000) ZnO substrate deposited with 50 nm gold NPs. (a) Before and (b) after etching at 1000 °C for 1h in vacuum.

VLS grown NWs are well-known to possess unique wire directions, resulting from preferential growth directions which maximize the low energy surfaces. To investigate the possible translation of this effect to NNW growth, we performed SLV-etching of single-crystalline ZnO substrates with the wurtzite structure and three different orientations. ZnO was chosen because when grown in NW form it is consistently seen to grow along the [0001] direction, and with a distinctive hexagonal cross section. Shown in Fig. 4.6 are the results of SLV-etching of ZnO substrates with orientations (0001), ($1\bar{1}00$) and ($11\bar{2}0$), at 1000°C for 30 min. Similarly to NW growth, the NNWs are seen to etch along the [0001] direction in all three cases, leading to tracks perpendicular to the substrate surface for (0001)-oriented ZnO (Fig 4.6a-d), and parallel to the surface for ($1\bar{1}00$) and ($11\bar{2}0$) (Fig 4.6f-i, k-n). Evidence that the NNW etch-direction is [0001] for ($1\bar{1}00$)- and ($11\bar{2}0$)-oriented ZnO is provided not only by the etch tracks parallel to the surface, but additionally by the orientation of the hexagonal cross-sections of the NNWs with respect to the surface (Fig 4.6h, i). These results are similar to those seen for Au NP etching of (001)-oriented InP in the

presence of water vapor as the reactive gas, for which anisotropic etching occurs preferentially along the (111)-normal.²³¹ Pore formation with preferred low energy facets has also been observed previously in crystals for which a simple sublimation process has occurred, with no metal catalyst particles present.²³⁹ The sublimation process will therefore present an upper temperature bound for performing SLV-etching, since maintaining catalyst control of the mechanism will require us to avoid a high-temperature sublimation regime.²⁴⁰

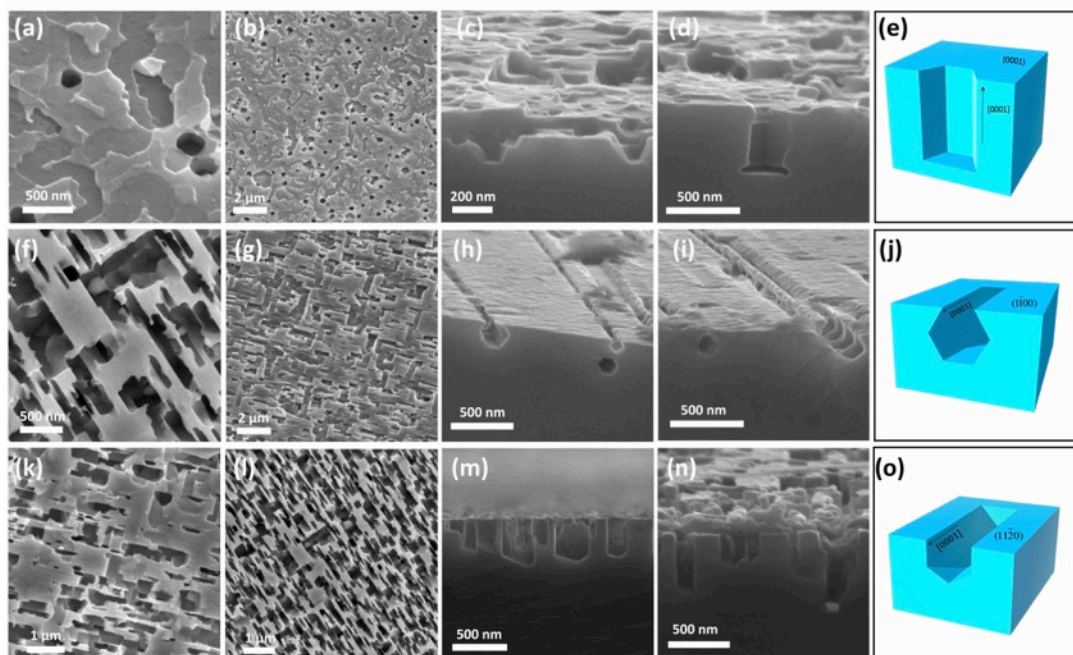


Figure 4.6 SEM images of gold NP etched ZnO substrates with different orientations upon annealing at 1000°C for 30 min. (a-d), (f-i) and (k-n) are SEM images of (0001), (1 $\bar{1}$ 00) and (11 $\bar{2}$ 0) ZnO substrates respectively, with 2 top view images and 2 cross-section view images each case. (e), (j) and (o) show cross-sectional diagrams of the expected shape of a [0001]-oriented NNW.

Further evidence of the SLV-etching mechanism is provided by performing the process at lower temperatures. Fig 4.7 shows images of (0001) ZnO substrates after etching at 800, 900 and 1000°C for 1h. In all cases, there is evidence of etch tracks parallel to the surface, suggesting that mobile gold droplets initially diffuse across the

(0001) surface, etching trenches *via* the SLV process, but only in the case of annealing at 1000°C, the NPs acquire sufficient activation energy to etch perpendicular to the surface in the preferred [0001] direction. This set of observations provides evidence that, though there is a thermodynamic driving force for etching in the [0001] direction, the particles must first overcome an activation energy. We speculate that this may be an adhesive force between the gold droplet and the walls of the NNW, similar to the adhesion observed between gold droplet and TEM substrate in our previous studies of individual NW dissolution *via* SLV.²³⁵

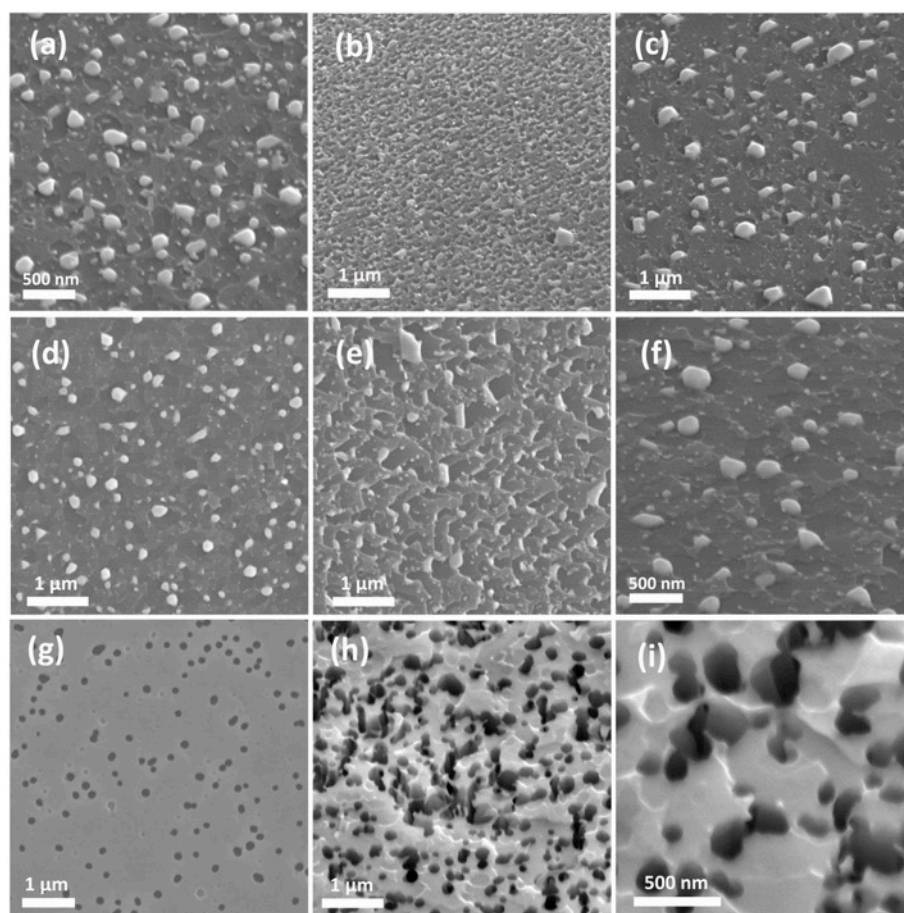


Figure 4.7 SEM images of gold NP etched (0001) ZnO substrates upon annealing at 800 °C (a-c), 900 °C (d-f) and 1000 °C (g-i) for 1 hour in high vacuum

4.5 SLV etching on silicon substrate

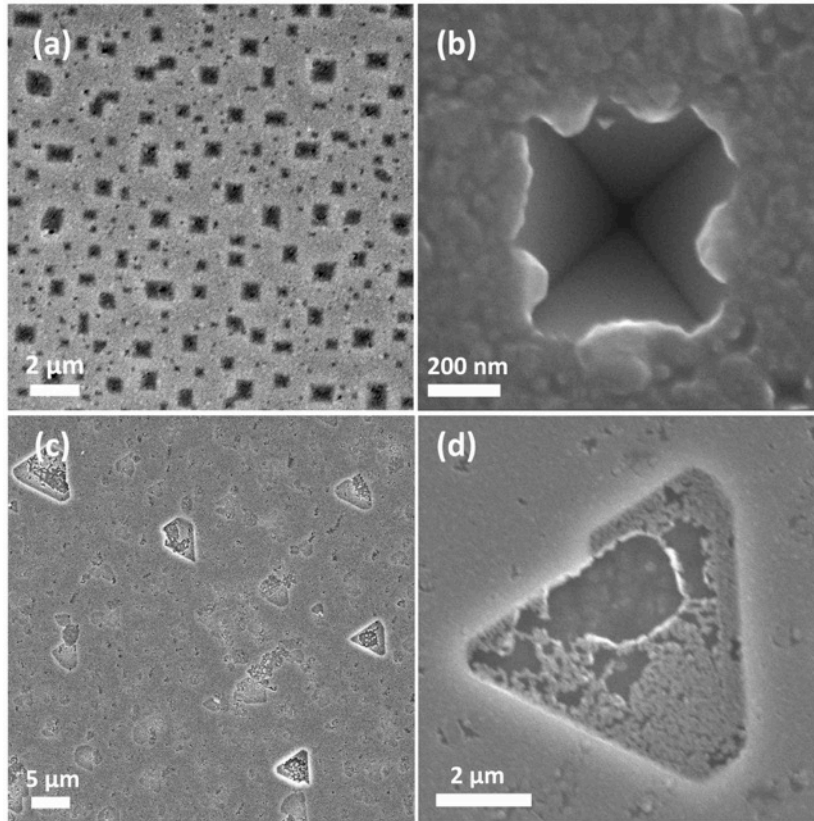


Figure 4.8 SEM images of gold NP etched (001) Si substrate (a, b) and (111) Si substrate (c, d).

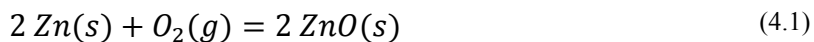
SLV-etching was also attempted on elemental Si substrates and did not produce NNWs for these samples but, rather, etchpits similar to those reported by other groups.^{241–243} Etching at 950°C for 2 hours to produce low surface energy facets is also observed in (100)- and (111)-oriented Si substrates (Fig. 4.8), with the crystallographically equivalent {111} facets resulting in differently shaped pits. For the case of (100) Si, square-pyramidal pits were formed, bounded by four {111} type planes. For the (111)-oriented Si, a wide and shallow, triangular prismatic pit was formed, producing a large (111) facet at the base, with six {111}-type sidewalls. In our experiments, due to the single-crystalline nature of the underlying Si substrate, all Si pits

show a clear orientation relationship to one another, aligning parallel. We include this data not as an example of NNW formation but as an example of the orientation relationship resulting from etching a single-crystalline substrate. The much larger footprint of these pits with respect to the original NPs suggests that the gold wets the Si surface and agglomerates prior to etching.

In addition to the evidence presented above, rough calculations of the expected melting and decomposition temperatures of the substrates used reveal temperatures which are several hundred degrees higher than the temperatures used in our experiments, consistent with our assumption that, in each of the examples presented, the gold catalyst droplets were responsible for etching. The calculations of the melting points of ZnO, SnO₂ and Si at low pressure are provided as below.

The sublimation temperatures of the substrates involved are much greater than 900 °C; at ambient pressure, ZnO decomposes at 1975 °C, and SnO₂ and Si melt at 1630 °C and 1414 °C respectively.

1) ZnO. To consider the possibility that low pressure may promote the decomposition of ZnO at lower temperature, we considered the thermodynamics of the reaction:



From the Ellingham Diagram,²⁴⁴ the absolute Gibbs free energy ($|\Delta G^\circ|$) of this reaction was found to decrease with increasing temperature, agreeing with negative enthalpy gain, since the entropy change of this reaction must be negative, and ΔG° can be generally expressed as a linear relationship with T:

$$\Delta G^\circ = \Delta H^\circ - T\Delta S^\circ \quad (4.2)$$

Below the boiling point of Zn metal, only O₂ will contribute to the reaction constant of the decomposition giving the following relationship between ΔG° and the oxygen partial pressure p_{O2} at equilibrium:

$$\Delta G^\circ = -RT\ln(Q) = RT\ln(p_{O_2}) \quad (4.3)$$

Taking ΔH° = -850 kJ/mol and ΔS° = -0.378 kJ/mol.K from the Ellingham Diagram²⁴⁴ and p_{O2} = 5 × 10⁻⁶ Torr (a typical pressure for our etching experiment), the decomposition temperature of ZnO was found to be 1317 °C, which is well above the temperature of our experiments. Thus the estimation suggests that decomposition of ZnO should not dominate under our experimental conditions.

2) SnO₂. For the decomposition reaction SnO₂ → Sn + O₂, with reference to the Ellingham Diagram, we get:

$$\Delta G = -575 + 0.2T = RT\ln(p_{O_2}) \quad (\text{unit: kJ/mol}) \quad (4.4)$$

which gives T = 2876 K (2603 °C) at ambient pressure, and T = 1612 K (1339 °C) at low pressure (p_{O2} = 5 × 10⁻⁶ Torr = 6.59 × 10⁻⁹ bar).

According to literature, SnO₂ may start to sublime at 1800~1900 °C,²⁴⁵ though the melting point has also been predicted to be ~2500 °C.²⁴⁶ One possibility is that the decomposition of SnO₂ may accompany this sublimation, consistent with the report of Lamoreaux et al.²⁴⁷ who show that the decomposition of SnO₂ is more complex than that of ZnO.

3) Si. In contrast to the metal oxides, the melting point of silicon increases as pressure decreases, since similar to water, the molar volume of liquid silicon is less than that of crystalline silicon. From the experimentally-determined pressure-temperature diagram for bulk Si, T_m decreases as P increases in agreement with a model prediction.²⁴⁸

$$T_m(P) = T_{m0} \sqrt{(1 + A)}. \quad (4.5)$$

where A is a pressure-related negative term (dominated by $V_l < V_s$). In full, this can be expressed:

$$T_m(P) = T_{m0} \sqrt{1 + \{2(V_l - V_s)P + [V_s \kappa_s - V_l(\gamma/f)\kappa_l]P^2\}/H_{m0}} \quad (4.6)$$

Taking pressure = 5×10^{-6} Torr and $A = -1.5 \times 10^{-9}$, reduced pressure results in a small increase of T_m to 1420 °C as compared with 1414 °C at ambient conditions.

4.6 Conclusion

We report for the first time the SLV-based synthesis of NNW arrays in which the catalyst metal was not a product of the underlying substrate, and no reactive atmosphere was employed. Optimization of the process on epitaxial SnO₂ thin films shows that NNW growth rate can be controlled by reaction temperature, and reaction time and NP catalyst size control the length and diameter of the NNW, respectively. For single-crystalline ZnO and Si substrates, a unique etch direction was observed, leading to specific NNW or etch-pit orientations, with respect to both the substrate surface and to one another. Given the simplicity of our SLV approach for the synthesis of NNW arrays, it should be widely generalizable to any catalyst-substrate material combination previously known to produce NWs via the VLS mechanism. As such, this synthetic approach has the potential to be utilized as a method to produce high densities of highly specific and well-defined crystal facets, from a very wide range of materials, contained within a single, easy to manipulate substrate.

Chapter 5 Understanding hollow metal oxide nanomaterial formation with *in situ* TEM

5.1 Introduction

Hollow nanomaterials have been studied for decades, in large part for their potential applications such as catalysis,^{249–251} energy storage,^{252–254} sensors² and drug delivery²⁵⁵, which rely on their unique characteristics⁵ such as the high surface area to provide more active sites, the thin shell to reduce mass transport path, and the hollow interior to relieve structural strain with improved stability. Hollow iron oxide nanomaterials are of particular interest, due to their high theoretical lithium ion storage capacity, low toxicity, and cost.²⁵⁶ For example, iron oxide nanotubes have shown to perform well as anode materials in lithium ion batteries,^{257,258} supercapacitors,²⁵⁹ and catalysts,^{260,261} and also display interesting magnetic properties.^{261,262}

In order to fully exploit the potential of these hollow iron oxide nanomaterials, it is critical to understand and control the crystal structure (for the many different iron oxide phases) and morphology. The phase transformation of β -FeOOH to α -Fe₂O₃ has been observed in air;^{263–266} however, β -FeOOH undergoes transformation to the spinel phase (either γ -Fe₂O₃ or Fe₃O₄) in high vacuum.^{264,267–269} Both processes have been shown to result in porous or hollow morphologies.^{265,267,269} Chen et al.²⁶⁵ observed voids in the center of a β -FeOOH NR upon annealing in air, during the transformation to the α -Fe₂O₃ phase. Single pores have been observed by Gonzalez-Calbet et al.²⁶⁷ in γ -Fe₂O₃, resulting from the decomposition of β -FeOOH in vacuum. In all of these cases, while the final structure and composition are dictated by synthetic conditions, the porous or hollow morphologies appear to depend solely on the identity of the starting material.

Hollow nanomaterial syntheses can be categorized generally, into template and template-free syntheses. The templates include hard templates such as polystyrene,²⁷⁰ silica,²⁷¹ carbon,²⁷² and metal oxide²⁷³, and soft templates including gas bubbles²⁷⁴ and emulsion micelles²⁷⁵. Templated synthesis of hollow nanomaterials not only yields poorly crystalline materials, however, may also be expensive and time-consuming due to the complexity of the process.^{276,277} In this regard, template-free synthesis is superior and comes with advantages such as simple synthetic procedures, high reproducibility, low production costs, and the potential of scaling up the synthesis for large quantity production. To this end, much work has been done to understand the various hollowing mechanisms. Galvanic erosion, an electrochemical process with an ion metal been reduced by another metal with lower reduction potential, is used to produce metal hollow structure. Sun et al.⁴⁴ synthesized Au nanoboxes by using Ag nanocubes as a sacrificial template, upon which Au was deposited via reaction of Ag with H₂AuCl₄, before the dissolution of the Ag to form a hollow Au cube shape; Pd nanocubes were synthesized by Xiong et al.²⁷⁸ using a similar approach. The Kirkendall effect is another elegant method to prepare hollow metal oxide nanostructure, in which the difference in diffusion rates between two components in a diffusion couple leads to voids formed in the fast diffusion side. For example, Yin et al.²⁷⁹ reacted Co nanocrystals with O₂, S, and Se to form hollow oxide or chalcogenides nanostructure, and the synthesis of hollow ZnAl₂O₄ NW by reaction of ZnO-Al₂O₃ core-shell NWs, in which ZnO and Al₂O₃ are the fast and slow diffusers respectively, opened up a new window to the synthesis of various binary and ternary metal oxide hollow nanomaterials,²⁸⁰ One particularly intriguing approach, known as inside-out Oswald ripening, utilizes a solution phase synthesis by deposition of

dissolved small crystals on the surface of larger crystals in an asymmetric hollowing manner, and has been utilized to synthesize various hollow species such as SnO_2 ,²⁸¹ Fe_3O_4 ,²³ and TiO_2 ⁴ hollow spheres.

One effective way to explore hollowing mechanisms is reaction time-dependent studies, complemented with transmission electron microscopy (TEM) characterization.^{4,23-25} Nevertheless, the information obtainable from *ex situ* experiments are limited, and leads to the necessity of deducing mechanistic steps from “before” and “after” data points. To this end, *in situ* experiments have been exploited with great effect for some known hollowing mechanisms, in particular, the Kirkendall effect. Herman et al. demonstrated the oleylamine-assisted transformation of iron-iron oxide core-shell NPs to iron oxide hollow NPs induced by electron-beam irradiation in TEM.²⁸² Niu et al. reported an *in situ* study using liquid cell TEM of the Kirkendall effect, in which it induces bismuth oxide hollow NP formation.²⁸³ Recently, Yu et al. investigated the kinetics of Ag NW hollowing via the Kirkendall effect, using transmission X-ray microscopy²⁸⁴.

In this chapter we describe the decomposition of single-crystalline β -FeOOH NRs, to form hollow single crystalline NRs, for which we expect the α - Fe_2O_3 and γ - Fe_2O_3 phases to form in the air and high vacuum respectively, in which, the final hollow *morphology* is dictated by starting material rather than particular phase transformation. Using *in situ* imaging in the TEM we have revealed a new hollowing mechanism which we term “surface-confined” Ostwald Ripening, which is reminiscent but distinctive and different from the reported inside-out Ostwald ripening. Four hollow iron oxide species were synthesized via this route, α - Fe_2O_3 , γ - Fe_2O_3 , Fe_3O_4 and FeO.

5.2 Syntheses of β -FeOOH nanorods and nanowires

β -FeOOH NRs and NWs were synthesized through a hydrothermal method based on literature.³⁷ In a typical synthesis, 4 mmol $\text{FeCl}_3 \cdot 6\text{H}_2\text{O}$ and cetyltrimethylammonium bromide (CTAB, 0.9 g) were dissolved in 36 ml deionized water and stirred for 15 min. The mixed solution was then transferred to 45 mL Teflon-lined stainless steel autoclave, sealed and maintained at 80 °C or 120 °C for 12 h. After the system was allowed to cool down to room temperature, the product was collected and washed with distilled water and ethanol, and dried at 60 °C overnight. To make hollow α - Fe_2O_3 nanocapsules, β -FeOOH NRs were annealed in air at 500-700 °C for 3 hours.

5.3 Formation of hollow iron oxide nanorod in *in situ* TEM

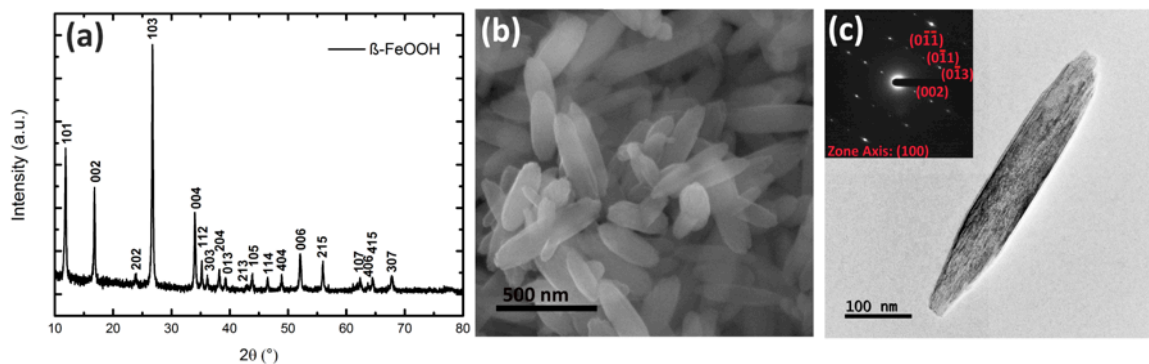


Figure 5.1 Structural characterization for β -FeOOH NRs. Powder X-ray diffraction pattern (a), SEM image (b) and TEM image with FFT inset (c) of β -FeOOH NRs.

NRs and NWs for this study were synthesized via a hydrothermal method. The phase purity, morphology and single-crystallinity for the as-grown β -FeOOH NRs were identified by XRD, SEM and TEM as shown in Fig. 5.1. On annealing the β -FeOOH NRs in air at 500-700 °C, a transformation into hollow single-crystalline α - Fe_2O_3 capsules is revealed (Fig. 5.2). High-resolution TEM images confirm the single-crystallinity of these nano-capsules.

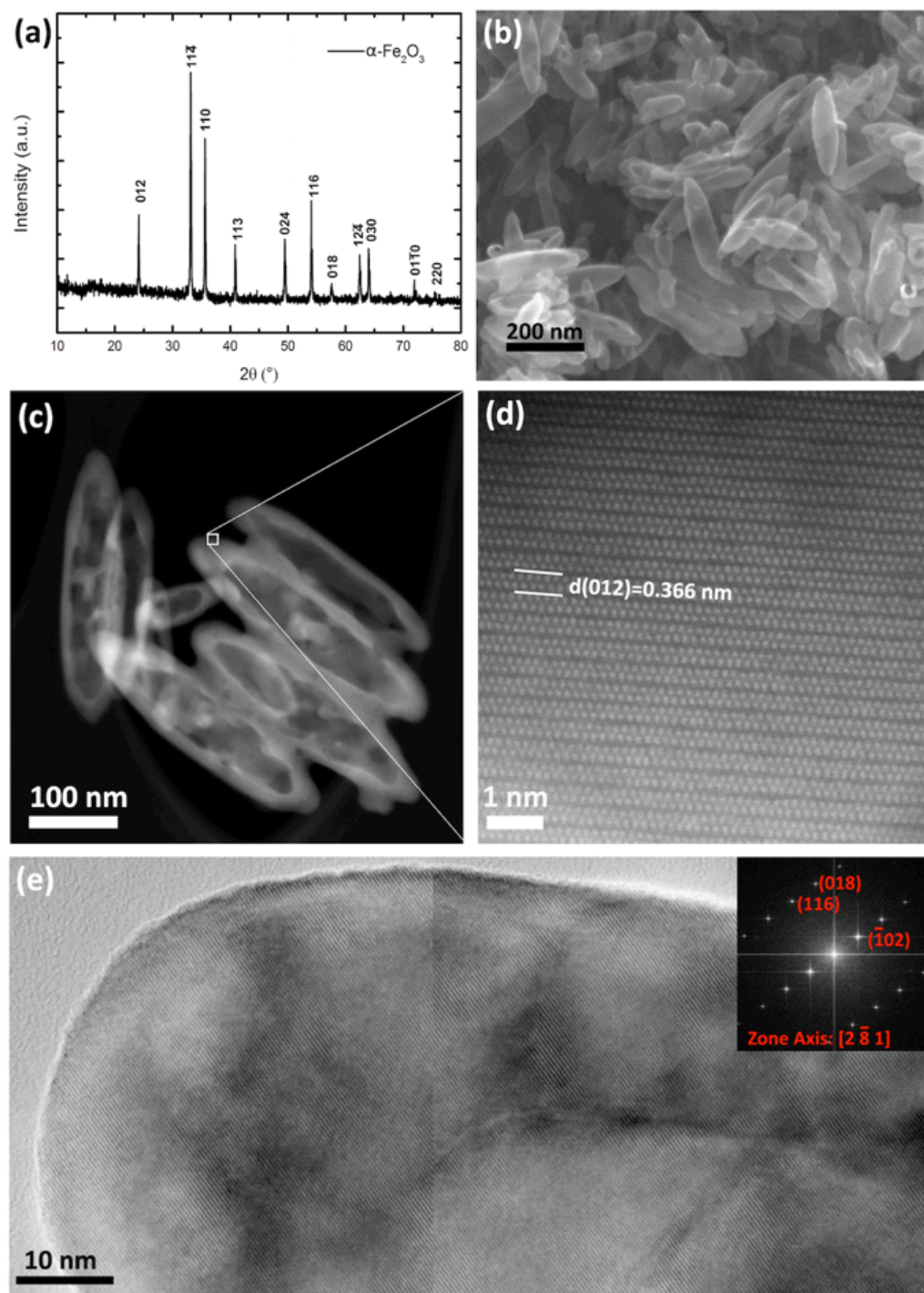


Figure 5.2 Structural characterization of hollow α -Fe₂O₃ NRs. Powder X-ray diffraction pattern (a), SEM image (b), HAADF STEM image (c-e) and TEM images (e) of hollow α -Fe₂O₃ NRs demonstrating their phase purity and single crystallinity. HRTEM image composed of two sub images with FFT inset (e), showing the single crystallinity of the high curvature end.

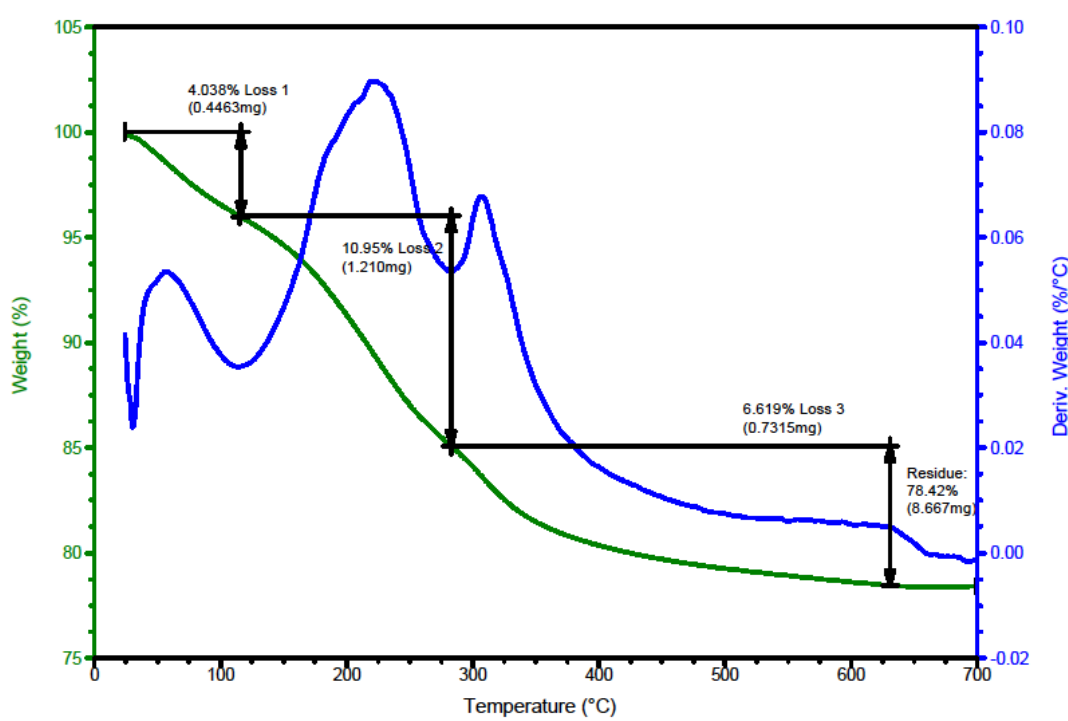


Figure 5.3 Thermalgravimetric analysis of β -FeOOH NRs heated from 25 °C to 700 °C in air. The curve in green is the weight of sample, the blue curve is the derivative weight.

As a complementary probe of the transformations occurring in air, thermalgravimetric analysis (TGA) was acquired (Fig. 5.3), and shows three weight losses. The loss below 100 °C is assigned to the desorption of surface water, while the loss at around 300 °C signifies decomposition of β -FeOOH to α -Fe₂O₃. These results are consistent with *in situ* XRD (Fig. 5.4) which we acquired in the low vacuum: here we see no structural change below 100°C, above which the β -FeOOH phase contracts, and eventually disappears, to be replaced by α -Fe₂O₃ at around 300 °C. An additional weight loss in the TGA at around 230 °C is very likely from water residing in the tunnel structure of β -FeOOH, and occurs concurrently with the contraction of the crystal structure and collapse of the tunnel. Interestingly this occurs during an intermediate region of the *in situ* XRD for which the structure appears to almost entirely lose its crystallinity.

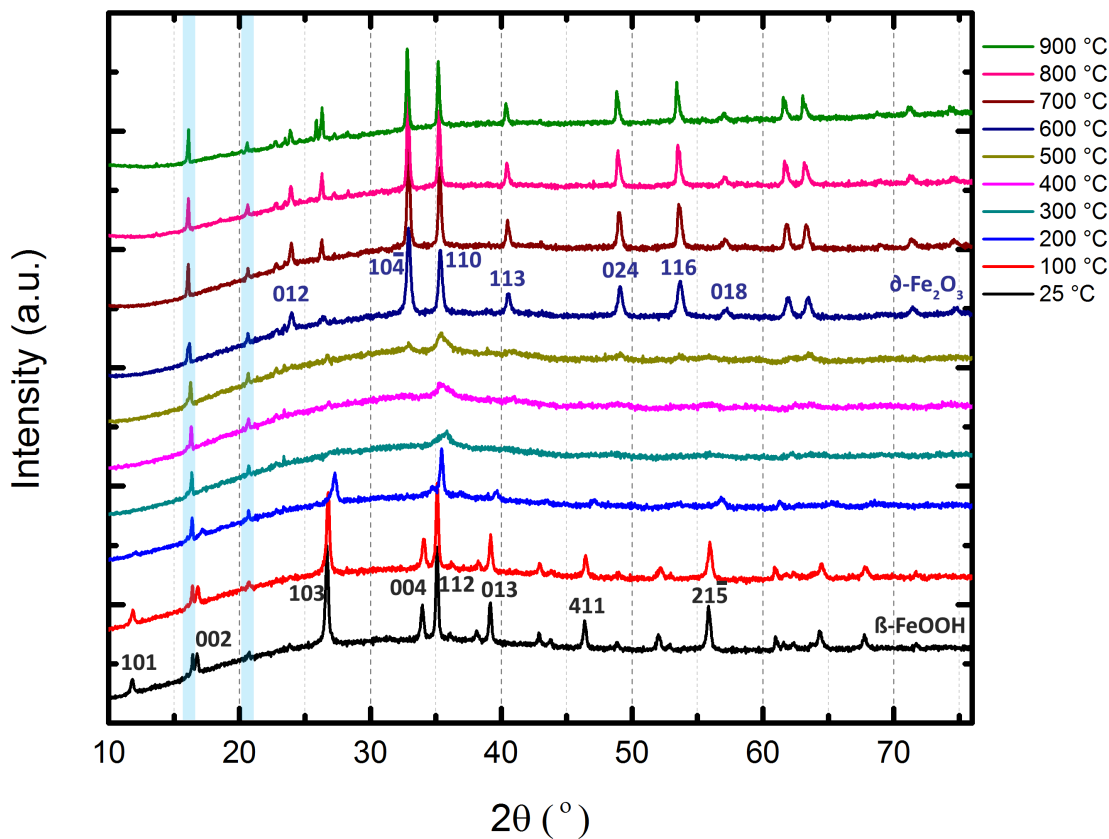


Figure 5.4 *In situ* XRD of β -FeOOH NRs during annealing from 25 °C to 900 °C in low vacuum. The two masked peaks are from the sample stage.

We conducted *in situ* TEM experiments to observe the solid NR to hollow nanocapsule evolution process. The β -FeOOH NR was heated up from room temperature to 700 °C in the TEM with a ramping rate of 1 °C/s. Figure 5.5 shows the frames every 3 min from the video recorded for a β -FeOOH NR during heating. The NR initially has no change until around 300 °C, at which point it starts to look polycrystalline; at 350 °C a shell starts to form, inside of which small crystals grow and agglomerate to form larger ones. As the temperature is ramped, the larger crystals are seemed to continuously wet the inner surface of the shell continuously increasing its thickness until every small

crystallite is consumed. Significantly, the outer diameter of the NR does not change throughout the hollowing process.

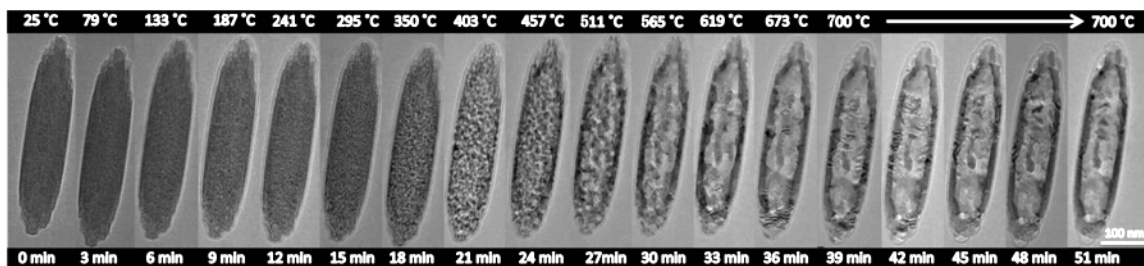


Figure 5.5 TEM images of an FeOOH NR as it is heated in situ. The rod is seen to become porous, and then hollow.

To further identify the species during phase transformation, we collected selected area diffraction patterns (SAED) for another NR. The β -FeOOH NR was annealed for 10 min at 100 °C intervals, and quenched for SAED pattern collection, as shown in Fig. 5.6. At 300 °C the NR starts to transform into β -Fe₂O₃. From 400 to 600 °C, the NR is identified as spinel phase with two possible species: γ -Fe₂O₃ and Fe₃O₄. It is very interesting that there are two sets of patterns for spinel phases in a temperature range of 400-600 °C. The β -Fe₂O₃ phase is typically believed to undergo transformation to α -Fe₂O₃ at this temperature range,²⁸⁵⁻²⁸⁹ with one notable exception reported for β -Fe₂O₃, in which hollow NPs transform to γ -Fe₂O₃ at 400°C. In this unusual case, the authors hypothesize that the extremely elevated surface area of the hollow morphology of β -Fe₂O₃ NPs plays a critical role in determining the transformation mechanism.²⁹⁰ Similarly, in our case, the porous structure of β -Fe₂O₃ phase dehydrated from β -FeOOH might foster the transition to γ -Fe₂O₃ phase instead of α -Fe₂O₃. At 700 °C we found FeO and some spinel phase coexisted. The rod then collapsed and couldn't be identified from diffraction pattern at 800 °C.

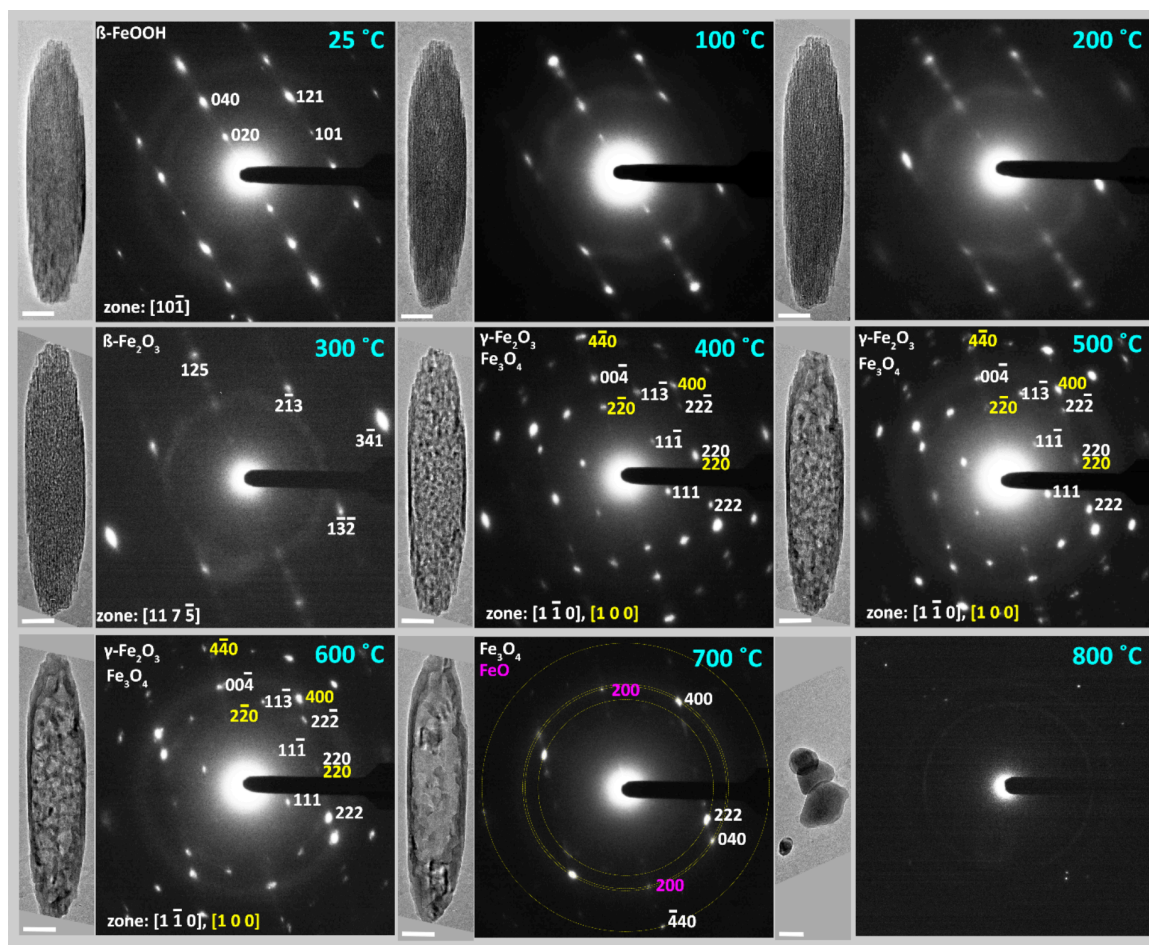


Figure 5.6 TEM images and corresponding selected area diffraction patterns of a NR during *in situ* heating. The rod undergoes phase transformations from β -FeOOH to β -Fe₂O₃, to γ -Fe₂O₃/Fe₃O₄, to Fe₃O₄/FeO, while becoming hollow, and maintaining single-crystallinity.

The crystal structure of the two spinel species: γ -Fe₂O₃, and Fe₃O₄, are almost indistinguishable from their diffraction signatures, given that γ -Fe₂O₃ is simply a defective form of the Fe₃O₄ structure.²⁹¹ Thus, electron energy loss spectra (EELS) were collected for another NR under the same heating profile to monitor the evolution of iron oxidation state during phase transformation, as shown in Fig. 5.7.

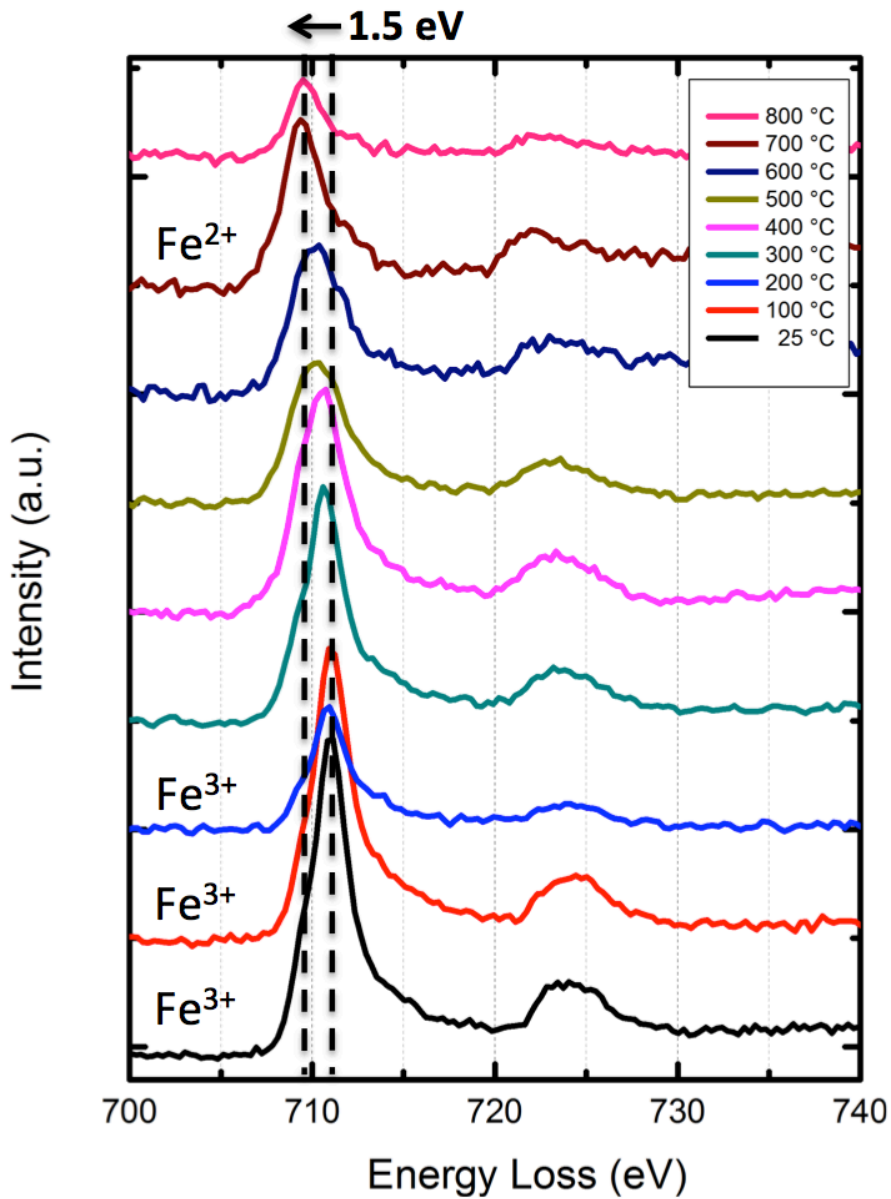


Figure 5.7 Iron $L_{2,3}$ -edge of the electron energy loss spectrum of a NR during heating from 25 °C to 800 °C. It shows a red-shift on reduction of the iron.

The iron edge at around 711 eV started to shift to left till 700 °C, with a total 1.5 eV shift, indicating a Fe^{3+} to Fe^{2+} or Fe^0 transition.^{292,293} The disappearance of the oxygen edge at around 531 eV above 700 °C (Fig. 5.8) confirms the reduction of Fe^{3+} ,²⁹⁴ while the retention of the 540 eV edge indicates the presence of oxygen and in an increasingly

Fe²⁺-rich environment. The continuous reduction of Fe³⁺ to Fe²⁺ over the 300 - 700°C temperature range is suggestive of a γ -Fe₂O₃ to Fe₃O₄ phase transformation.

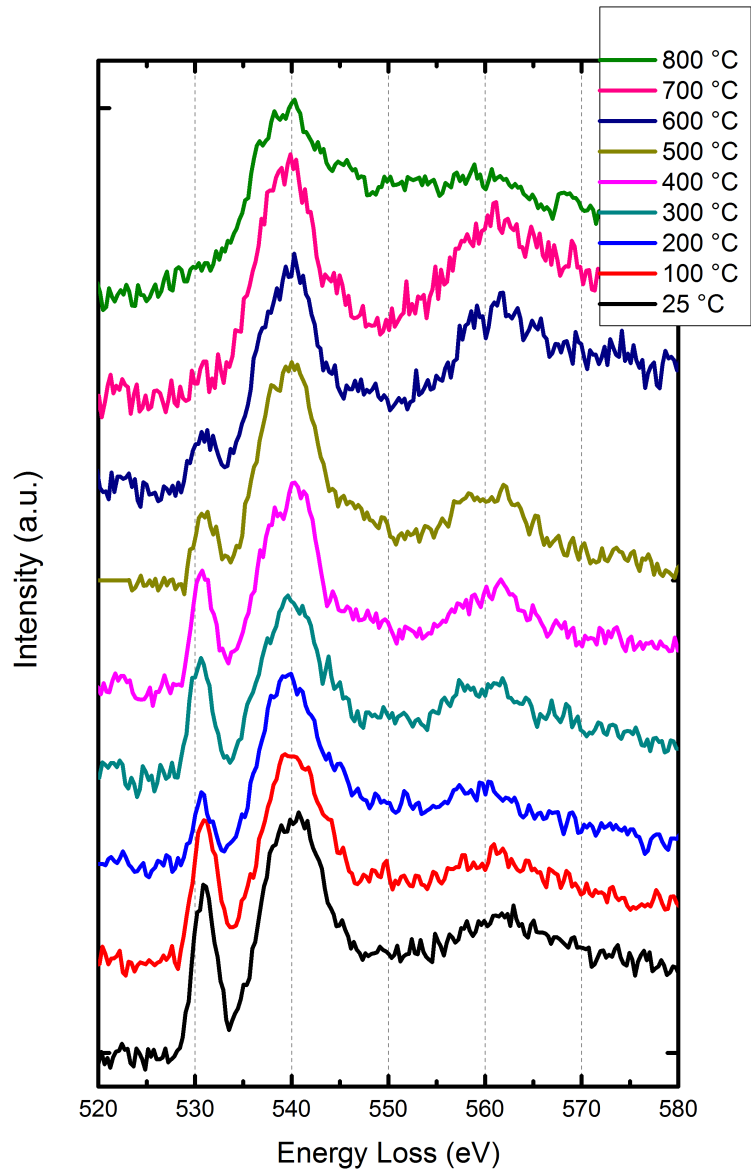


Figure 5.8 Oxygen edge of the electron energy loss spectrum of a NR during heating from 25°C to 800 °C.

β -FeOOH is a channel-like structure reminiscent of hollandite, comprising iron (III) atoms octahedrally coordinated to oxide and hydroxide ions. The tetragonal unit cell is

formed by corner-sharing double rows of octahedra along the *c* axis, with tunnels formed in the center. On heating in air, phase transformation results in α -Fe₂O₃, which has a corundum-type hexagonal structure (space group $R\bar{3}c$) with hexagonally close-packed oxygen matrix, and two-thirds occupancy of the octahedral sites by Fe(III). As the thermodynamically stable iron oxide phase at atmospheric conditions, α -Fe₂O₃ is unambiguously the product of β -FeOOH dehydration, though no clear structural relationship exists between β -FeOOH and α -Fe₂O₃. This phase transition has been utilized widely to synthesize α -Fe₂O₃ nanostructures.^{266,263,264,37,295–297}

The series of phase transitions observed in the TEM, however, are quite different, likely due both to the stabilization of reduced iron oxide phases under the low oxygen fugacity of the TEM column, and because the nanostructured morphology allows the kinetic trapping of phases with a topotactic relationship to their precursor. In the TEM we observe a progression from β -FeOOH first to β -Fe₂O₃, then γ -Fe₂O₃/Fe₃O₄, and finally FeO. Interestingly, all of these phases are supported by an underlying cubic close-packed oxygen anion matrix, except for β -FeOOH with a body-centered cubic anion arrangement (Fig. 5.9). β -Fe₂O₃ has a bixbyite-type body-centered cubic structure (space group $Ia\bar{3}$); γ -Fe₂O₃ and Fe₃O₄ have the spinel structure (space group $Fd\bar{3}m$), where γ -Fe₂O₃ has vacancies in the octahedral positions; and FeO has the rock salt structure (space group $Fm\bar{3}m$). Our observation of the phase-transition from β -FeOOH to cubic β -Fe₂O₃ represents the first report of this structural transition. (It should be noted that Braun et al. report a tetragonal “ β ”-Fe₂O₃ phase as a product of dehydrated β -FeOOH, for which this phase is structurally different from previous literature describing β -Fe₂O₃.^{288,298}) Previous reports of the decomposition of β -FeOOH under vacuum describe a transition first to γ -

Fe₂O₃ at below 500 °C, followed by a transformation to α-Fe₂O₃ at higher temperature.^{264,267,291} In contrast to this, we observe a transition to γ-Fe₂O₃ via the β-Fe₂O₃ intermediate, and a subsequent reduction first to the topotactic Fe₃O₄ spinel, and finally the rock salt-like FeO structure. Each of these transitions is favored by a clear structural relationship between the precursor and product (Fe₃O₄-like defect clusters are common low energy defects within FeO), suggesting that the transformation pathways require low activation energies, and may well be favored by kinetics, though it is also well known than small particle sizes selectively stabilize reduced forms of the iron oxides.²⁹⁹

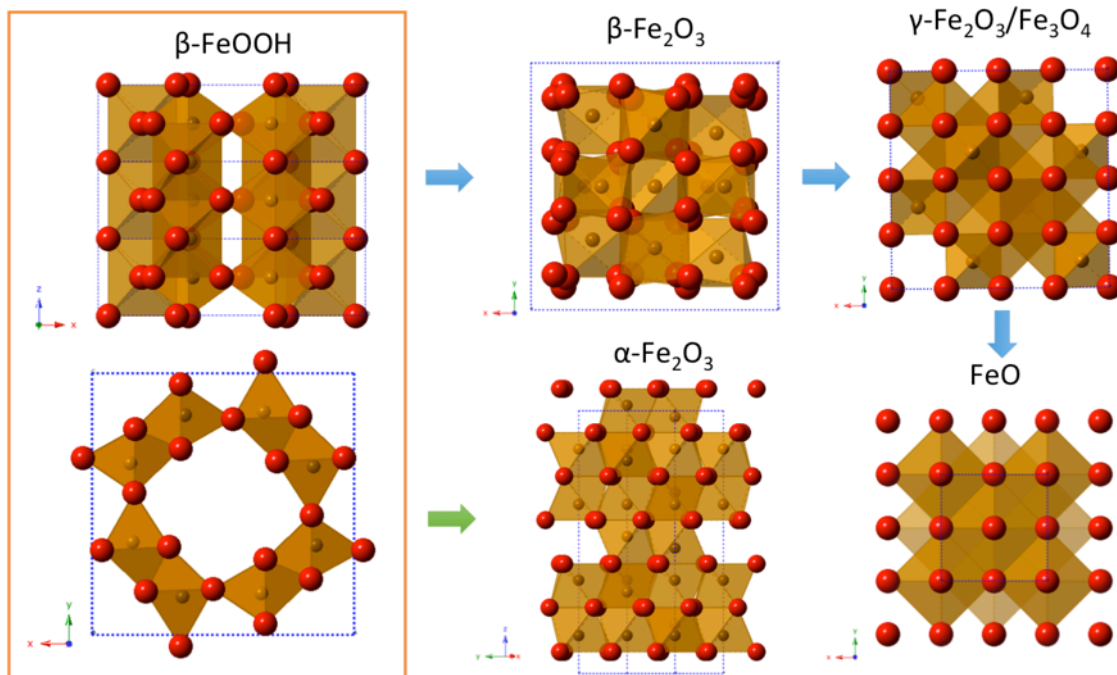


Figure 5.9 Graphical representations of crystal structures of β-FeOOH, β-Fe₂O₃, γ-Fe₂O₃/Fe₃O₄, FeO, α-Fe₂O₃. The brown spheres at the centers of polyhedrons and red spheres represent the iron and oxygen atoms respectively. The blue and green arrows stand for the phase transition paths in TEM and air correspondingly.

In order to check the consistency of our data analysis with mass conservation, we performed a density calculation for the NR shown in Fig. 5.5. As shown in Fig. 5.10, we calculated the volume of the NR by approximating it as a cylinder capped with two half

ellipsoids. The volumes of the NR before (at 25°C) and after (at 700°C) heating were thus calculated as $2.840 \times 10^6 \text{ nm}^3$ and $1.650 \times 10^6 \text{ nm}^3$ respectively. If we assume the iron atoms do not evaporate during heating, mass conservation dictates the resulting volumes of the possible species to be $1.909 \times 10^6 \text{ nm}^3$, $1.675 \times 10^6 \text{ nm}^3$ and $1.360 \times 10^6 \text{ nm}^3$ for $\gamma\text{-Fe}_2\text{O}_3$, Fe_3O_4 and FeO respectively. Comparing those volumes with the real resulting volume, we found the hollow NR is a mixture of both Fe_3O_4 and FeO , in complete agreement with the SAED and EELS data.

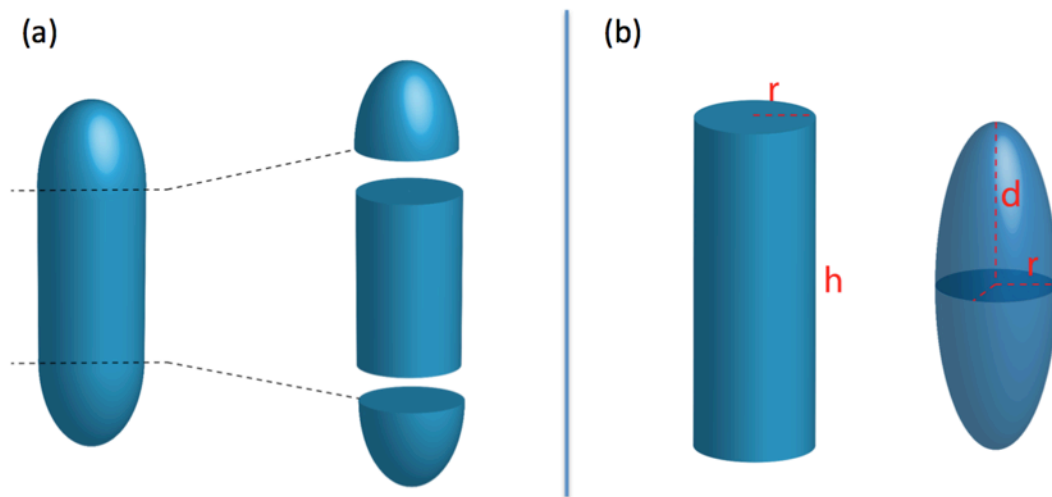


Figure 5.10 Cartoon showing the structure decomposition of a NR for density calculations

As a control experiment, we tried heating longer FeOOH wires without the curvature of the short rods. Using the same heating profiles as previously we saw the same solid to hollow transformation, in this case leading to an Fe_2O_3 tube as shown in Fig. 5.11, indicating the curvature of the NR is not the reason of hollowing.

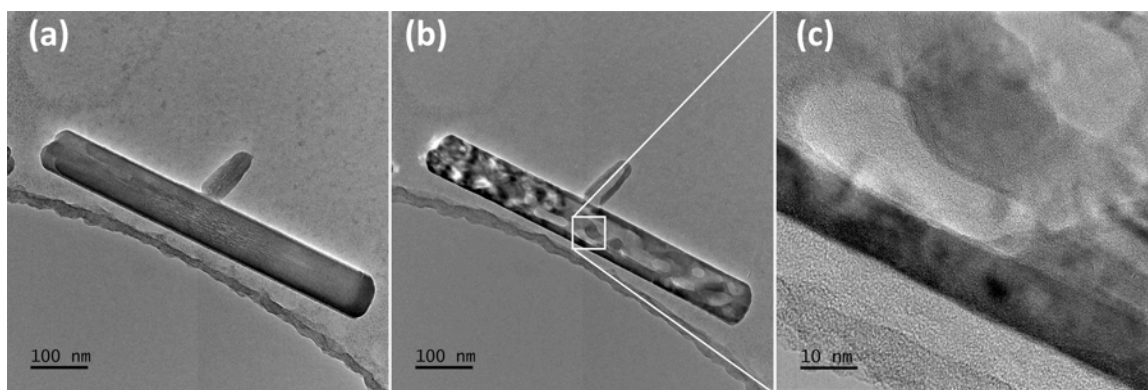


Figure 5.11 TEM images of an FeOOH NW before (a) and after (b) heating in TEM. The HRTEM image(c) shows the single-crystallinity of the hollow NW

A similar transformation of metal hydroxide to annealed porous oxide have also been observed in other systems, such as GaOOH/Ga₂O₃³⁰⁰, and Co(OH)₂/Co₃O₄³⁰¹. In these cases it was believed to be due to the volume contraction resulting from the loss of water, and also the transformation from a low-density metal (oxy) hydroxide to denser metal oxide; both of these factors apply also to the FeOOH/Fe_xO_y system reported here. Further, our *in situ* observations reveal that the initial decomposition from β-FeOOH to a structurally and thermodynamically more stable, and denser, iron oxide, produces a stable iron oxide shell within which all future transformations take place. Crucially, while particle size, system temperature and pressure, and the activation energies of transformation all undoubtedly play a role in dictating the resulting iron oxide phase, the hollow morphology depends only on the initial starting point, and is formed regardless of any heat treatments applied post-decomposition. *We have thus demonstrated the decoupling of phase/structure from morphology in the creation of a class of oxides with great potential for commercial application.* Briefly, the hollowing mechanism proceeds with the following steps (Fig. 5.12) the single crystal nanorod breaks into small crystals, followed by the formation of bigger crystals by dissolving and growing from the smaller

ones, to reduce the surface energy induced by the curvature; At the same time, a thin shell formed enclosing all the particles, after which the particles continuously grow into and thicken the shell till all been consumed. The shell formed at very beginning seems to play a very important role in capturing the small crystals during the hollowing process. As observed, this mechanism therefore possesses many of the usual characteristics of Ostwald ripening, with the added component of the larger, ripening, particles comprising the inner surface of a nanoshell. We therefore dub this mechanism “surface-confined Ostwald ripening.”

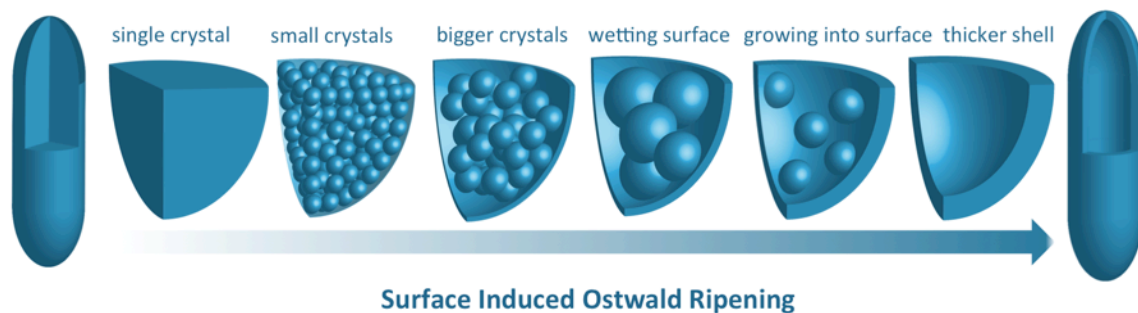


Figure 5.12 Surface-confined Ostwald ripening: the hollowing process observed for β -FeOOH NRs

5.4 Conclusion

In conclusion, a new mechanism for creating hollow nanostructures is observed, and dubbed surface-confined Ostwald ripening. β -FeOOH nanorods and nanowires were studied via *in situ* experiments, revealing a series of phase transformations from β -FeOOH, to β -Fe₂O₃, γ -Fe₂O₃, Fe₃O₄ and FeO under high vacuum, while a β -FeOOH to α -Fe₂O₃ transformation is observed in ambient and low vacuum conditions. Despite the wholly different structural transformations, both routes produced hollow nanorods with the same morphology, indicating that the crystal structure of the starting species is the

critical factor determining eventual morphology. This work reveals the ability to decouple the factors of morphology and structure in the design of useful nanomaterials.

REFERENCES

- (1) Ge, X.; Liu, Y.; Goh, F. W. T.; Hor, T. S. A.; Zong, Y.; Xiao, P.; Zhang, Z.; Lim, S. H.; Li, B.; Wang, X.; *et al.* Dual-Phase Spinel MnCo₂O₄ and Spinel MnCo₂O₄/Nanocarbon Hybrids for Electrocatalytic Oxygen Reduction and Evolution. *ACS Appl. Mater. Interfaces* **2014**, *6*, 12684–12691.
- (2) Rao, A.; Long, H.; Harley-Trochimczyk, A.; Pham, T.; Zettl, A.; Carraro, C.; Maboudian, R. *In Situ* Localized Growth of Ordered Metal Oxide Hollow Sphere Array on Microheater Platform for Sensitive, Ultra-Fast Gas Sensing. *ACS Appl. Mater. Interfaces* **2017**, *9*, 2634–2641.
- (3) Haque, S. A.; Koops, S.; Tokmoldin, N.; Durrant, J. R.; Huang, J.; Bradley, D. D. C.; Palomares, E. A Multilayered Polymer Light-Emitting Diode Using a Nanocrystalline Metal-Oxide Film as a Charge-Injection Electrode. *Adv. Mater.* **2007**, *19*, 683–687.
- (4) Ding, Y.; Xia, X.; Chen, W.; Hu, L.; Mo, L.; Huang, Y.; Dai, S. Inside-out Ostwald Ripening: A Facile Process towards Synthesizing Anatase TiO₂ Microspheres for High-Efficiency Dye-Sensitized Solar Cells. *Nano Res.* **2016**, *9*, 1891–1903.
- (5) Zhang, L.; Wu, H. B.; Lou, X. W. (David). Iron-Oxide-Based Advanced Anode Materials for Lithium-Ion Batteries. *Adv. Energy Mater.* **2014**, *4*, n/a-n/a.
- (6) Law, M.; Goldberger, J.; Yang, P. Semiconductor Nanowires and Nanotubes. *Annu. Rev. Mater. Res.* **2004**, *34*, 83–122.
- (7) Hobbs, R. G.; Petkov, N.; Holmes, J. D. Semiconductor Nanowire Fabrication by Bottom-Up and Top-Down Paradigms. *Chem. Mater.* **2012**, *24*, 1975–1991.
- (8) Tong, H. D.; Chen, S.; van der Wiel, W. G.; Carlen, E. T.; van den Berg, A. Novel Top-Down Wafer-Scale Fabrication of Single Crystal Silicon Nanowires. *Nano Lett.* **2009**, *9*, 1015–1022.
- (9) Chen, S.; Bomer, J. G.; van der Wiel, W. G.; Carlen, E. T.; van den Berg, A. Top-Down Fabrication of Sub-30 Nm Monocrystalline Silicon Nanowires Using Conventional Microfabrication. *ACS Nano* **2009**, *3*, 3485–3492.
- (10) Qi, H.; Glaser, E. R.; Caldwell, J. D.; Prokes, S. M.; Qi, H.; Glaser, E. R.; Caldwell, J. D.; Prokes, S. M. Growth of Vertically Aligned ZnO Nanowire Arrays Using Bilayered Metal Catalysts, Growth of Vertically Aligned ZnO Nanowire Arrays Using Bilayered Metal Catalysts. *J. Nanomater. J. Nanomater.* **2012**, *2012*, *2012*, e260687.
- (11) Luo, S.; Fan, J.; Liu, W.; Zhang, M.; Song, Z.; Lin, C.; Wu, X.; Chu, P. K. Synthesis and Low-Temperature Photoluminescence Properties of SnO₂ Nanowires and Nanobelts. *Nanotechnology* **2006**, *17*, 1695.
- (12) Auer, E.; Lugstein, A.; Löffler, S.; Hyun, Y. J.; Brezna, W.; Bertagnolli, E.; Pongratz, P. Ultrafast VLS Growth of Epitaxial β-Ga₂O₃ Nanowires. *Nanotechnology* **2009**, *20*, 434017.
- (13) Zhuge, F.; Yanagida, T.; Nagashima, K.; Yoshida, H.; Kanai, M.; Xu, B.; Klamchuen, A.; Meng, G.; He, Y.; Rahong, S.; *et al.* Fundamental Strategy for Creating VLS Grown TiO₂ Single Crystalline Nanowires. *J. Phys. Chem. C* **2012**, *116*, 24367–24372.

- (14) Liu, B.; Zeng, H. C. Hydrothermal Synthesis of ZnO Nanorods in the Diameter Regime of 50 Nm. *J. Am. Chem. Soc.* **2003**, *125*, 4430–4431.
- (15) Wang, X.; Li, Y. Selected-Control Hydrothermal Synthesis of α - and β -MnO₂ Single Crystal Nanowires. *J. Am. Chem. Soc.* **2002**, *124*, 2880–2881.
- (16) Wang, G.; Gou, X.; Horvat, J.; Park, J. Facile Synthesis and Characterization of Iron Oxide Semiconductor Nanowires for Gas Sensing Application. *J. Phys. Chem. C* **2008**, *112*, 15220–15225.
- (17) Wei, C.; Xu, C.; Li, B.; Nan, D.; Ma, J.; Kang, F. Formation and Conversion Mechanisms between Single-Crystal Gamma-MnOOH and Manganese Oxides. *Mater. Res. Bull.* **2012**, *47*, 1740–1746.
- (18) Meng, F.; Morin, S. A.; Jin, S. Rational Solution Growth of α -FeOOH Nanowires Driven by Screw Dislocations and Their Conversion to α -Fe₂O₃ Nanowires. *J. Am. Chem. Soc.* **2011**, *133*, 8408–8411.
- (19) Hastings, J. M.; Corliss, L. M. Neutron Diffraction Study of Manganese Ferrite. *Phys. Rev.* **1956**, *104*, 328–331.
- (20) Liu, C.; Zou, B.; Rondinone, A. J.; Zhang, Z. J. Chemical Control of Superparamagnetic Properties of Magnesium and Cobalt Spinel Ferrite Nanoparticles through Atomic Level Magnetic Couplings. *J. Am. Chem. Soc.* **2000**, *122*, 6263–6267.
- (21) Garlea, V. O.; Jin, R.; Mandrus, D.; Roessli, B.; Huang, Q.; Miller, M.; Schultz, A. J.; Nagler, S. E. Magnetic and Orbital Ordering in the Spinel MnV₂O₄. *Phys. Rev. Lett.* **2008**, *100*, 66404.
- (22) Yu, L.; Zhang, Y.; Hudak, B. M.; Wallace, D. K.; Kim, D. Y.; Guiton, B. S. Simple Synthetic Route to Manganese-Containing Nanowires with the Spinel Crystal Structure. *J. Solid State Chem.* **2016**, *240*, 23–29.
- (23) Ma, F.-X.; Hu, H.; Wu, H. B.; Xu, C.-Y.; Xu, Z.; Zhen, L.; (David) Lou, X. W. Formation of Uniform Fe₃O₄ Hollow Spheres Organized by Ultrathin Nanosheets and Their Excellent Lithium Storage Properties. *Adv. Mater.* **2015**, *27*, 4097–4101.
- (24) Kandambeth, S.; Venkatesh, V.; Shinde, D. B.; Kumari, S.; Halder, A.; Verma, S.; Banerjee, R. Self-Templated Chemically Stable Hollow Spherical Covalent Organic Framework. *Nat. Commun.* **2015**, *6*, 6786.
- (25) Zhang, A.-Q.; Li, H.-J.; Qian, D.-J.; Chen, M. Kinetically-Controlled Template-Free Synthesis of Hollow Silica Micro-/Nanostructures with Unusual Morphologies. *Nanotechnology* **2014**, *25*, 135608.
- (26) Zhang, H.; Yang, D.; Ji, Y.; Ma, X.; Xu, J.; Que, D. Low Temperature Synthesis of Flowerlike ZnO Nanostructures by Cetyltrimethylammonium Bromide-Assisted Hydrothermal Process. *J. Phys. Chem. B* **2004**, *108*, 3955–3958.
- (27) Mai, H.-X.; Sun, L.-D.; Zhang, Y.-W.; Si, R.; Feng, W.; Zhang, H.-P.; Liu, H.-C.; Yan, C.-H. Shape-Selective Synthesis and Oxygen Storage Behavior of Ceria Nanopolyhedra, Nanorods, and Nanocubes. *J. Phys. Chem. B* **2005**, *109*, 24380–24385.
- (28) Fang, Y.-P.; Xu, A.-W.; Song, R.-Q.; Zhang, H.-X.; You, L.-P.; Yu, J. C.; Liu, H.-Q. Systematic Synthesis and Characterization of Single-Crystal Lanthanide Orthophosphate Nanowires. *J. Am. Chem. Soc.* **2003**, *125*, 16025–16034.

- (29) Armstrong, A. R.; Armstrong, G.; Canales, J.; Bruce, P. G. TiO₂-B Nanowires. *Angew. Chem. Int. Ed.* **2004**, *43*, 2286–2288.
- (30) Huang, X. J. *Nanotechnology Research: New Nanostructures, Nanotubes and Nanofibers*; Nova Publishers, 2008.
- (31) Yu, S.-H.; Liu, B.; Mo, M.-S.; Huang, J.-H.; Liu, X.-M.; Qian, Y.-T. General Synthesis of Single-Crystal Tungstate Nanorods/Nanowires: A Facile, Low-Temperature Solution Approach. *Adv. Funct. Mater.* **2003**, *13*, 639–647.
- (32) Chen, X. Y.; Huh, H. S.; Lee, S. W. Hydrothermal Synthesis of Boehmite (γ -AlOOH) Nanoplatelets and Nanowires: pH-Controlled Morphologies. *Nanotechnology* **2007**, *18*, 285608.
- (33) Liu, B.; Aydil, E. S. Growth of Oriented Single-Crystalline Rutile TiO₂ Nanorods on Transparent Conducting Substrates for Dye-Sensitized Solar Cells. *J. Am. Chem. Soc.* **2009**, *131*, 3985–3990.
- (34) Pu, Z.; Cao, M.; Yang, J.; Huang, K.; Hu, C. Controlled Synthesis and Growth Mechanism of Hematite Nanorhombhedra, Nanorods and Nanocubes. *Nanotechnology* **2006**, *17*, 799.
- (35) Duan, X.; Yang, J.; Gao, H.; Ma, J.; Jiao, L.; Zheng, W. Controllable Hydrothermal Synthesis of Manganese Dioxide Nanostructures: Shape Evolution, Growth Mechanism and Electrochemical Properties. *CrystEngComm* **2012**, *14*, 4196–4204.
- (36) Chevalier-César, C.; Capochichi-Gnambodoe, M.; Leprince-Wang, Y. Growth Mechanism Studies of ZnO Nanowire Arrays via Hydrothermal Method. *Appl. Phys. Mater. Sci. Process.* **2014**, *115*, 953–960.
- (37) Wang, X.; Chen, X.; Gao, L.; Zheng, H.; Ji, M.; Tang, C.; Shen, T.; Zhang, Z. Synthesis of β -FeOOH and α -Fe₂O₃ Nanorods and Electrochemical Properties of β -FeOOH. *J. Mater. Chem.* **2004**, *14*, 905–907.
- (38) Sun, Y.; Li, C.; Wang, L.; Wang, Y.; Ma, X.; Ma, P.; Song, M. Ultralong Monoclinic ZnV₂O₆ Nanowires: Their Shape-Controlled Synthesis, New Growth Mechanism, and Highly Reversible Lithium Storage in Lithium-Ion Batteries. *RSC Adv.* **2012**, *2*, 8110.
- (39) Huang, M. H.; Mao, S.; Feick, H.; Yan, H.; Wu, Y.; Kind, H.; Weber, E.; Russo, R.; Yang, P. Room-Temperature Ultraviolet Nanowire Nanolasers. *Science* **2001**, *292*, 1897–1899.
- (40) Wang, X.; Li, Y. Synthesis and Characterization of Lanthanide Hydroxide Single-Crystal Nanowires. *Angew. Chem. Int. Ed.* **2002**, *41*, 4790–4793.
- (41) Ruan, H.; Wang, R.; Luo, Y.; Liu, H.; Han, T.; Yang, L. Study on Synthesis and Growth Mechanism of Copper Nanowires via a Facile Oleylamine-Mediated Process. *J. Mater. Sci. Mater. Electron.* **2016**, *27*, 9405–9409.
- (42) Liu, Z.; Li, S.; Yang, Y.; Peng, S.; Hu, Z.; Qian, Y. Complex-Surfactant-Assisted Hydrothermal Route to Ferromagnetic Nickel Nanobelts. *Adv. Mater.* **2003**, *15*, 1946–1948.
- (43) Cordente, N.; Respaud, M.; Senocq, F.; Casanove, M.-J.; Amiens, C.; Chaudret, B. Synthesis and Magnetic Properties of Nickel Nanorods. *Nano Lett.* **2001**, *1*, 565–568.
- (44) Sun, Y.; Xia, Y. Shape-Controlled Synthesis of Gold and Silver Nanoparticles. *Science*, **2002**, *298*, 2176–2179.

- (45) Sun, Y.; Gates, B.; Mayers, B.; Xia, Y. Crystalline Silver Nanowires by Soft Solution Processing. *Nano Lett.* **2002**, *2*, 165–168.
- (46) Sun, Y.; Yin, Y.; Mayers, B. T.; Herricks, T.; Xia, Y. Uniform Silver Nanowires Synthesis by Reducing AgNO₃ with Ethylene Glycol in the Presence of Seeds and Poly(Vinyl Pyrrolidone). *Chem. Mater.* **2002**, *14*, 4736–4745.
- (47) Caswell, K. K.; Bender, C. M.; Murphy, C. J. Seedless, Surfactantless Wet Chemical Synthesis of Silver Nanowires. *Nano Lett.* **2003**, *3*, 667–669.
- (48) Joo, J.; Chow, B. Y.; Prakash, M.; Boyden, E. S.; Jacobson, J. M. Face-Selective Electrostatic Control of Hydrothermal Zinc Oxide Nanowire Synthesis. *Nat. Mater.* **2011**, *10*, 596–601.
- (49) Shandilya, M.; Rai, R.; Singh, J. Review: Hydrothermal Technology for Smart Materials. *Adv. Appl. Ceram.* **2016**, *115*, 354–376.
- (50) Phuruangrat, A.; Ham, D. J.; Hong, S. J.; Thongtem, S.; Lee, J. S. Synthesis of Hexagonal WO₃ Nanowires by Microwave-Assisted Hydrothermal Method and Their Electrocatalytic Activities for Hydrogen Evolution Reaction. *J. Mater. Chem.* **2010**, *20*, 1683–1690.
- (51) Yeo, J.; Hong, S.; Kim, G.; Lee, H.; Suh, Y. D.; Park, I.; Grigoropoulos, C. P.; Ko, S. H. Laser-Induced Hydrothermal Growth of Heterogeneous Metal-Oxide Nanowire on Flexible Substrate by Laser Absorption Layer Design. *ACS Nano* **2015**, *9*, 6059–6068.
- (52) Wagner, R. S.; Ellis, W. C. Vapor-Liquid-Solid Mechanism of Single Crystal Growth. *Appl. Phys. Lett.* **1964**, *4*, 89–90.
- (53) Wu, Y.; Yang, P. Direct Observation of Vapor- Liquid- Solid Nanowire Growth. *J. Am. Chem. Soc.* **2001**, *123*, 3165–3166.
- (54) Cui, Y.; Lauhon, L. J.; Gudiksen, M. S.; Wang, J.; Lieber, C. M. Diameter-Controlled Synthesis of Single-Crystal Silicon Nanowires. *Appl. Phys. Lett.* **2001**, *78*, 2214–2216.
- (55) Sunkara, M. K.; Sharma, S.; Miranda, R.; Lian, G.; Dickey, E. C. Bulk Synthesis of Silicon Nanowires Using a Low-Temperature Vapor–liquid–solid Method. *Appl. Phys. Lett.* **2001**, *79*, 1546–1548.
- (56) Adhikari, H.; Marshall, A. F.; Goldthorpe, I. A.; Chidsey, C. E. D.; McIntyre, P. C. Metastability of Au–Ge Liquid Nanocatalysts: Ge Vapor–Liquid–Solid Nanowire Growth Far below the Bulk Eutectic Temperature. *ACS Nano* **2007**, *1*, 415–422.
- (57) Ahlén, N.; Johnsson, M.; Nygren, M. Carbothermal Synthesis of TiC Whiskers via a Vapor-Liquid-Solid Growth Mechanism. *J. Am. Ceram. Soc.* **1996**, *79*, 2803–2808.
- (58) Chen, C.-C.; Yeh, C.-C.; others. Large-Scale Catalytic Synthesis of Crystalline Gallium Nitride Nanowires. *Adv. Mater.* **2000**, *12*, 738–741.
- (59) Yang, P.; Yan, H.; Mao, S.; Russo, R.; Johnson, J.; Saykally, R.; Morris, N.; Pham, J.; He, R.; Choi, H.-J. Controlled Growth of ZnO Nanowires and Their Optical Properties. *Adv. Funct. Mater.* **2002**, *12*, 323.
- (60) Gudiksen, M. S.; Lieber, C. M. Diameter-Selective Synthesis of Semiconductor Nanowires. *J. Am. Chem. Soc.* **2000**, *122*, 8801–8802.
- (61) Wang, Y.; Schmidt, V.; Senz, S.; Gösele, U. Epitaxial Growth of Silicon Nanowires Using an Aluminium Catalyst. *Nat. Nanotechnol.* **2006**, *1*, 186–189.

- (62) Song, J.; Wang, X.; Riedo, E.; Wang, Z. L. Elastic Property of Vertically Aligned Nanowires. *Nano Lett.* **2005**, *5*, 1954–1958.
- (63) Kuykendall, T. R.; Altoe, M. V. P.; Ogletree, D. F.; Aloni, S. Catalyst-Directed Crystallographic Orientation Control of GaN Nanowire Growth. *Nano Lett.* **2014**, *14*, 6767–6773.
- (64) Hannon, J. B.; Kodambaka, S.; Ross, F. M.; Tromp, R. M. The Influence of the Surface Migration of Gold on the Growth of Silicon Nanowires. *Nature* **2006**, *440*, 69–71.
- (65) Stelzner, T.; Andrä, G.; Wendler, E.; Wesch, W.; Scholz, R.; Gösele, U.; Christiansen, S. Growth of Silicon Nanowires by Chemical Vapour Deposition on Gold Implanted Silicon Substrates. *Nanotechnology* **2006**, *17*, 2895.
- (66) Yu, L.; Riddle, A. J.; Wang, S.; Sundararajan, A.; Thompson, J.; Chang, Y.-J.; Park, M. E.; Seo, S. S. A.; Guiton, B. S. Solid–Liquid–Vapor Synthesis of Negative Metal Oxide Nanowire Arrays. *Chem. Mater.* **2016**, *28*, 8924–8929.
- (67) Schoen, D. T.; Peng, H.; Cui, Y. Anisotropy of Chemical Transformation from In₂Se₃ to CuInSe₂ Nanowires through Solid State Reaction. *J. Am. Chem. Soc.* **2009**, *131*, 7973–7975.
- (68) Zhang, D.; Yang, Y.; Bekenstein, Y.; Yu, Y.; Gibson, N. A.; Wong, A. B.; Eaton, S. W.; Kornienko, N.; Kong, Q.; Lai, M.; *et al.* Synthesis of Composition Tunable and Highly Luminescent Cesium Lead Halide Nanowires through Anion-Exchange Reactions. *J. Am. Chem. Soc.* **2016**, *138*, 7236–7239.
- (69) Jeong, U.; Camargo, P. H. C.; Lee, Y. H.; Xia, Y. Chemical Transformation: A Powerful Route to Metal Chalcogenide Nanowires. *J. Mater. Chem.* **2006**, *16*, 3893.
- (70) Gates, B.; Mayers, B.; Cattle, B.; Xia, Y. Synthesis and Characterization of Uniform Nanowires of Trigonal Selenium. *Adv. Funct. Mater.* **2002**, *12*, 219–227.
- (71) Jiang, X.; Mayers, B.; Herricks, T.; Xia, Y. Direct Synthesis of Se@CdSe Nanocables and CdSe Nanotubes by Reacting Cadmium Salts with Se Nanowires. *Adv. Mater.* **2003**, *15*, 1740–1743.
- (72) Wu, Y.; Messer, B.; Yang, P. Superconducting MgB₂ Nanowires. *Adv. Mater.* **2001**, *13*, 1487–1489.
- (73) Yang, L.; Liu, D.; Hao, S.; Qu, F.; Ge, R.; Ma, Y.; Du, G.; Asiri, A. M.; Chen, L.; Sun, X. Topotactic Conversion of α -Fe₂O₃ Nanowires into FeP as a Superior Fluorosensor for Nucleic Acid Detection: Insights from Experiment and Theory. *Anal. Chem.* **2017**, *89*, 2191–2195.
- (74) Jiang, P.; Liu, Q.; Liang, Y.; Tian, J.; Asiri, A. M.; Sun, X. A Cost-Effective 3D Hydrogen Evolution Cathode with High Catalytic Activity: FeP Nanowire Array as the Active Phase. *Angew. Chem. Int. Ed.* **2014**, *53*, 12855–12859.
- (75) Tian, J.; Liu, Q.; Asiri, A. M.; Sun, X. Self-Supported Nanoporous Cobalt Phosphide Nanowire Arrays: An Efficient 3D Hydrogen-Evolving Cathode over the Wide Range of pH 0–14. *J. Am. Chem. Soc.* **2014**, *136*, 7587–7590.
- (76) Tian, J.; Liu, Q.; Cheng, N.; Asiri, A. M.; Sun, X. Self-Supported Cu₃P Nanowire Arrays as an Integrated High-Performance Three-Dimensional Cathode for Generating Hydrogen from Water. *Angew. Chem. Int. Ed.* **2014**, *53*, 9577–9581.

- (77) Tang, C.; Gan, L.; Zhang, R.; Lu, W.; Jiang, X.; Asiri, A. M.; Sun, X.; Wang, J.; Chen, L. Ternary $\text{Fe}_x\text{Co}_{1-x}\text{P}$ Nanowire Array as a Robust Hydrogen Evolution Reaction Electrocatalyst with Pt-like Activity: Experimental and Theoretical Insight. *Nano Lett.* **2016**, *16*, 6617–6621.
- (78) Kolmakov, A.; Zhang, Y.; Moskovits, M. Topotactic Thermal Oxidation of Sn Nanowires: Intermediate Suboxides and Core–Shell Metastable Structures. *Nano Lett.* **2003**, *3*, 1125–1129.
- (79) Li, L.; Yang, Y.-W.; Li, G.-H.; Zhang, L.-D. Conversion of a Bi Nanowire Array to an Array of Bi– Bi_2O_3 Core–Shell Nanowires and Bi_2O_3 Nanotubes. *Small* **2006**, *2*, 548–553.
- (80) Shan, C. X.; Liu, Z.; Zhang, Z. Z.; Shen, D. Z.; Hark, S. K. A Simple Route to Porous ZnO and ZnCdO Nanowires. *J. Phys. Chem. B* **2006**, *110*, 11176–11179.
- (81) Wu, W. W.; Lu, K. C.; Wang, C. W.; Hsieh, H. Y.; Chen, S. Y.; Chou, Y. C.; Yu, S. Y.; Chen, L. J.; Tu, K. N. Growth of Multiple Metal/Semiconductor Nanoheterostructures through Point and Line Contact Reactions. *Nano Lett.* **2010**, *10*, 3984–3989.
- (82) Liu, C.-Y.; Li, W.-S.; Chu, L.-W.; Lu, M.-Y.; Tsai, C.-J.; Chen, L.-J. An Ordered Si Nanowire with NiSi_2 Tip Arrays as Excellent Field Emitters. *Nanotechnology* **2011**, *22*, 55603.
- (83) Lee, S.; Yoon, J.; Koo, B.; Shin, D. H.; Koo, J. H.; Lee, C. J.; Kim, Y. W.; Kim, H.; Lee, T. Formation of Vertically Aligned Cobalt Silicide Nanowire Arrays Through a Solid-State Reaction. *IEEE Trans. Nanotechnol.* **2013**, *12*, 704–711.
- (84) Liu, H.; She, G.; Huang, X.; Qi, X.; Mu, L.; Meng, X.; Shi, W. Synthesis and Magnetic Properties of Mn_4Si_7 and Si– Mn_4Si_7 Axial Heterostructure Nanowire Arrays. *J. Phys. Chem. C* **2013**, *117*, 2377–2381.
- (85) Kang, Y.; Vaddiraju, S. Solid-State Phase Transformation as a Route for the Simultaneous Synthesis and Welding of Single-Crystalline Mg_2Si Nanowires. *Chem. Mater.* **2014**, *26*, 2814–2819.
- (86) Hong Jin Fan; Knez, M.; Scholz, R.; Nielsch, K.; Pippel, E.; Hesse, D.; Zacharias, M.; Gösele, U. Monocrystalline Spinel Nanotube Fabrication Based on the Kirkendall Effect. *Nat. Mater.* **2006**, *5*, 627–631.
- (87) Lee, H.-W.; Muralidharan, P.; Ruffo, R.; Mari, C. M.; Cui, Y.; Kim, D. K. Ultrathin Spinel LiMn_2O_4 Nanowires as High Power Cathode Materials for Li-Ion Batteries. *Nano Lett.* **2010**, *10*, 3852–3856.
- (88) Mukherjee, A.; Ardakani, H. A.; Yi, T.; Cabana, J.; Shahbazian-Yassar, R.; Klie, R. F. Direct Characterization of the Li Intercalation Mechanism into $\alpha\text{-V}_2\text{O}_5$ Nanowires Using *in-Situ* Transmission Electron Microscopy. *Appl. Phys. Lett.* **2017**, *110*, 213903.
- (89) Xu, X.; Luo, Y.-Z.; Mai, L.-Q.; Zhao, Y.-L.; An, Q.-Y.; Xu, L.; Hu, F.; Zhang, L.; Zhang, Q.-J. Topotactically Synthesized Ultralong LiV_3O_8 Nanowire Cathode Materials for High-Rate and Long-Life Rechargeable Lithium Batteries. *NPG Asia Mater.* **2012**, *4*, e20.
- (90) Liu, X. H.; Zheng, H.; Zhong, L.; Huang, S.; Karki, K.; Zhang, L. Q.; Liu, Y.; Kushima, A.; Liang, W. T.; Wang, J. W.; *et al.* Anisotropic Swelling and Fracture of Silicon Nanowires during Lithiation. *Nano Lett.* **2011**, *11*, 3312–3318.

- (91) Wang, C.-M.; Xu, W.; Liu, J.; Zhang, J.-G.; Saraf, L. V.; Arey, B. W.; Choi, D.; Yang, Z.-G.; Xiao, J.; Thevuthasan, S.; *et al.* *In Situ* Transmission Electron Microscopy Observation of Microstructure and Phase Evolution in a SnO₂ Nanowire during Lithium Intercalation. *Nano Lett.* **2011**, *11*, 1874–1880.
- (92) Liu, X. H.; Huang, S.; Picraux, S. T.; Li, J.; Zhu, T.; Huang, J. Y. Reversible Nanopore Formation in Ge Nanowires during Lithiation–Delithiation Cycling: An *In Situ* Transmission Electron Microscopy Study. *Nano Lett.* **2011**, *11*, 3991–3997.
- (93) Schoen, D. T.; Peng, H.; Cui, Y. CuInSe₂ Nanowires from Facile Chemical Transformation of In₂Se₃ and Their Integration in Single-Nanowire Devices. *ACS Nano* **2013**, *7*, 3205–3211.
- (94) Gao, T.; Jelle, B. P. Paraotwayite-Type α -Ni(OH)₂ Nanowires: Structural, Optical, and Electrochemical Properties. *J. Phys. Chem. C* **2013**, *117*, 17294–17302.
- (95) Liang, S.; Islam, R.; Smith, D. J.; Bennett, P. A. Phase Transformation in FeSi₂ Nanowires. *J. Cryst. Growth* **2006**, *295*, 166–171.
- (96) Pienack, N.; Bensch, W. In-Situ Monitoring of the Formation of Crystalline Solids. *Angew. Chem. Int. Ed.* **2011**, *50*, 2014–2034.
- (97) Chuvilin, A.; Kaiser, U.; Bichoutskaia, E.; Besley, N. A.; Khlobystov, A. N. Direct Transformation of Graphene to Fullerene. *Nat. Chem.* **2010**, *2*, 450–453.
- (98) Weber, W. J.; Ewing, R. C.; Wang, L.-M. The Radiation-Induced Crystalline-to-Amorphous Transition in Zircon. *J. Mater. Res.* **1994**, *9*, 688–698.
- (99) Liu, B. H.; Teo, H. W.; Mo, Z. H.; Mai, Z. H.; Lam, J.; Xue, J. M.; Zhao, Y. Z.; Tan, P. K. *In Situ* TEM Study of Electron-Beam Radiation Induced Boron Diffusion and Effects on Phase and Microstructure Evolution in Nanostructured CoFeB/SiO₂ Thin Film. *J. Appl. Phys.* **2017**, *121*, 15111.
- (100) Rankin, J. *In Situ* TEM Heating of Nanosized ZrO₂. *J. Am. Ceram. Soc.* **1999**, *82*, 1560–1564.
- (101) Chen, C.; Hu, Z.; Li, Y.; Liu, L.; Mori, H.; Wang, Z. *In-Situ* High-Resolution Transmission Electron Microscopy Investigation of Overheating of Cu Nanoparticles. *Sci. Rep.* **2016**, *6*, 19545.
- (102) Agarwal, R.; Zakharov, D. N.; Krook, N. M.; Liu, W.; Berger, J. S.; Stach, E. A.; Agarwal, R. Real-Time Observation of Morphological Transformations in II–VI Semiconducting Nanobelts via Environmental Transmission Electron Microscopy. *Nano Lett.* **2015**, *15*, 3303–3308.
- (103) Parsons, D. F. Structure of Wet Specimens in Electron Microscopy. *Science* **1974**, *186*, 407–414.
- (104) Sun, L.; Noh, K. W.; Wen, J.-G.; Dillon, S. J. *In Situ* Transmission Electron Microscopy Observation of Silver Oxidation in Ionized/Atomic Gas. *Langmuir* **2011**, *27*, 14201–14206.
- (105) Vendelbo, S. B.; Elkjær, C. F.; Falsig, H.; Puspitasari, I.; Dona, P.; Mele, L.; Morana, B.; Nelissen, B. J.; van Rijn, R.; Creemer, J. F.; *et al.* Visualization of Oscillatory Behaviour of Pt Nanoparticles Catalysing CO Oxidation. *Nat. Mater.* **2014**, *13*, 884–890.
- (106) Williamson, M. J.; Tromp, R. M.; Vereecken, P. M.; Hull, R.; Ross, F. M. Dynamic Microscopy of Nanoscale Cluster Growth at the Solid–liquid Interface. *Nat. Mater.* **2003**, *2*, 532–536.

- (107) Radisic, A.; Vereecken, P. M.; Hannon, J. B.; Searson, P. C.; Ross, F. M. Quantifying Electrochemical Nucleation and Growth of Nanoscale Clusters Using Real-Time Kinetic Data. *Nano Lett.* **2006**, *6*, 238–242.
- (108) Lu, Y.; Peng, C.; Ganesan, Y.; Huang, J. Y.; Lou, J. Quantitative *in Situ* TEM Tensile Testing of an Individual Nickel Nanowire. *Nanotechnology* **2011**, *22*, 355702.
- (109) Chen, C. Q.; Pei, Y. T.; De Hosson, J. T. M. Effects of Size on the Mechanical Response of Metallic Glasses Investigated through *in Situ* TEM Bending and Compression Experiments. *Acta Mater.* **2010**, *58*, 189–200.
- (110) Lee, S.; Im, J.; Yoo, Y.; Bitzek, E.; Kiener, D.; Richter, G.; Kim, B.; Oh, S. H. Reversible Cyclic Deformation Mechanism of Gold Nanowires by Twinning–detwinning Transition Evidenced from *in Situ* TEM. *Nat. Commun.* **2014**, *5*, ncomms4033.
- (111) Wang, J.; Zeng, Z.; Weinberger, C. R.; Zhang, Z.; Zhu, T.; Mao, S. X. *In Situ* Atomic-Scale Observation of Twinning-Dominated Deformation in Nanoscale Body-Centred Cubic Tungsten. *Nat. Mater.* **2015**, *14*, 594–600.
- (112) Schoen, D. T.; Xie, C.; Cui, Y. Electrical Switching and Phase Transformation in Silver Selenide Nanowires. *J. Am. Chem. Soc.* **2007**, *129*, 4116–4117.
- (113) Chou, Y.-C.; Wu, W.-W.; Cheng, S.-L.; Yoo, B.-Y.; Myung, N.; Chen, L. J.; Tu, K. N. *In-Situ* TEM Observation of Repeating Events of Nucleation in Epitaxial Growth of Nano CoSi₂ in Nanowires of Si. *Nano Lett.* **2008**, *8*, 2194–2199.
- (114) Hsieh, Y.-H.; Chiu, C.-H.; Huang, C.-W.; Chen, J.-Y.; Lin, W.-J.; Wu, W.-W. Dynamic Observation on the Growth Behaviors in Manganese Silicide/Silicon Nanowire Heterostructures. *Nanoscale* **2015**, *7*, 1776–1781.
- (115) Chen, Y. H.; Huang, C. W.; Yeh, P. H.; Chen, J. Y.; Lin, T. Y.; Chang, C. F.; Wu, W. W. A Solid-State Cation Exchange Reaction to Form Multiple Metal Oxide Heterostructure Nanowires. *Nanoscale* **2016**, *8*, 17039–17043.
- (116) Sun, X.; Yu, B.; Ng, G.; Nguyen, T. D.; Meyyappan, M. III-VI Compound Semiconductor Indium Selenide (In₂Se₃) Nanowires: Synthesis and Characterization. *Appl. Phys. Lett.* **2006**, *89*, 233121.
- (117) Persson, A. I.; Larsson, M. W.; Stenström, S.; Ohlsson, B. J.; Samuelson, L.; Wallenberg, L. R. Solid-Phase Diffusion Mechanism for GaAs Nanowire Growth. *Nat. Mater.* **2004**, *3*, 677–681.
- (118) Boston, R.; Schnepf, Z.; Nemoto, Y.; Sakka, Y.; Hall, S. R. *In Situ* TEM Observation of a Microcrucible Mechanism of Nanowire Growth. *Science* **2014**, *344*, 623–626.
- (119) Hudak, B. M.; Chang, Y.-J.; Yu, L.; Li, G.; Edwards, D. N.; Guiton, B. S. Real-Time Observation of the Solid–Liquid–Vapor Dissolution of Individual Tin(IV) Oxide Nanowires. *ACS Nano* **2014**, *8*, 5441–5448.
- (120) Hsin, C.-L.; Huang, C.-W.; Chen, J.-Y.; Liao, K.-C.; Liu, P.-L.; Wu, W.-W.; Chen, L.-J. Direct Observation of Sublimation Behaviors in One-Dimensional In₂Se₃/In₂O₃ Nanoheterostructures. *Anal. Chem.* **2015**, *87*, 5584–5588.
- (121) Wang, C.-M.; Li, X.; Wang, Z.; Xu, W.; Liu, J.; Gao, F.; Kovarik, L.; Zhang, J.-G.; Howe, J.; Burton, D. J.; *et al.* *In Situ* TEM Investigation of Congruent Phase Transition and Structural Evolution of Nanostructured Silicon/Carbon Anode for Lithium Ion Batteries. *Nano Lett.* **2012**, *12*, 1624–1632.

- (122) Gu, M.; Li, Y.; Li, X.; Hu, S.; Zhang, X.; Xu, W.; Thevuthasan, S.; Baer, D. R.; Zhang, J.-G.; Liu, J.; *et al.* *In Situ* TEM Study of Lithiation Behavior of Silicon Nanoparticles Attached to and Embedded in a Carbon Matrix. *ACS Nano* **2012**, *6*, 8439–8447.
- (123) McDowell, M. T.; Lee, S. W.; Harris, J. T.; Korgel, B. A.; Wang, C.; Nix, W. D.; Cui, Y. *In Situ* TEM of Two-Phase Lithiation of Amorphous Silicon Nanospheres. *Nano Lett.* **2013**, *13*, 758–764.
- (124) Li, G.; Yu, L.; Hudak, B. M.; Chang, Y.-J.; Baek, H.; Sundararajan, A.; Strachan, D. R.; Yi, G.-C.; Guiton, B. S. Direct Observation of Li Diffusion in Li-Doped ZnO Nanowires. *Mater. Res. Express* **2016**, *3*, 54001.
- (125) Tao, X.; Wang, K.; Wang, H.; Li, Q.; Xia, Y.; Huang, H.; Gan, Y.; Liang, C.; Zhang, W. Controllable Synthesis and *in Situ* TEM Study of Lithiation Mechanism of High Performance NaV3O8 Cathodes. *J. Mater. Chem. A* **2015**, *3*, 3044–3050.
- (126) Lu, X.; Adkins, E. R.; He, Y.; Zhong, L.; Luo, L.; Mao, S. X.; Wang, C.-M.; Korgel, B. A. Germanium as a Sodium Ion Battery Material: *In Situ* TEM Reveals Fast Sodiation Kinetics with High Capacity. *Chem. Mater.* **2016**, *28*, 1236–1242.
- (127) Knop-Gericke, A. X-Ray Photoelectron Spectroscopy. An Introduction to Principles and Practices. By Paul van Der Heide. *Angew. Chem. Int. Ed.* **2012**, *51*, 9218–9218.
- (128) Williams, D. B.; Carter, C. B. *Transmission Electron Microscopy: A Textbook for Materials Science*; 2nd ed.; Springer: New York, 2008.
- (129) Stroppa, D. G.; Zagonel, L. F.; Montoro, L. A.; Leite, E. R.; Ramirez, A. J. High-Resolution Scanning Transmission Electron Microscopy (HRSTEM) Techniques: High-Resolution Imaging and Spectroscopy Side by Side. *ChemPhysChem* **2012**, *13*, 437–443.
- (130) Pennycook, S. J. Z-Contrast Transmission Electron Microscopy: Direct Atomic Imaging of Materials. *Annu. Rev. Mater. Sci.* **1992**, *22*, 171–195.
- (131) Joy, D. C.; Maher, D. M. Electron Energy-Loss Spectroscopy. *J. Phys. [E]* **1980**, *13*, 260.
- (132) Hofer, F.; Schmidt, F. P.; Grogger, W.; Kothleitner, G. Fundamentals of Electron Energy-Loss Spectroscopy. *IOP Conf. Ser. Mater. Sci. Eng.* **2016**, *109*, 12007.
- (133) Walther, T.; Quandt, E.; Stegmann, H.; Thesen, A.; Benner, G. First Experimental Test of a New Monochromated and Aberration-Corrected 200kV Field-Emission Scanning Transmission Electron Microscope. *Ultramicroscopy* **2006**, *106*, 963–969.
- (134) Prabhudev, S.; Bugnet, M.; Zhu, G.-Z.; Bock, C.; Botton, G. A. Surface Segregation of Fe in Pt–Fe Alloy Nanoparticles: Its Precedence and Effect on the Ordered-Phase Evolution during Thermal Annealing. *ChemCatChem* **2015**, *7*, 3655–3664.
- (135) Garcia, D.; Leon, A.; Kumar, S. *In-Situ* Transmission Electron Microscope High Temperature Behavior in Nanocrystalline Platinum Thin Films. *JOM* **2015**, *68*, 109–115.
- (136) Liu, Z.; Che, R.; Elzatahry, A. A.; Zhao, D. Direct Imaging Au Nanoparticle Migration Inside Mesoporous Silica Channels. *ACS Nano* **2014**, *8*, 10455–10460.

- (137) Denny, N. R.; Li, F.; Norris, D. J.; Stein, A. *In Situ* High Temperature TEM Analysis of Sintering in Nanostructured Tungsten and Tungsten–molybdenum Alloy Photonic Crystals. *J. Mater. Chem.* **2010**, *20*, 1538–1545.
- (138) Zink, N.; Therese, H. A.; Pansiot, J.; Yella, A.; Banhart, F.; Tremel, W. *In Situ* Heating TEM Study of Onion-like WS₂ and MoS₂ Nanostructures Obtained via MOCVD. *Chem. Mater.* **2008**, *20*, 65–71.
- (139) Asthana, A.; Shokuhfar, T.; Gao, Q.; Heiden, P. A.; Friedrich, C.; Yassar, R. S. A Real Time Observation of Phase Transition of Anatase TiO₂ Nanotubes Into Rutile Nanoparticles by *In-Situ* Joule Heating Inside Transmission Electron Microscope. *Adv. Sci. Lett.* **2010**, *3*, 557–562.
- (140) Jin, H. W.; Park, C. G.; Kim, M. C. *In Situ* TEM Heating Studies on the Phase Transformation of Metastable Phases in Fe–Cr–B Alloy Spray Coatings. *Mater. Sci. Eng. A* **2001**, *304*, 321–326.
- (141) Barnard, A. S.; Young, N. P.; Kirkland, A. I.; van Huis, M. A.; Xu, H. Nanogold: A Quantitative Phase Map. *ACS Nano* **2009**, *3*, 1431–1436.
- (142) Kim, S. J.; Noh, S.-Y.; Kargar, A.; Wang, D.; Graham, G. W.; Pan, X. *In Situ* TEM Observation of the Structural Transformation of Rutile TiO₂ Nanowire during Electrochemical Lithiation. *Chem. Commun.* **2014**, *50*, 9932–9935.
- (143) Liu, S.; Xie, J.; Su, Q.; Du, G.; Zhang, S.; Cao, G.; Zhu, T.; Zhao, X. Understanding Li-Storage Mechanism and Performance of MnFe₂O₄ by *in Situ* TEM Observation on Its Electrochemical Process in Nano Lithium Battery. *Nano Energy* **2014**, *8*, 84–94.
- (144) Zeng, Z.; Liang, W.-I.; Chu, Y.-H.; Zheng, H. *In Situ* TEM Study of the Li–Au Reaction in an Electrochemical Liquid Cell. *Faraday Discuss.* **2015**, *176*, 95–107.
- (145) Asoro, M. A.; Kovar, D.; Ferreira, P. J. *In Situ* Transmission Electron Microscopy Observations of Sublimation in Silver Nanoparticles. *ACS Nano* **2013**, *7*, 7844–7852.
- (146) Hellebusch, D. J.; Manthiram, K.; Beberwyck, B. J.; Alivisatos, A. P. *In Situ* Transmission Electron Microscopy of Cadmium Selenide Nanorod Sublimation. *J. Phys. Chem. Lett.* **2015**, *6*, 605–611.
- (147) Allard, L. F.; Bigelow, W. C.; Jose-Yacamán, M.; Nackashi, D. P.; Damiano, J.; Mick, S. E. A New MEMS-Based System for Ultra-High-Resolution Imaging at Elevated Temperatures. *Microsc. Res. Tech.* **2009**, *72*, 208–215.
- (148) Poizot, P.; Laruelle, S.; Grugeon, S.; Dupont, L.; Tarascon, J.-M. Nano-Sized Transition-Metal Oxides as Negative-Electrode Materials for Lithium-Ion Batteries. *Nature* **2000**, *407*, 496–499.
- (149) Chen, Y. X.; He, L. H.; Shang, P. J.; Tang, Q. L.; Liu, Z. Q.; Liu, H. B.; Zhou, L. P. Micro-Sized and Nano-Sized Fe₃O₄ Particles as Anode Materials for Lithium-Ion Batteries. *J. Mater. Sci. Technol.* **2011**, *27*, 41–45.
- (150) Wang, H.; Cui, L.-F.; Yang, Y.; Sanchez Casalongue, H.; Robinson, J. T.; Liang, Y.; Cui, Y.; Dai, H. Mn₃O₄–Graphene Hybrid as a High-Capacity Anode Material for Lithium Ion Batteries. *J. Am. Chem. Soc.* **2010**, *132*, 13978–13980.
- (151) Huang, S.-Z.; Jin, J.; Cai, Y.; Li, Y.; Tan, H.-Y.; Wang, H.-E.; Tendeloo, G. V.; Su, B.-L. Engineering Single Crystalline Mn₃O₄ Nano-Octahedra with Exposed

- Highly Active {011} Facets for High Performance Lithium Ion Batteries. *Nanoscale* **2014**, *6*, 6819–6827.
- (152) Gummow, R. J.; de Kock, A.; Thackeray, M. M. Improved Capacity Retention in Rechargeable 4 V Lithium/Lithium-Manganese Oxide (Spinel) Cells. *Solid State Ion.* **1994**, *69*, 59–67.
- (153) Ammundsen, B.; Paulsen, J. Novel Lithium-Ion Cathode Materials Based on Layered Manganese Oxides. *Adv. Mater.* **2001**, *13*, 943–956.
- (154) Thackeray, M. M.; David, W. I. F.; Bruce, P. G.; Goodenough, J. B. Lithium Insertion into Manganese Spinels. *Mater. Res. Bull.* **1983**, *18*, 461–472.
- (155) Feltz, A.; Beck, F.-H.; Neidnicht, B. Redox Reactions in Condensed Oxide Systems XIII: Li Insertion Reaction of MgTiO_3 and the Spinels Mg_2TiO_4 , MgNiMnO_4 and MMn_2O_4 (M = Mn, Mg, Ni). *J. Alloys Compd.* **1991**, *176*, 347–355.
- (156) Allen, G. C.; Jutson, J. A. Carbon Deposition on Iron–manganese–chromium Spinels. *J. Mater. Chem.* **1991**, *1*, 73–78.
- (157) S. Kiiding, S. J. YSZ-Cells for Potentiometric Nitric Oxide Sensors. *Ionics* **2003**, *9*, 151–154.
- (158) Mehandjiev, D.; Zhecheva, E.; Ivanov, G.; Ioncheva, R. Preparation and Catalytic Activity of Nickel–manganese Oxide Catalysts with an Ilmenite-Type Structure in the Reactions of Complete Oxidation of Hydrocarbons. *Appl. Catal. Gen.* **1998**, *167*, 277–282.
- (159) Zhu, J.; Gao, Q. Mesoporous MCo_2O_4 (M = Cu, Mn and Ni) Spinels: Structural Replication, Characterization and Catalytic Application in CO Oxidation. *Microporous Mesoporous Mater.* **2009**, *124*, 144–152.
- (160) Tang, Z.-R.; Kondrat, S. A.; Dickinson, C.; Bartley, J. K.; Carley, A. F.; Taylor, S. H.; Davies, T. E.; Allix, M.; Rosseinsky, M. J.; Claridge, J. B.; *et al.* Synthesis of High Surface Area CuMn_2O_4 by Supercritical Anti-Solvent Precipitation for the Oxidation of CO at Ambient Temperature. *Catal. Sci. Technol.* **2011**, *1*, 740–746.
- (161) Papavasiliou, J.; Avgouropoulos, G.; Ioannides, T. Combined Steam Reforming of Methanol over Cu–Mn Spinel Oxide Catalysts. *J. Catal.* **2007**, *251*, 7–20.
- (162) Lodowicks, E.; Beck, F. Basic Characteristics of Spinel Type Manganese Mixed Oxide/Titanium Composite Anodes for Electroorganic Redox Catalysis. *Chem. Eng. Technol.* **1994**, *17*, 338–347.
- (163) Arrebola, J. C.; Caballero, A.; Hernán, L.; Morales, J. Improving the Performance of Lithium-Ion Batteries by Using Spinel Nanoparticles. *J. Nanomater.* **2008**, *2008*, e659397.
- (164) Gao, J.; Lowe, M. A.; Abruña, H. D. Spongelike Nanosized Mn_3O_4 as a High-Capacity Anode Material for Rechargeable Lithium Batteries. *Chem. Mater.* **2011**, *23*, 3223–3227.
- (165) Jian, G.; Xu, Y.; Lai, L.-C.; Wang, C.; Zachariah, M. R. Mn_3O_4 Hollow Spheres for Lithium-Ion Batteries with High Rate and Capacity. *J. Mater. Chem. A* **2014**, *2*, 4627–4632.
- (166) Cabana, J.; Valdés-Solís, T.; Palacín, M. R.; Oró-Solé, J.; Fuertes, A.; Marbán, G.; Fuertes, A. B. Enhanced High Rate Performance of LiMn_2O_4 Spinel Nanoparticles Synthesized by a Hard-Template Route. *J. Power Sources* **2007**, *166*, 492–498.

- (167) Shaju, K. M.; Bruce, P. G. A Stoichiometric Nano-LiMn₂O₄ Spinel Electrode Exhibiting High Power and Stable Cycling. *Chem. Mater.* **2008**, *20*, 5557–5562.
- (168) Lu, C.-Z.; Fey, G. T.-K. Nanocrystalline and Long Cycling LiMn₂O₄ Cathode Material Derived by a Solution Combustion Method for Lithium Ion Batteries. *J. Phys. Chem. Solids* **2006**, *67*, 756–761.
- (169) Wang, C.; Yin, L.; Xiang, D.; Qi, Y. Uniform Carbon Layer Coated Mn₃O₄ Nanorod Anodes with Improved Reversible Capacity and Cyclic Stability for Lithium Ion Batteries. *ACS Appl. Mater. Interfaces* **2012**, *4*, 1636–1642.
- (170) Hosono, E.; Kudo, T.; Honma, I.; Matsuda, H.; Zhou, H. Synthesis of Single Crystalline Spinel LiMn₂O₄ Nanowires for a Lithium Ion Battery with High Power Density. *Nano Lett.* **2009**, *9*, 1045–1051.
- (171) Song, Y. P.; Wang, P. W.; Xu, X. Y.; Wang, Z.; Li, G. H.; Yu, D. P. Magnetism and Photoluminescence in Manganese–gallium Oxide Nanowires with Monoclinic and Spinel Structures. *Phys. E Low-Dimens. Syst. Nanostructures* **2006**, *31*, 67–71.
- (172) Chen, Y.; Liu, Z.; Ringer, S. P.; Tong, Z.; Cui, X.; Chen, Y. Selective Oxidation Synthesis of MnCr₂O₄ Spinel Nanowires from Commercial Stainless Steel Foil. *Cryst. Growth Des.* **2007**, *7*, 2279–2281.
- (173) Na, C. W.; Han, D. S.; Park, J.; Jo, Y.; Jung, M.-H. Ferrimagnetic Mn₂SnO₄ Nanowires. *Chem. Commun.* **2006**, 2251.
- (174) Izawa, N.; Oi, T. Ion and Lithium Isotope Selectivities of Sorbents Prepared from Mg₂MnO₄. *J. Mater. Sci.* **1997**, *32*, 675–679.
- (175) de Kock, A.; Rossouw, M. H.; de Picciotto, L. A.; Thackeray, M. M.; David, W. I. F.; Ibberson, R. M. Defect Spinels in the System Li₂O•yMnO₂ (y>2.5): A Neutron-Diffraction Study and Electrochemical Characterization of Li₂Mn₄O₉. *Mater. Res. Bull.* **1990**, *25*, 657–664.
- (176) Garg, N.; Menaka; Ramanujachary, K. V.; Lofland, S. E.; Ganguli, A. K. Nanostructured Dimagnesium Manganese Oxide (Spinel): Control of Size, Shape and Their Magnetic and Electro Catalytic Properties. *J. Solid State Chem.* **2013**, *197*, 392–397.
- (177) Radhakrishnan, N. K.; Biswas, A. B. A Neutron Diffraction Study of the Spinel Oxide CuMn₂O₄. *Phys. Status Solidi A* **1977**, *44*, 45–49.
- (178) Miller, A. Determination of the Valence State of Copper in Cubic CuMn₂O₄ Spinel by X-Ray Absorption Edge Measurements. *J. Phys. Chem. Solids* **1968**, *29*, 633–639.
- (179) Gillot, B.; Buguet, S.; Kester, E. Oxidation Mechanism and Valence States of Copper and Manganese in Tetragonal CuMn₂O₄. *J. Mater. Chem.* **1997**, *7*, 2513–2517.
- (180) Waskowska, A.; Gerward, L.; Olsen, J. S.; Steenstrup, S.; Talik, E. CuMn₂O₄: Properties and the High-Pressure Induced Jahn-Teller Phase Transition. *J. Phys. Condens. Matter* **2001**, *13*, 2549.
- (181) Shoemaker, D. P.; Li, J.; Seshadri, R. Unraveling Atomic Positions in an Oxide Spinel with Two Jahn–Teller Ions: Local Structure Investigation of CuMn₂O₄. *J. Am. Chem. Soc.* **2009**, *131*, 11450–11457.

- (182) Xia, G. G.; Yin, Y. G.; Willis, W. S.; Wang, J. Y.; Suib, S. L. Efficient Stable Catalysts for Low Temperature Carbon Monoxide Oxidation. *J. Catal.* **1999**, *185*, 91–105.
- (183) Tanaka, Y.; Utaka, T.; Kikuchi, R.; Sasaki, K.; Eguchi, K. Water Gas Shift Reaction over Cu-Based Mixed Oxides for CO Removal from the Reformed Fuels. *Appl. Catal. Gen.* **2003**, *242*, 287–295.
- (184) Fang, D.; Xie, J.; Mei, D.; Zhang, Y.; He, F.; Liu, X.; Li, Y. Effect of CuMn_2O_4 Spinel in Cu–Mn Oxide Catalysts on Selective Catalytic Reduction of NO_x with NH_3 at Low Temperature. *RSC Adv.* **2014**, *4*, 25540–25551.
- (185) Lan, B.; Yu, L.; Lin, T.; Cheng, G.; Sun, M.; Ye, F.; Sun, Q.; He, J. Multifunctional Free-Standing Membrane from the Self-Assembly of Ultralong MnO_2 Nanowires. *ACS Appl. Mater. Interfaces* **2013**, *5*, 7458–7464.
- (186) Yang, Y.; Wang, P.; Zhang, Z.; Liu, H.; Zhang, J.; Zhuang, J.; Wang, X. Nanowire Membrane-Based Nanothermite: Towards Processable and Tunable Interfacial Diffusion for Solid State Reactions. *Sci. Rep.* **2013**, *3*, 1694.
- (187) Zhang, X.; Du, A. J.; Lee, P.; Sun, D. D.; Leckie, J. O. TiO_2 Nanowire Membrane for Concurrent Filtration and Photocatalytic Oxidation of Humic Acid in Water. *J. Membr. Sci.* **2008**, *313*, 44–51.
- (188) Liu, N.; Li, J.; Ma, W.; Liu, W.; Shi, Y.; Tao, J.; Zhang, X.; Su, J.; Li, L.; Gao, Y. Ultrathin and Lightweight 3D Free-Standing Ni@NiO Nanowire Membrane Electrode for a Supercapacitor with Excellent Capacitance Retention at High Rates. *ACS Appl. Mater. Interfaces* **2014**, *6*, 13627–13634.
- (189) Maiyalagan, T.; Chemelewski, K. R.; Manthiram, A. Role of the Morphology and Surface Planes on the Catalytic Activity of Spinel $\text{LiMn}_{1.5}\text{Ni}_{0.5}\text{O}_4$ for Oxygen Evolution Reaction. *ACS Catal.* **2014**, *4*, 421–425.
- (190) Xiao, X.; Wang, L.; Wang, D.; He, X.; Peng, Q.; Li, Y. Hydrothermal Synthesis of Orthorhombic LiMnO_2 Nano-Particles and LiMnO_2 Nanorods and Comparison of Their Electrochemical Performances. *Nano Res.* **2009**, *2*, 923–930.
- (191) Jia, Y.; Xu, J.; Zhou, L.; Liu, H.; Hu, Y. A Simple One Step Approach to Preparation of $\gamma\text{-MnOOH}$ Multipods and $\beta\text{-MnO}_2$ Nanorods. *Mater. Lett.* **2008**, *62*, 1336–1338.
- (192) Kester, E.; Gillot, B.; Perriat, P.; Dufour, P.; Villette, C.; Tailhades, P.; Rousset, A. Thermal Behavior and Cation Distribution of Submicron Copper Ferrite Spinels $\text{Cu}_x\text{Fe}_{3-x}\text{O}_4$ ($0 \leq x \leq 0.5$) Studied by DTG, FTIR, and XPS. *J. Solid State Chem.* **1996**, *126*, 7–14.
- (193) Gillot, B.; Buguet, S.; Kester, E. Oxidation Mechanism and Valence States of Copper and Manganese in Tetragonal CuMn_2O_4 . *J. Mater. Chem.* **1997**, *7*, 2513–2517.
- (194) Lenglet, M.; D’Huysser, A.; Kasperek, J.; Bonnelle, J. P.; Dürr, J. Characterisation Des Etats D’oxydation Du Cuiver et Du Manganese Dans Quelques Manganites Par Analyse Des Spectres XPS, D’émission X et Des Seuils D’absorption X. *Mater. Res. Bull.* **1985**, *20*, 745–757.
- (195) Töpfer, J.; Feltz, A.; Gräf, D.; Hackl, B.; Raupach, L.; Weissbrodt, P. Cation Valencies and Distribution in the Spinels NiMn_2O_4 and $\text{MzNiMn}_{2-z}\text{O}_4$ (M = Li, Cu) Studied by XPS. *Phys. Status Solidi A* **1992**, *134*, 405–415.

- (196) Suntivich, J.; May, K. J.; Gasteiger, H. A.; Goodenough, J. B.; Shao-Horn, Y. A. Perovskite Oxide Optimized for Oxygen Evolution Catalysis from Molecular Orbital Principles. *Science* **2011**, *334*, 1383–1385.
- (197) Jin, C.; Cao, X.; Zhang, L.; Zhang, C.; Yang, R. Preparation and Electrochemical Properties of Urchin-like $\text{La}_{0.8}\text{Sr}_{0.2}\text{MnO}_3$ Perovskite Oxide as a Bifunctional Catalyst for Oxygen Reduction and Oxygen Evolution Reaction. *J. Power Sources* **2013**, *241*, 225–230.
- (198) Cheng, F.; Shen, J.; Peng, B.; Pan, Y.; Tao, Z.; Chen, J. Rapid Room-Temperature Synthesis of Nanocrystalline Spinels as Oxygen Reduction and Evolution Electrocatalysts. *Nat. Chem.* **2011**, *3*, 79–84.
- (199) Kempa, T. J.; Kim, S.-K.; Day, R. W.; Park, H.-G.; Nocera, D. G.; Lieber, C. M. Facet-Selective Growth on Nanowires Yields Multi-Component Nanostructures and Photonic Devices. *J. Am. Chem. Soc.* **2013**, *135*, 18354–18357.
- (200) Cho, B.; Park, K. S.; Baek, J.; Oh, H. S.; Koo Lee, Y.-E.; Sung, M. M. Single-Crystal Poly(3,4-Ethylenedioxythiophene) Nanowires with Ultrahigh Conductivity. *Nano Lett.* **2014**, *14*, 3321–3327.
- (201) Wallentin, J.; Anttu, N.; Asoli, D.; Huffman, M.; Åberg, I.; Magnusson, M. H.; Siefert, G.; Fuss-Kailuweit, P.; Dimroth, F.; Witzigmann, B.; *et al.* InP Nanowire Array Solar Cells Achieving 13.8% Efficiency by Exceeding the Ray Optics Limit. *Science* **2013**, *339*, 1057–1060.
- (202) Qiu, J.; Qiu, Y.; Yan, K.; Zhong, M.; Mu, C.; Yan, H.; Yang, S. All-Solid-State Hybrid Solar Cells Based on a New Organometal Halide Perovskite Sensitizer and One-Dimensional TiO_2 Nanowire Arrays. *Nanoscale* **2013**, *5*, 3245–3248.
- (203) Xia, X.; Tu, J.; Zhang, Y.; Mai, Y.; Wang, X.; Gu, C.; Zhao, X. Freestanding Co_3O_4 Nanowire Array for High Performance Supercapacitors. *RSC Adv.* **2012**, *2*, 1835–1841.
- (204) Kumar, N.; Srivastava, A. K.; Nath, R.; Gupta, B. K.; Varma, G. D. Probing the Highly Efficient Room Temperature Ammonia Gas Sensing Properties of a Luminescent ZnO Nanowire Array Prepared via an AAO-Assisted Template Route. *Dalton Trans.* **2014**, *43*, 5713–5720.
- (205) Bograchev, D. A.; Volgin, V. M.; Davydov, A. D. Simple Model of Mass Transfer in Template Synthesis of Metal Ordered Nanowire Arrays. *Electrochim Acta* **2013**, *96*, 1–7.
- (206) Yao, Z.; Wang, C.; Li, Y.; Kim, N.-Y. AAO-Assisted Synthesis of Highly Ordered, Large-Scale TiO_2 Nanowire Arrays via Sputtering and Atomic Layer Deposition. *Nanoscale Res. Lett.* **2015**, *10*.
- (207) Grote, F.; Kühnel, R.-S.; Balducci, A.; Lei, Y. Template Assisted Fabrication of Free-Standing MnO_2 Nanotube and Nanowire Arrays and Their Application in Supercapacitors. *Appl. Phys. Lett.* **2014**, *104*, 53904.
- (208) Jafari Jam, R.; Heurlin, M.; Jain, V.; Kvennefors, A.; Graczyk, M.; Maximov, I.; Borgström, M. T.; Pettersson, H.; Samuelson, L. III–V Nanowire Synthesis by Use of Electrodeposited Gold Particles. *Nano Lett.* **2015**, *15*, 134–138.
- (209) Jensen, L. E.; Björk, M. T.; Jeppesen, S.; Persson, A. I.; Ohlsson, B. J.; Samuelson, L. Role of Surface Diffusion in Chemical Beam Epitaxy of InAs Nanowires. *Nano Lett.* **2004**, *4*, 1961–1964.

- (210) Geng, C.; Jiang, Y.; Yao, Y.; Meng, X.; Zapien, J. A.; Lee, C. S.; Lifshitz, Y.; Lee, S. T. Well-Aligned ZnO Nanowire Arrays Fabricated on Silicon Substrates. *Adv. Funct. Mater.* **2004**, *14*, 589–594.
- (211) Kuykendall, T.; Pauzauskie, P. J.; Zhang, Y.; Goldberger, J.; Sirbuly, D.; Denlinger, J.; Yang, P. Crystallographic Alignment of High-Density Gallium Nitride Nanowire Arrays. *Nat. Mater.* **2004**, *3*, 524–528.
- (212) Wan, Q.; Wei, M.; Zhi, D.; MacManus-Driscoll, J. L.; Blamire, M. G. Epitaxial Growth of Vertically Aligned and Branched Single-Crystalline Tin-Doped Indium Oxide Nanowire Arrays. *Adv. Mater.* **2006**, *18*, 234–238.
- (213) Schmitt, S. W.; Schechtel, F.; Amkreutz, D.; Bashouti, M.; Srivastava, S. K.; Hoffmann, B.; Dieker, C.; Spiecker, E.; Rech, B.; Christiansen, S. H. Nanowire Arrays in Multicrystalline Silicon Thin Films on Glass: A Promising Material for Research and Applications in Nanotechnology. *Nano Lett.* **2012**, *12*, 4050–4054.
- (214) Choi, D.-G.; Yu, H. K.; Jang, S. G.; Yang, S.-M. Colloidal Lithographic Nanopatterning via Reactive Ion Etching. *J. Am. Chem. Soc.* **2004**, *126*, 7019–7025.
- (215) Whitney, A. V.; Myers, B. D.; Van Duyne, R. P. Sub-100 Nm Triangular Nanopores Fabricated with the Reactive Ion Etching Variant of Nanosphere Lithography and Angle-Resolved Nanosphere Lithography. *Nano Lett.* **2004**, *4*, 1507–1511.
- (216) Tan, B. J. Y.; Sow, C. H.; Koh, T. S.; Chin, K. C.; Wee, A. T. S.; Ong, C. K. Fabrication of Size-Tunable Gold Nanoparticles Array with Nanosphere Lithography, Reactive Ion Etching, and Thermal Annealing. *J. Phys. Chem. B* **2005**, *109*, 11100–11109.
- (217) Brodoceanu, D.; Alhmod, H. Z.; Elnathan, R.; Delalat, B.; Voelcker, N. H.; Kraus, T. Fabrication of Silicon Nanowire Arrays by near-Field Laser Ablation and Metal-Assisted Chemical Etching. *Nanotechnology* **2016**, *27*, 75301.
- (218) Li, Y.; Duan, C. Bubble-Regulated Silicon Nanowire Synthesis on Micro-Structured Surfaces by Metal-Assisted Chemical Etching. *Langmuir* **2015**, *31*, 12291–12299.
- (219) Liu, Y.; Sun, W.; Jiang, Y.; Zhao, X.-Z. Fabrication of Bifacial Wafer-Scale Silicon Nanowire Arrays with Ultra-High Aspect Ratio through Controllable Metal-Assisted Chemical Etching. *Mater. Lett.* **2015**, *139*, 437–442.
- (220) Um, H.-D.; Kim, N.; Lee, K.; Hwang, I.; Hoon Seo, J.; Yu, Y. J.; Duane, P.; Wober, M.; Seo, K. Versatile Control of Metal-Assisted Chemical Etching for Vertical Silicon Microwire Arrays and Their Photovoltaic Applications. *Sci. Rep.* **2015**, *5*, 11277.
- (221) Yeom, J.; Ratchford, D.; Field, C. R.; Brintlinger, T. H.; Pehrsson, P. E. Decoupling Diameter and Pitch in Silicon Nanowire Arrays Made by Metal-Assisted Chemical Etching. *Adv. Funct. Mater.* **2014**, *24*, 106–116.
- (222) Li, L.; Liu, Y.; Zhao, X.; Lin, Z.; Wong, C.-P. Uniform Vertical Trench Etching on Silicon with High Aspect Ratio by Metal-Assisted Chemical Etching Using Nanoporous Catalysts. *ACS Appl. Mater. Interfaces* **2014**, *6*, 575–584.
- (223) McSweeney, W.; Geaney, H.; O'Dwyer, C. Metal-Assisted Chemical Etching of Silicon and the Behavior of Nanoscale Silicon Materials as Li-Ion Battery Anodes. *Nano Res.* **2015**, *8*, 1395–1442.

- (224) Asoh, H.; Suzuki, Y.; Ono, S. Metal-Assisted Chemical Etching of GaAs Using Au Catalyst Deposited on the Backside of a Substrate. *Electrochim Acta* **2015**, *183*, 8–14.
- (225) Wagner, R. S. A Solid-Liquid-Vapor Etching Process. *J. Cryst. Growth* **1968**, *3–4*, 159–161.
- (226) Givargizov, E. I.; Babasian, P. A. Negative Whiskers Formed by Solid-Liquid-Vapor Mechanism during Vaporization of ZnS. *J. Cryst. Growth* **1977**, *37*, 140–146.
- (227) Babasian, R. A.; Givargizov, E. I. Vaporization of CdS Single Crystals and Formation of Negative Whiskers. *J. Mater. Sci.* **1980**, *15*, 1619–1624.
- (228) Givargizov, E. I.; Babasian, R. A. Mechanisms and Kinetics of Vapor-Phase Etching of GaAs and GaP. *J. Electron. Mater.* **1980**, *9*, 883–904.
- (229) Borgström, M. T.; Wallentin, J.; Kawaguchi, K.; Samuelson, L.; Deppert, K. Dynamics of Extremely Anisotropic Etching of InP Nanowires by HCl. *Chem. Phys. Lett.* **2011**, *502*, 222–224.
- (230) Hui, H. Y.; Filler, M. A. Solid–Liquid–Vapor Etching of Semiconductor Nanowires. *Nano Lett.* **2015**, *15*, 6939–6945.
- (231) Nikoobakht, B.; Herzing, A.; Muramoto, S.; Tersoff, J. Vapor–Liquid–Solid Etch of Semiconductor Surface Channels by Running Gold Nanodroplets. *Nano Lett.* **2015**, *15*, 8360–8364.
- (232) Huang, Z.; Geyer, N.; Werner, P.; de Boor, J.; Gösele, U. Metal-Assisted Chemical Etching of Silicon: A Review: In Memory of Prof. Ulrich Gösele. *Adv. Mater.* **2011**, *23*, 285–308.
- (233) Geyer, N.; Fuhrmann, B.; Huang, Z.; de Boor, J.; Leipner, H. S.; Werner, P. Model for the Mass Transport during Metal-Assisted Chemical Etching with Contiguous Metal Films As Catalysts. *J. Phys. Chem. C* **2012**, *116*, 13446–13451.
- (234) Kim, B.-J.; Stach, E. A. Desorption Induced Formation of Negative Nanowires in GaN. *J. Cryst. Growth* **2011**, *324*, 119–123.
- (235) Hudak, B. M.; Chang, Y.-J.; Yu, L.; Li, G.; Edwards, D. N.; Guiton, B. S. Real-Time Observation of the Solid–Liquid–Vapor Dissolution of Individual Tin(IV) Oxide Nanowires. *ACS Nano* **2014**, *8*, 5441–5448.
- (236) Tien, L. C.; Norton, D. P.; Budai, J. D. Epitaxial Growth of Transparent Tin Oxide Films on (0001) Sapphire by Pulsed Laser Deposition. *Mater. Res. Bull.* **2009**, *44*, 6–10.
- (237) Dasgupta, N. P.; Sun, J.; Liu, C.; Britzman, S.; Andrews, S. C.; Lim, J.; Gao, H.; Yan, R.; Yang, P. 25th Anniversary Article: Semiconductor Nanowires – Synthesis, Characterization, and Applications. *Adv. Mater.* **2014**, *26*, 2137–2184.
- (238) Gudixsen, M. S.; Wang, J.; Lieber, C. M. Synthetic Control of the Diameter and Length of Single Crystal Semiconductor Nanowires. *J. Phys. Chem. B* **2001**, *105*, 4062–4064.
- (239) Kim, B. J.; García, R. E.; Stach, E. A. Kinetics of Congruent Vaporization of ZnO Islands. *Phys. Rev. Lett.* **2011**, *107*, 146101.
- (240) Corr, S. A.; Shoemaker, D. P.; Toberer, E. S.; Seshadri, R. Spontaneously Formed Porous and Composite Materials. *J. Mater. Chem.* **2010**, *20*, 1413–1422.

- (241) Zacharatos, F.; Gianneta, V.; Nassiopoulou, A. G. Highly Ordered Hexagonally Arranged Nanostructures on Silicon through a Self-Assembled Silicon-Integrated Porous Anodic Alumina Masking Layer. *Nanotechnology* **2008**, *19*, 495306.
- (242) Qiao, Y.; Wang, D.; Buriak, J. M. Block Copolymer Templated Etching on Silicon. *Nano Lett.* **2007**, *7*, 464–469.
- (243) Wang, C. G.; Wu, X. Z.; Di, D.; Dong, P. T.; Xiao, R.; Wang, S. Q. Orientation-Dependent Nanostructure Arrays Based on Anisotropic Silicon Wet-Etching for Repeatable Surface-Enhanced Raman Scattering. *Nanoscale* **2016**, *8*, 4672–4680.
- (244) Ellingham, H. Transactions and Communications. *J. Soc. Chem. Ind.* **1944**, *63*, 125–160.
- (245) Wu, J.; Gross, A.; Yang, H., Shape and Composition-Controlled Platinum Alloy Nanocrystals Using Carbon Monoxide as Reducing Agent. *Nano Letters* **2011**, *11*(2), 798-802.
- (246) Goodman, J. F.; Gregg, S. J. 237. The Production of Active Solids by Thermal Decomposition. Part XI. The Heat Treatment of Precipitated Stannic Oxide. *J. Chem. Soc.* **1960**, 1162–1167.
- (247) Lamoreaux, R. H.; Hildenbrand, D. L.; Brewer, L. High-Temperature Vaporization Behavior of Oxides II. Oxides of Be, Mg, Ca, Sr, Ba, B, Al, Ga, In, Tl, Si, Ge, Sn, Pb, Zn, Cd, and Hg. *J. Phys. Chem. Ref. Data* **1987**, *16*, 419–443.
- (248) Yang, C. C.; Li, J. C.; Jiang, Q. Effect of Pressure on Melting Temperature of Silicon Determined by Clapeyron Equation. *Chem. Phys. Lett.* **2003**, *372*, 156–159.
- (249) Prieto, G.; Tüysüz, H.; Duyckaerts, N.; Knossalla, J.; Wang, G.-H.; Schüth, F. Hollow Nano- and Microstructures as Catalysts. *Chem. Rev.* **2016**, *116*, 14056–14119.
- (250) Jiang, Z.; Zhu, J.; Liu, D.; Wei, W.; Xie, J.; Chen, M. *In Situ* Synthesis of Bimetallic Ag/Pt Loaded Single-Crystalline Anatase TiO₂ Hollow Nano-Hemispheres and Their Improved Photocatalytic Properties. *CrystEngComm* **2014**, *16*, 2384–2394.
- (251) Jiao, W.; Wang, L.; Liu, G.; Lu, G. Q. (Max); Cheng, H.-M. Hollow Anatase TiO₂ Single Crystals and Mesocrystals with Dominant {101} Facets for Improved Photocatalysis Activity and Tuned Reaction Preference. *ACS Catal.* **2012**, *2*, 1854–1859.
- (252) Wang, Z.; Zhou, L.; (David) Lou, X. W. Metal Oxide Hollow Nanostructures for Lithium-Ion Batteries. *Adv. Mater.* **2012**, *24*, 1903–1911.
- (253) Zhou, L.; Zhuang, Z.; Zhao, H.; Lin, M.; Zhao, D.; Mai, L. Intricate Hollow Structures: Controlled Synthesis and Applications in Energy Storage and Conversion. *Adv. Mater.* **2017**.
- (254) Yu, X.-Y.; Yu, L.; Lou, X. W. (David). Metal Sulfide Hollow Nanostructures for Electrochemical Energy Storage. *Adv. Energy Mater.* **2016**, *6*.
- (255) Cao, S.-W.; Zhu, Y.-J.; Ma, M.-Y.; Li, L.; Zhang, L. Hierarchically Nanostructured Magnetic Hollow Spheres of Fe₃O₄ and γ -Fe₂O₃: Preparation and Potential Application in Drug Delivery. *J. Phys. Chem. C* **2008**, *112*, 1851–1856.
- (256) Cabana, J.; Monconduit, L.; Larcher, D.; Palacín, M. R. Beyond Intercalation-Based Li-Ion Batteries: The State of the Art and Challenges of Electrode

- Materials Reacting Through Conversion Reactions. *Adv. Mater.* **2010**, *22*, E170–E192.
- (257) Chen, J.; Xu, L.; Li, W.; Gou, X. α -Fe₂O₃ Nanotubes in Gas Sensor and Lithium-Ion Battery Applications. *Adv. Mater.* **2005**, *17*, 582–586.
- (258) Wang, Z.; Luan, D.; Madhavi, S.; Li, C. M.; Lou, X. W. (David). α -Fe₂O₃ Nanotubes with Superior Lithium Storage Capability. *Chem. Commun.* **2011**, *47*, 8061–8063.
- (259) Yang, P.; Ding, Y.; Lin, Z.; Chen, Z.; Li, Y.; Qiang, P.; Ebrahimi, M.; Mai, W.; Wong, C. P.; Wang, Z. L. Low-Cost High-Performance Solid-State Asymmetric Supercapacitors Based on MnO₂ Nanowires and Fe₂O₃ Nanotubes. *Nano Lett.* **2014**, *14*, 731–736.
- (260) Ma, L.; Ma, H.; Gao, N.; Wang, J.; Zhang, X. Controllable Synthesis of α -Fe₂O₃ Nanotubes with High Surface Area: Preparation, Growth Mechanism, and Its Catalytic Performance for the Selective Catalytic Reduction of NO with NH₃. *J. Mater. Sci.* **2015**, *51*, 1959–1965.
- (261) Qu, X.; Kobayashi, N.; Komatsu, T. Solid Nanotubes Comprising α -Fe₂O₃ Nanoparticles Prepared from Ferritin Protein. *ACS Nano* **2010**, *4*, 1732–1738.
- (262) Lian, J.; Duan, X.; Ma, J.; Peng, P.; Kim, T.; Zheng, W. Hematite (α -Fe₂O₃) with Various Morphologies: Ionic Liquid-Assisted Synthesis, Formation Mechanism, and Properties. *ACS Nano* **2009**, *3*, 3749–3761.
- (263) Paterson, E.; Swaffield, R.; Clark, D. R. Thermal Decomposition of Synthetic Akaganeite (β -FeOOH). *Thermochim. Acta* **1982**, *54*, 201–211.
- (264) Meroño, M. D.; Morales, J.; Tirado, J. L. Thermal Behaviour of Synthetic Akaganeite under Different Experimental Conditions. *Thermochim. Acta* **1985**, *92*, 525–528.
- (265) Chen, M.; Jiang, J.; Zhou, X.; Diao, G. Preparation of Akaganeite Nanorods and Their Transformation to Sphere Shape Hematite. *J. Nanosci. Nanotechnol.* **2008**, *8*, 3942–3948.
- (266) Bernal, J. D.; Dasgupta, D. R.; Mackay, A. L. The Oxides and Hydroxides of Iron and Their Structural Inter-Relationships. *Clay Miner.* **1959**, *4*, 15–30.
- (267) Gonzalez-Calbet, J. M.; Franco, M. A. A. A Thermogravimetric and Electron Microscopy Study of the Decomposition of Akaganeite. *Thermochim. Acta* **1982**, *58*, 45–51.
- (268) Galbraith, S. T.; Baird, T.; Fryer, J. R. Structural Changes in β -FeOOH Caused by Radiation Damage. *Acta Crystallogr. A* **1979**, *35*, 197–200.
- (269) González-Calbet, J. M.; Alario-Franco, M. A.; Gayoso-Andrade, M. The Porous Structure of Synthetic Akaganeite. *J. Inorg. Nucl. Chem.* **1981**, *43*, 257–264.
- (270) Jin, Z.; Wang, F.; Wang, F.; Wang, J.; Yu, J. C.; Wang, J. Metal Nanocrystal-Embedded Hollow Mesoporous TiO₂ and ZrO₂ Microspheres Prepared with Polystyrene Nanospheres as Carriers and Templates. *Adv. Funct. Mater.* **2013**, *23*, 2137–2144.
- (271) Arnal, P. M.; Weidenthaler, C.; Schüth, F. Highly Monodisperse Zirconia-Coated Silica Spheres and Zirconia/Silica Hollow Spheres with Remarkable Textural Properties. *Chem. Mater.* **2006**, *18*, 2733–2739.
- (272) Li, W.-C.; Lu, A.-H.; Weidenthaler, C.; Schüth, F. Hard-Templating Pathway To Create Mesoporous Magnesium Oxide. *Chem. Mater.* **2004**, *16*, 5676–5681.

- (273) Mijangos, C.; Hernández, R.; Martín, J. A Review on the Progress of Polymer Nanostructures with Modulated Morphologies and Properties, Using Nanoporous AAO Templates. *Prog. Polym. Sci.* **2016**, *54–55*, 148–182.
- (274) Wan, J.; Stone, H. A. Coated Gas Bubbles for the Continuous Synthesis of Hollow Inorganic Particles. *Langmuir* **2012**, *28*, 37–41.
- (275) He, Ge; Liu; Wang; Zhang. Synthesis of Cagelike Polymer Microspheres with Hollow Core/Porous Shell Structures by Self-Assembly of Latex Particles at the Emulsion Droplet Interface. *Chem. Mater.* **2005**, *17*, 5891–5892.
- (276) Yang, M.; Ma, J.; Zhang, C.; Yang, Z.; Lu, Y. General Synthetic Route toward Functional Hollow Spheres with Double-Shelled Structures. *Angew. Chem. Int. Ed.* **2005**, *44*, 6727–6730.
- (277) Wang, Y.; Zhu, Q.; Zhang, H. Fabrication of β -Ni(OH)₂ and NiO Hollow Spheres by a Facile Template-Free Process. *Chem. Commun.* **2005**, 5231–5233.
- (278) Xiong, Y.; Wiley, B.; Chen, J.; Li, Z.-Y.; Yin, Y.; Xia, Y. Corrosion-Based Synthesis of Single-Crystal Pd Nanoboxes and Nanocages and Their Surface Plasmon Properties. *Angew. Chem. Int. Ed.* **2005**, *44*, 7913–7917.
- (279) Yin, Y.; Rioux, R. M.; Erdonmez, C. K.; Hughes, S.; Somorjai, G. A.; Alivisatos, A. P. Formation of Hollow Nanocrystals Through the Nanoscale Kirkendall Effect. *Science* **2004**, *304*, 711–714.
- (280) Fan, H. J.; Knez, M.; Scholz, R.; Hesse, D.; Nielsch, K.; Zacharias, M.; Gösele, U. Influence of Surface Diffusion on the Formation of Hollow Nanostructures Induced by the Kirkendall Effect: The Basic Concept. *Nano Lett.* **2007**, *7*, 993–997.
- (281) Lou, X. W.; Wang, Y.; Yuan, C.; Lee, J. Y.; Archer, L. A. Template-Free Synthesis of SnO₂ Hollow Nanostructures with High Lithium Storage Capacity. *Adv. Mater.* **2006**, *18*, 2325–2329.
- (282) Herman, D. A. J.; Cheong, S.; Banholzer, M. J.; Tilley, R. D. How Hollow Structures Form from Crystalline Iron–iron Oxide Core–shell Nanoparticles in the Electron Beam. *Chem. Commun.* **2013**, *49*, 6203–6205.
- (283) Niu, K.-Y.; Park, J.; Zheng, H.; Alivisatos, A. P. Revealing Bismuth Oxide Hollow Nanoparticle Formation by the Kirkendall Effect. *Nano Lett.* **2013**, *13*, 5715–5719.
- (284) Yu, L.; Yan, Z.; Cai, Z.; Zhang, D.; Han, P.; Cheng, X.; Sun, Y. Quantitatively *in Situ* Imaging Silver Nanowire Hollowing Kinetics. *Nano Lett.* **2016**, *16*, 6555–6559.
- (285) Zboril, R.; Mashlan, M.; Krausova, D.; Pikal, P. Cubic β -Fe₂O₃ as the Product of the Thermal Decomposition of Fe₂(SO₄)₃. *Hyperfine Interact.* **1999**, *120–121*, 497–501.
- (286) Sakurai, S.; Namai, A.; Hashimoto, K.; Ohkoshi, S. First Observation of Phase Transformation of All Four Fe₂O₃ Phases ($\gamma \rightarrow \varepsilon \rightarrow \beta \rightarrow \alpha$ -Phase). *J. Am. Chem. Soc.* **2009**, *131*, 18299–18303.
- (287) Zboril, R.; Mashlan, M.; Machala, L.; Bezdicka, P. Iron(III) Oxides Formed During Thermal Conversion of Rhombohedral Iron(III) Sulfate. *Material Research in Atomic Scale by Mössbauer Spectroscopy* **2003**, *94*, pp. 21–30.
- (288) Ben-Dor, L.; Fischbein, E.; Kalman, Z. Concerning the β Phase of iron(III) Oxide. *Acta Crystallogr. B* **1976**, *32*, 667–667.

- (289) González-Carreño, T.; Morales, M. P.; Serna, C. J. Fine β -Fe₂O₃ Particles with Cubic Structure Obtained by Spray Pyrolysis. *J. Mater. Sci. Lett.* **1994**, *13*, 381–382.
- (290) Lee, C.-W.; Jung, S.-S.; Lee, J.-S. Phase Transformation of β -Fe₂O₃ Hollow Nanoparticles. *Mater. Lett.* **2008**, *62*, 561–563.
- (291) Inouye, K.; Shibata, K.; Ozeki, S.; Kaneko, K. Ferromagnetic Iron Oxides from Synthetic β -FeOOH by Vacuum Thermal Decomposition. *J. Electrochem. Soc.* **1984**, *131*, 2435–2438.
- (292) Tan, H.; Verbeeck, J.; Abakumov, A.; Van Tendeloo, G. Oxidation State and Chemical Shift Investigation in Transition Metal Oxides by EELS. *Ultramicroscopy* **2012**, *116*, 24–33.
- (293) Guo, W.; Zhou, Y.; Sang, X.; Leonard, D. N.; Qu, J.; Poplawsky, J. D. Atom Probe Tomography Unveils Formation Mechanisms of Wear-Protective Tribofilms by ZDDP, Ionic Liquid, and Their Combination. *ACS Appl. Mater. Interfaces* **2017**.
- (294) Bischoff, J.; Motta, A. T. EFTEM and EELS Analysis of the Oxide Layer Formed on HCM12A Exposed to SCW. *J. Nucl. Mater.* **2012**, *430*, 171–180.
- (295) Kim, H. S.; Piao, Y.; Kang, S. H.; Hyeon, T.; Sung, Y.-E. Uniform Hematite Nanocapsules Based on an Anode Material for Lithium Ion Batteries. *Electrochem. Commun.* **2010**, *12*, 382–385.
- (296) Chaudhari, N. K.; Yu, J.-S. Size Control Synthesis of Uniform β -FeOOH to High Coercive Field Porous Magnetic α -Fe₂O₃ Nanorods. *J. Phys. Chem. C* **2008**, *112*, 19957–19962.
- (297) Wang, Z.; Luan, D.; Madhavi, S.; Hu, Y.; Lou, X. W. (David). Assembling Carbon-Coated α -Fe₂O₃ Hollow Nanohorns on the CNT Backbone for Superior Lithium Storage Capability. *Energy Environ. Sci.* **2012**, *5*, 5252–5256.
- (298) Braun, H.; Gallagher, K. J. β -Fe₂O₃, a New Structural Form of Iron (III) Oxide. *Nature* **1972**, *240*, 13–14.
- (299) Navrotsky, A.; Ma, C.; Lilova, K.; Birkner, N. Nanophase Transition Metal Oxides Show Large Thermodynamically Driven Shifts in Oxidation-Reduction Equilibria. *Science* **2010**, *330*, 199–201.
- (300) Li, D.; Duan, X.; Qin, Q.; Fan, H.; Zheng, W. Ionic Liquid-Assisted Synthesis of Mesoporous α -Ga₂O₃ Hierarchical Structures with Enhanced Photocatalytic Activity. *J. Mater. Chem. A* **2013**, *1*, 12417–12421.
- (301) Li, Y.; Tan, B.; Wu, Y. Freestanding Mesoporous Quasi-Single-Crystalline Co₃O₄ Nanowire Arrays. *J. Am. Chem. Soc.* **2006**, *128*, 14258–14259.

VITA

Lei Yu

Education

- B.S. in Chemistry, Beijing Institute of Technology, China June 2012

Professional Experience

Oak Ridge National laboratory, Research Assistant July 2016-July 2017
Supervisor: **Dr. Karren L. More**

University of Kentucky, Research Assistant Fall 2012- July 2017
Supervisor: **Prof. Beth Guiton**

University of Kentucky, Teaching Assistant Fall 2012-Spring 2014

- General Chemistry

Publications and Presentations

Patent

- B. S. Guiton, **L. Yu**, “Design and Synthesis of Metal Oxide Surfaces and Interfaces with Crystallographic Control Using Solid-Liquid-Vapor Etching and Vapor-Liquid-Solid Growth” US Patent, 2016, pending

Pear-reviewed Journal Papers (Total, 6)

- J. Liu, D. Olds, R. Peng, **L. Yu**, G. Foo, S. Qian, J. Keum, B. S. Guiton, Z. Wu, K. Page, Quantitative Analysis of the Morphology of {101} and {001} Faceted Anatase TiO₂ Nanocrystals and Its Application on Photocatalytic Activity, *Chemistry of Materials*, 2017, *ASAP*
- **L. Yu**, A. J. Riddle, S. Wang, A. Sundararajan, J. Thompson, Y. -J. Chang, M. E. Park, S. A. Seo, B. S. Guiton, Solid-Liquid-Vapor Synthesis of Negative Metal Oxide Nanowire Arrays, *Chemistry of Materials*, 2016, 28, pp 8924-8929
- **L. Yu**, Y. Zhang, B. M. Hudak, D. K. Wallace, D. Y. Kim, B. S. Guiton, Simple Synthetic Route to Manganese-Containing Nanowires with the Spinel Crystal Structure, *Journal of Solid State Chemistry*, 2016, 240, pp 23-29
- G. Li, **L. Yu**, B. M. Hudak, Y.-J. Chang, H. Baek, A. Sundararajan, D. Strachan, G. Yi, B. S. Guiton, Direct Observation of Li Diffusion in Li-doped ZnO Nanowires, *Material Research Express*, 2016, 3, 054001
- B. M. Hudak, Y.-J. Chang, **L. Yu**, G. Li, D. N. Edwards, M. E. Park, and B. S. Guiton, Understanding nanomaterial synthesis with *in situ* transmission electron microscopy, *Microscopy and Microanalysis*, *Microscopy and Microanalysis*, 2015, 21, pp 1507-1508

- B. M. Hudak, Y.-J. Chang, **L. Yu**, G. Li, D. N. Edwards, and B. S. Guiton, Real-time Observation of the Solid--Liquid--Vapor Dissolution of Individual Tin(IV) Oxide Nanowires, *ACS Nano*, 2014, 8, pp 5441–5448

Conference Presentations (Total, 9)

- **L. Yu et al.**, “Understanding Hollow Metal Oxide Nanomaterial Formation with *in situ* Transmission Electron Microscopy”, 2017 M&M, St. Louis, Mo, Aug 2017, Poster presenter
- **L. Yu et al.**, “Exploring metal oxide nanostructure synthesis mechanisms using *in situ* TEM”, 2017 MRS Spring, Phoenix, AZ, Apr 2017, Oral presenter
- **L. Yu et al.**, “Exploring metal oxide nanostructure synthesis mechanisms using *in situ* TEM”, 253rd ACS National Meeting, San Francisco, CA, Apr 2017, Oral presenter
- **L. Yu et al.**, “Direct observation of manganese-containing nanowire formation with spinel crystal structure in *in situ* TEM”, 2016 ACS Southeast Regional Meeting (SERMACS), Columbia, SC, Oct 2016, Oral presenter
- **L. Yu et al.**, “Exploring simple synthetic mechanism to form manganese-containing nanowires with the Spinel crystal structure”, 2016 KY NSF EPSCoR Supper Collider, Lexington, KY, Feb. 2016, Poster presenter
- **L. Yu et al.**, “Development and direct observation of a simple synthetic mechanism to form manganese-containing nanowires with the Spinel crystal structure”, 2015 MRS Fall Meeting & Exhibit, Boston, MA, Dec 2015, Poster presenter
- **L. Yu et al.**, “Exploring synthetic route to metal oxide nanowires with the Spinel crystal structure”, 2015 CNMS User Meeting, Oak Ridge National Laboratory, TN, Sep 2015, Oral & Poster presenter
- **L. Yu et al.**, “Synthesis and characterization of manganese-containing nanowires with the Spinel crystal structure”, 2015 KY EPSCoR Annual Conference-Promoting Industry and Academic Research Collaborations, Lexington, KY, May 2015, Poster presenter